A polarized p+p and p+A program for the next years

The STAR Collaboration

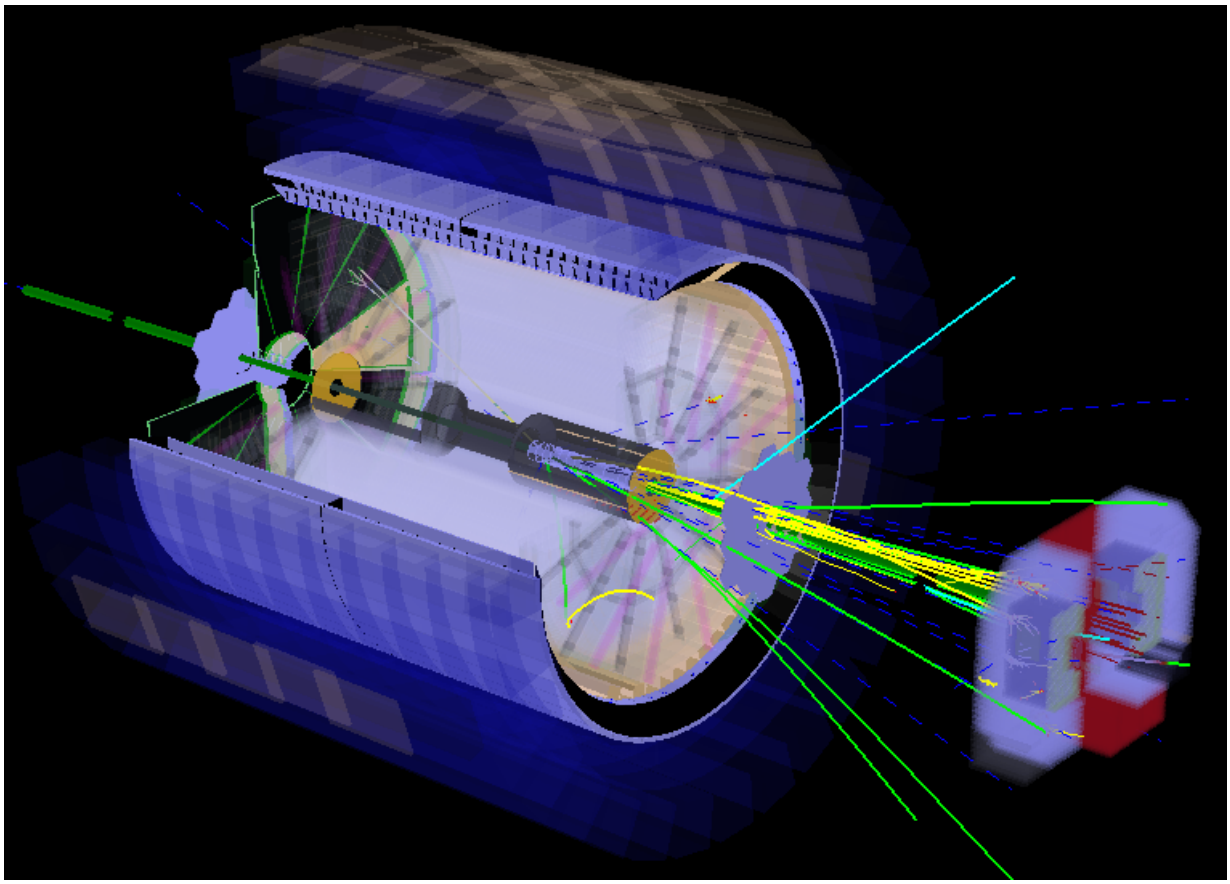

May 2014

1 Executive Summary

In this document, the STAR collaboration presents a science driven program for future polarized p+p and p+A beam operations at RHIC in the time period after Beam Energy Scan phase II and prior to the transition to eRHIC. This document is in response to an October 2013 charge from the BNL Associate Laboratory Director Berndt Mueller, which is reproduced in the Appendix. STAR has previously submitted a white paper and a Letter of Intent describing its plans for Beam Energy Scan phase II [1] and eRHIC [2], respectively.

The major scientific goal of the polarized p+p and p+A program is to explore Quantum Chromo Dynamics (QCD) in the high and low Bjorken *x* domain, driven by four overarching questions,

- *What is the nature of the spin of the proton?*
- *How do quarks and gluons hadronize into final-state particles?*
- *How can we describe the multidimensional landscape of nucleons and nuclei?*
- *What is the nature of the initial state in nuclear collisions?*

It is centered around the unique capabilities afforded with the existing STAR detector, complemented with detector upgrades including the forward calorimetric system (FCS) and forward tracking system (FCS), which are required to carry out the proposed physics program at forward rapidities. The proposed FCS and FTS upgrades were first envisioned in the STAR Decadal Plan [3] and represent a natural evolution of the growth for STAR scientific program. These upgrades will also be in an integral part of the eSTAR configuration at eRHIC area as outlined in our eSTAR LOI.

The envisioned beam operation periods and primary science objectives are:

Species	$\sqrt{s}$	$L_{\text{delivered}}$	Goal
Longitudinally polarized p+p	500 GeV	1 fb^{-1}	Low *x* Gluon helicity
Transversely polarized p+p	500 GeV	1 fb^{-1}	Transverse Momentum Dependent proton spin structure
transversely polarized p+A with 3 nuclei: C, Cu, Au	200 GeV	2.5 pb^{-1}	Saturation and nuclear parton distributions

We propose measurements with forward photon, J/ψ, Drell-Yan, inclusive and di-jet, and hadron/jet correlation probes at both energies, as well as W and Z probes at top energy, and demonstrate measurement capability and sensitivity through detailed simulations. It will be shown that these probes allow addressing fundamental aspects of the nucleon partonic structure, which are still rather poorly determined by experiment. One is the nature of the nucleon spin; the other is go beyond our current simple one-dimensional picture of nucleons by correlating the information on the individual parton contribution to the spin of the nucleon with its transverse momentum and spatial distribution inside the nucleon.

Measuring these probes in p+A collisions give the unique opportunity to progress our quest to understand QCD processes in Cold Nuclear Matter (CNM) by studying the dynamics of partons at very small and very large momentum fractions *x* in nuclei, and at high gluon-density to investigate the existence of nonlinear evolution effects.

In the remainder of this document, we motivate polarized p+p and p+A science and outline the world-wide context. We also discuss the potential for discovery in the search of exotics, i.e. glueballs by combining STAR's large detector acceptance with its small angle tagging capabilities. Section 2 contains our proposed measurements and section 3 outlines the necessary instrument upgrades, their cost and an envisioned construction schedule.

2 The science of polarized p+p and p+A

Quantum Chromodynamics (QCD), the theory of strong interactions, is a cornerstone of the Standard Model of modern physics. It explains all strongly interacting matter in terms of point-like quarks interacting by the exchange of gauge bosons, known as gluons. This strongly interacting matter is responsible for 99% of the visible mass in the universe. Over the past several decades, a rich picture has come to light, with several overarching questions remaining that have been and continue to be addressed by the RHIC p+p and p+A program:

- *What is the nature of the spin of the proton?*
- *How do quarks and gluons hadronize into final-state particles?*
- *How can we describe the multidimensional landscape of nucleons and nuclei?*
- *What is the nature of the initial state in nuclear collisions?*

Much of our present knowledge of nucleon structure comes from deep-inelastic lepton-nucleon scattering (DIS) experiments, with a great wealth of data on the unpolarized structure of the proton available from HERA [4]. From HERA we have learned that quarks carry 50% of the momentum of the proton, with the other half carried by gluons, which dominate for x <0.1.

Despite all that has been learned through DIS measurements, studying nucleon structure in a wide variety of reactions is essential in order to piece together a complete picture. Hadron-hadron interactions offer several advantages. Direct access to gluons is possible through parton-parton scattering, making measurement of the spin contribution of the gluon to the spin of the proton a key component of the RHIC program. W-Boson production and the Drell-Yan process are both golden probes to cleanly access antiquark distributions in hadron-hadron collisions. Drell-Yan will become an increasingly important part of the future RHIC p+p and p+A program. Comparing observations from DIS and hadronic interactions also allows us to test the assumptions of universality across processes in describing hadron structure and hadronization within the framework of perturbative QCD (pQCD). In the high-energy limit of pQCD, calculations in which the quarks and gluons are treated as nearly free particles moving collinearly with their parent hadron, and in which hadronic interactions are assumed to factorize into a) parton distribution functions (PDFs) within the initial-state hadron, b) partonic hard-scattering cross sections, and c) fragmentation functions (FFs) describing the hadronization of the scattered parton, have had tremendous success in describing hadronic cross sections at high energies over the past several decades. The collider energies available at RHIC, put high-p_T reactions comfortably within a regime described by factorized pQCD. It is worth noting that the relevant perturbative scale in DIS is Q^2, while in hadron-hadron interactions it is the square of the transverse momentum (p_T^2) of the produced jet or particle, and while both Q^2 and x are known in DIS, in hadron-hadron measurements the p_T of the produced particle is correlated with x, but a given p_T bin typically samples from a range of x values. At high energy, there remain two fundamental aspects of the nucleon partonic structure, which are rather poorly determined by experiment. One is the nature of the nucleon spin; the other is go beyond our current simple one-dimensional picture of nucleons by correlating the information on the individual parton contribution to the spin of the nucleon with its transverse momentum and spatial distribution inside the nucleon.

These questions have also manifested themselves in the nuclear physics performance milestones from DOE.

Table 2-1 list the current nuclear physics performance milestones related to the RHIC p+p and p+A physics program. There is currently only one NP performance milestone related to the RHIC p+A program (DM8, 2012). In the following sections we will describe how STAR is planning to address these questions in the next years.

Year	#	Milestone
2013	HP8	Measure flavor-identified q and $\bar{q}$ contributions to the spin of the proton via the longitudinal-spin asymmetries of W production
2013	HP12 (update of HP1 met in 2008)	Utilize polarized proton collisions at center of mass energies of 200 and 500 GeV, in combination with global QCD analyses, to determine if gluons have appreciable polarization over any range of momentum fraction between 1 and 30% of the momentum of a polarized proton.
2015	HP13 (new)	Test unique QCD predictions for relations between single-transverse spin phenomena in p-p scattering and those observed in deep –inelastic lepton scattering
2012	DM8	Determine the gluon densities at low x in cold nuclei via p+Au or d+Au collisions

Table 2-1: Current nuclear physics performance milestones related to the RHIC p+p physics program.

2.1 Kinematics of inclusive forward jets in p+p with the proposed forward upgrade

Both the measurement of the helicity structure and the transverse spin structure of the nucleon use reconstructed jets and di-jets to narrow the phase space of partonic kinematics. Since jets serve as proxies for the scattered partons, reconstructed jets allow the selection of events with a specific weighting of the fractional momenta of the parent protons carried by the scattering partons, assuming a 2-to-2 process. Here we call the fractional momentum carried by the parton coming from the beam along the z-axis (towards the proposed forward upgrade instrumentation) x_1, and the fractional momentum carried by the other parton x_2.

For measurements of A_{LL} it is important to select events where one x is determined with good accuracy within the kinematic region in which one wants to measure $\Delta g(x)$ and the other x is in a region where the helicity distribution is well known, i.e. in the region of medium to high values *of* x. The transverse spin structure of the nucleon on the other hand is usually accessed using transverse single spin asymmetries and semi-inclusive measurements. This means one measures azimuthal asymmetries of the final state, where the distribution function of interest couples to a spin dependent fragmentation function that serves as a polarimeter. Consequently we studied how in single- and di-jet events, the jet pseudorapidity η and p_T are related to the underlying partonic variables x_1 and x_2. We also studied the matching between reconstructed jets and scattered partons and the resolutions with which the parton axis can be reconstructed from the reconstructed detector jets. The latter is important to evaluate how well azimuthal asymmetries around the outgoing parton axis will be reconstructed by looking at asymmetries of reconstructed particles around the reconstructed jet axis.

For this study we used 500k events simulated with Pythia Tune A at $\sqrt{s}$=500 GeV and a minimum partonic p_T (CKIN3) of 3 GeV. We then used a fast simulation of the detector resolutions of the STAR barrel and the forward upgrade. For the purpose of this study we assumed a tracking detector with three planes at distances from the interaction point of 70 cm, 105 cm and 140 cm. Each plane is comprised of 1.2% radiation lengths of material with resolutions in the azimuthal direction between 0.11 and 0.85 mm/$\sqrt{12}$. Furthermore, we simulated a detector subsystem combining hadronic and electromagnetic calorimeters (FCS) with $0.58/\sqrt{E}$ hadronic resolution and an electromagnetic resolution of $0.11/\sqrt{E}$. In this setup, except for those tracks with very low energy, the track momentum is reconstructed in the FCS and the tracking is used mainly for charge discrimination. Jets were reconstructed with an anti-k_T algorithm with a radius of 0.7. An association between reconstructed jets and scattered partons is defined to be a distance in η-ϕ space of less than 0.5.

In the following, we refer to reconstructed jets as "detector jets" and jets found using stable, final state particles "particle jets." The outgoing partons in the event are determined by using the corresponding entries in the Pythia record, so there is no partonic jet finding.

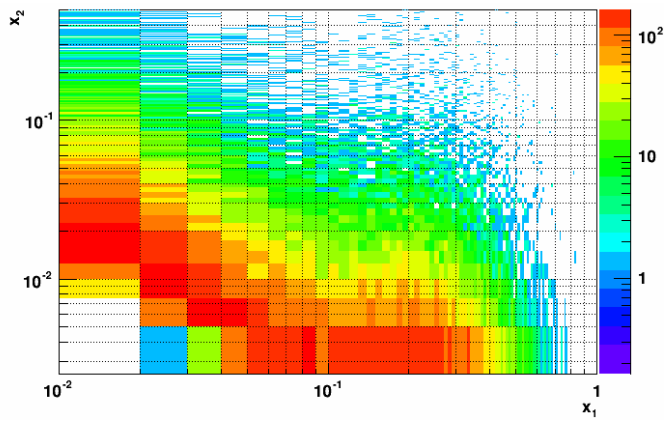

Figure 2-1: Distribution of the partonic variables x_1 and x_2 for events with a jet with $p_T > 3$ GeV/c and $2.8 < \eta < 3.5$. x_1 values of around 0.6 can be reached whereas x_2 goes as low as 7×10^{-3}.

Figure 2-1 shows the regions of x that can be accessed by jets in the forward region. A minimum jet p_T of 3 GeV/c was chosen to ensure that the momentum transfer is sufficiently high for pQCD calculations to be valid. At high x, values of x~0.6 should be reachable. This compares well with the current limit of SIDIS measurements, *x~0.3*, and encompasses the region in x that dominates the tensor charge. To investigate the possibility of selecting specific x regions, in particular high x, the dependence of x on the jet p_T and pseudorapidity was studied.

Figure 2-2 shows x_1 as a function of jet p_T and Figure 2-3 and Figure 2-4 show the η dependence for two p_T bins. For both the η and p_T dependences one can observe two bands: One that exhibits an η or p_T dependence and one that remains at low x. Based on the profile plots in Figure 2-3 and Figure 2-4, high x can be reached with small dilution for high η and p_T.

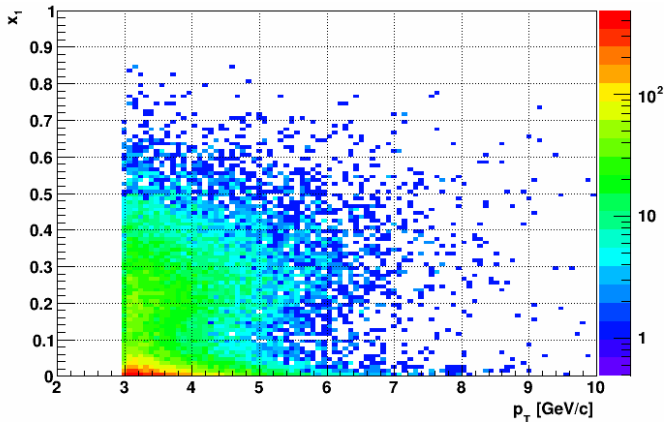

Figure 2-2: x_1 versus jet p_T. As expected, there is a correlation between the x accessed and the p_T of the jet. However, there is an underlying band of low x_1 values. This can be improved by further restricting the η range of the jet. Here $2.8 < \eta < 3.8$.

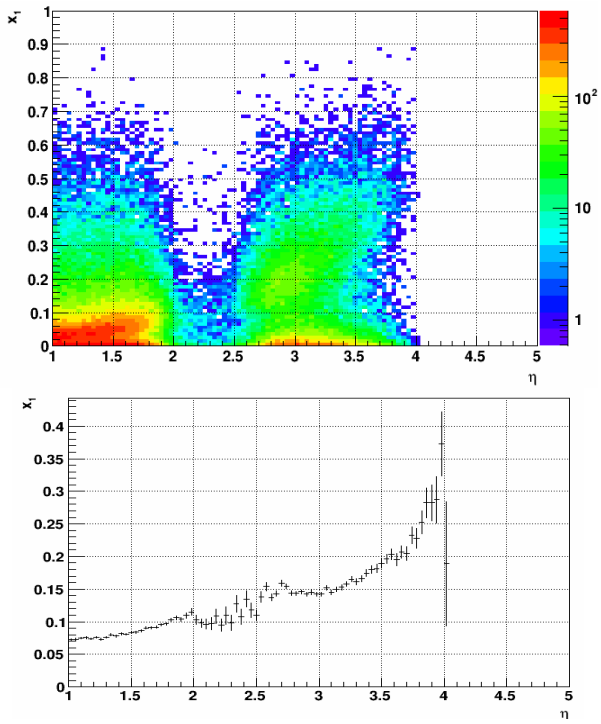

Figure 2-3: x_1 vs jet η. The upper figure shows a 2D histogram and the lower figure the profile plot. Here a minimum jet p_T of 3 GeV/c was required. One can see that the events are split into two bands. One exhibits a strong correlation with η, whereas the other is flat at low x_1. In the region of the forward upgrade x_1 values between 0.15 and 0.3 are accessible.

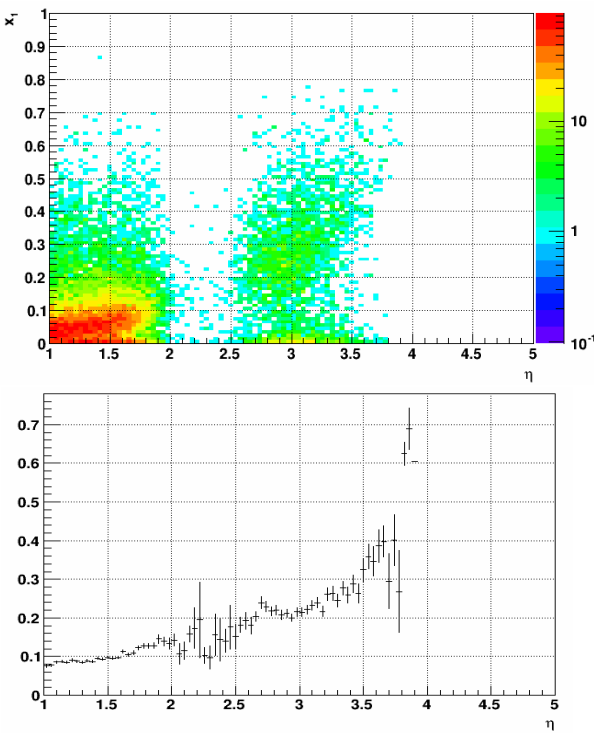

Figure 2-4: Same as in Figure 2-3 but with a minimum jet p_T of 5 GeV/c. This shows that additional p_T cuts allow one to push the accessible mean x to higher values. In this case, x_1 values between 0.2 and 0.4 are achievable.

For measurements of azimuthal asymmetries of jets or hadrons within a jet to probe the transverse spin structure of the nucleon it is important to reconstruct reliably the outgoing parton direction. Therefore, the matching of reconstructed jets to scattered partons was studied (Figure 2-5). Figure 2-6 and Figure 2-7 show the mean distance of partons to associated detector jets and detector jets to associated particle jets. In general, matching and parton axis smearing improves with p_T, which may be connected to the jet multiplicity that rises with transverse momentum. Figure 2-8 and Figure 2-9 give the p_T and resulting z smearing for the reconstructed jets. Here, z is defined as the fractional energy carried by the fragmenting hadron. The reconstruction of the transverse momentum is poor, but z exhibits a more favorable correlation. Possible explanations are compensation between jet and hadron momentum smearing and the domination of the z correlation by high multiplicity jets where the jet p_T reconstruction is more reliable.

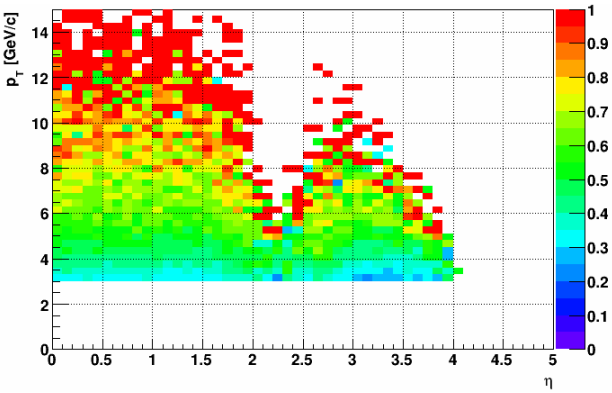

Figure 2-5: Matching Fraction between detector jets and partons. The matching fraction at low p_T is only around 50%, but grows to over 90% for high p_T. Unfortunately, the statistics at high p_T in the forward region is small.

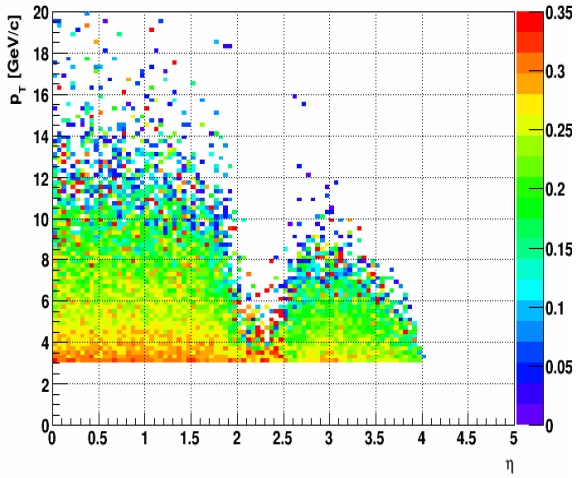

Figure 2-6: Mean distance between matching parton and detector jets. For most jets the mean distance in η–ϕ space is around 0.2, but depends strongly on the jet p_T.

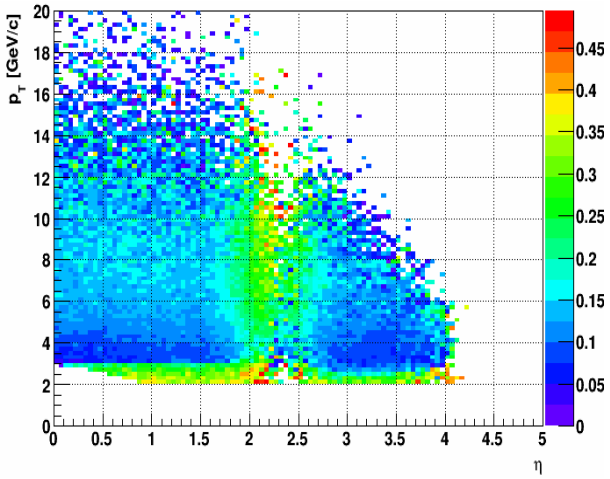

Figure 2-7: Mean distance between detector and particle jets. Detector and particle jets are closer to each other than the detector jets to the parton. The regions of large distance are caused by the lack of coverage between barrel and forward instrumentation and the lower minimum p_T cut for the particle jets.

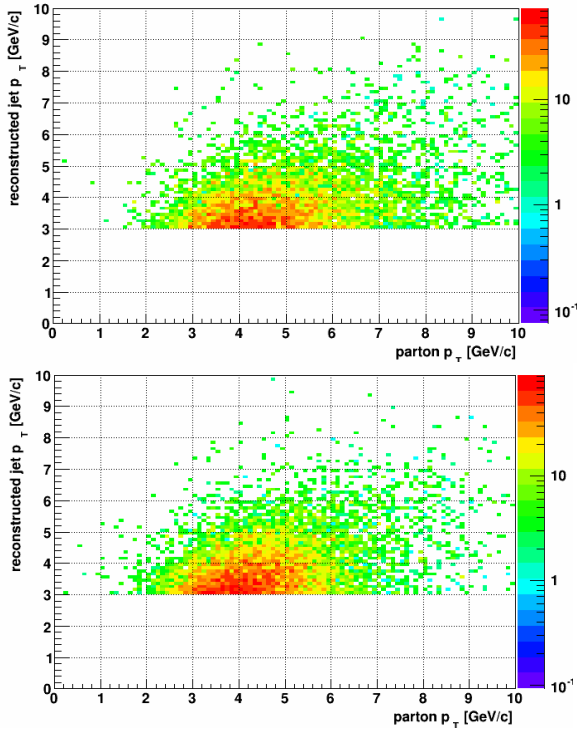

Figure 2-8: Transverse momentum smearing for reconstructed jets compared to that of the associated parton. The upper figure shows the smearing for jets with $2 < \eta < 3$ and the lower figure for those with $3 < \eta < 4$.

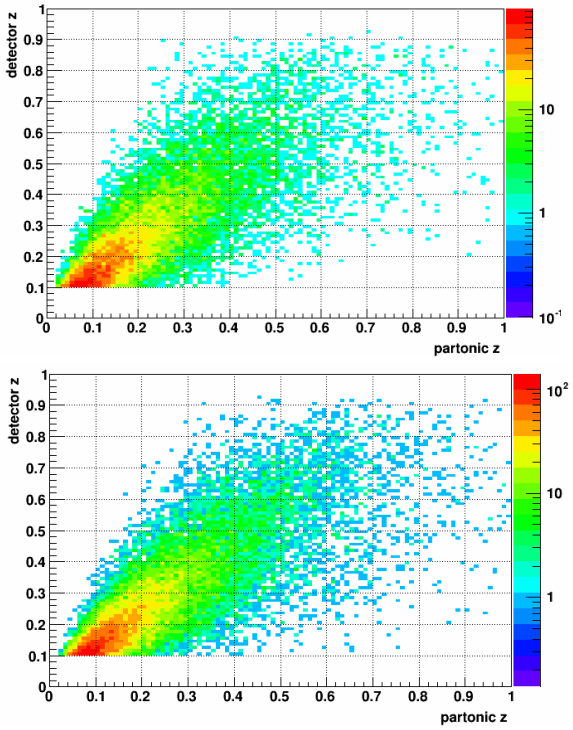

Figure 2-9: Smearing of z, the fractional momentum of the outgoing parton/jet carried by the outgoing hadron. The upper figure shows the smearing for jets with $2 < \eta < 3$ and the lower figure for jets with $3 < \eta < 4$.

2.2 Confined Motion of Partons in Nucleons

A natural next step in the investigation of nucleon structure is an expansion of our current picture of the nucleon by imaging the proton in both momentum and impact parameter space. At the

same time we need to further our understanding of color interactions and how they manifest themselves in different processes. In the new theoretical framework of transverse momentum dependent (TMD) parton distributions we can obtain an image in transverse as well as in longitudinal momentum space (2+1 dimensions). This has attracted renewed interest, both experimentally and theoretically, in transverse single spin asymmetries (SSA) in hadronic processes at high energies, which have a more than 30 year history. Measurements at RHIC have extended the observations from the fixed-target energy range to the collider regime, up to and including the highest center-of-mass energies to date in polarized p+p collisions. Figure 2-10 summarizes the measured asymmetries from different experiments as functions of Feynman-x ($x_F \sim x_1$-x_2).

The surprisingly large asymmetries seen are nearly independent of $\sqrt{s}$ over a very wide range. To understand the observed SSAs one has to go beyond the conventional collinear parton picture in the hard processes. Two theoretical formalisms have been proposed to generate sizable SSAs in the QCD framework: transverse momentum dependent parton distributions and fragmentation functions, which provide the full transverse momentum information, and the collinear quark-gluon-quark correlations, which provide information about the average transverse momentum. At RHIC the p_T-scale is sufficiently large to make the collinear quark-gluon-quark correlation formalism the appropriate approach to calculate the spin asymmetries. Here, various underlying mechanisms can contribute and need to be disentangled to understand the experimental observations in detail, in particular the p_T-dependence. These mechanisms are associated with the spin of the initial state nucleon (Sivers/Qiu-Sterman effects) and outgoing hadrons (Collins effects).

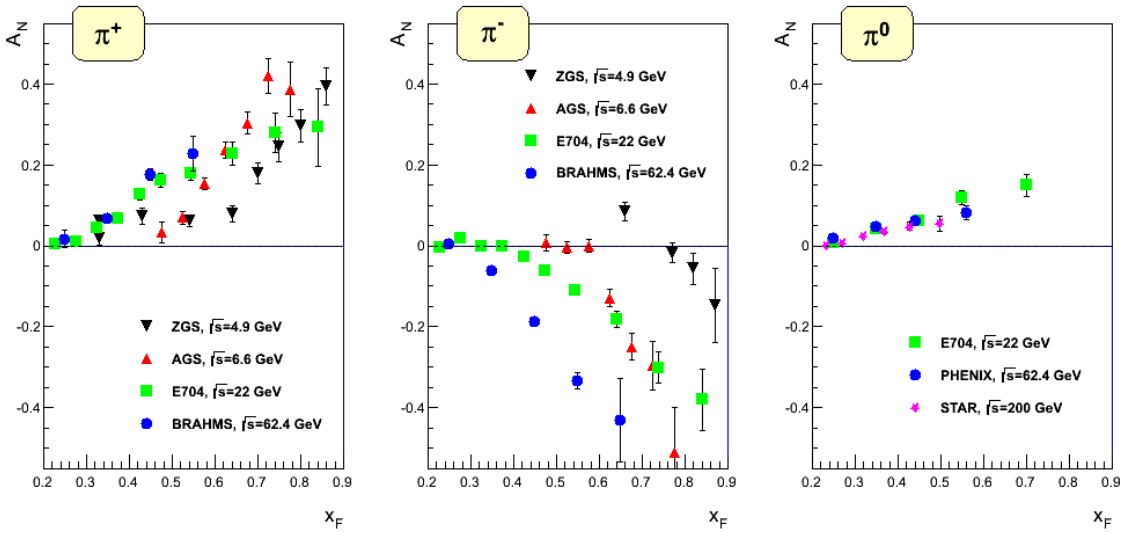

Figure 2-10: Transverse single spin asymmetry measurements for charged and neutral pions at different center-of-mass energies as function of Feynman-x.

The Sivers function, $f_{1T}^{\perp}$, describes the correlation of the parton transverse momentum with the transverse spin of the nucleon. A non-vanishing $f_{1T}^{\perp}$ means that the parton distribution will be azimuthally asymmetric in the **transverse momentum space** relative to the nucleon spin direction. The Collins function, $H_1^{\perp}$, describes a correlation of the transverse spin of a scattered quark and the transverse momenta of the fragmentation products and as such can lead to an asymmetry of the distribution of hadrons in jets. Contrary to the Sivers effect, the Collins fragmentation function is universal among different processes: SIDIS, e^+e^- annihilation, and p+p collisions. This is of special importance to the p+p case where it is always coupled to the chirally odd quark transversity distribution, which describes the transverse spin preference of quarks in a transversely polarized proton.

STAR pioneered in the last years the research in p+p collisions to identify observables that will help to separate the contributions from initial and final states, and will give insight to the transverse spin structure of hadrons. In the following it will be discussed how the current and future STAR data will help to answer the following burning questions:

- *Do the large transverse single spin asymmetries survive at high center-of-mass energies?*
- *Can the subprocess responsible for A_N be uniquely identified?*
- *Is the observed p_T-dependence of A_N consistent with theory expectations in pQCD*
- *Can the TMD evolution, which is different from the well-known DGLAP evolution, be seen in the RHIC data?*

Our current understanding is based on the already taken or soon to be taken data sets listed in Table 2-2.

Year	√s (GeV)	Recorded Luminosity for transversely polarized p+p	<P>
2006	200	8.5 pb^{-1}	57
2008	200	7.8 pb^{-1}	45
2011	500	25 pb^{-1}	53/54
2012	200	22 pb^{-1}	61/58
2015	200	50 pb^{-1}	60
2016	500	400 pb^{-1} (7w) / 900 pb^{-1} (14w)	50

Table 2-2: Luminosity recorded by STAR in the past transverse polarized p+p runs from 2006 onward. The luminosities listed for 2015 and 2016 are projected.

STAR primary contributions to the transverse spin physics have been through the study of forward neutral pion production in p+p collisions (see, for example, ref. [5,6]). This effort has been extended to include the first measurements at $\sqrt{s}$ = 200 GeV of the transverse spin asymmetry A_N for the η meson [7]. The Run-11 data taken with transverse polarization at $\sqrt{s}$ = 500 GeV have revealed several surprising results. Figure 2-11 shows the transverse single spin asymmetry A_N for electromagnetic jets detected in the forward meson spectrometer (FMS) at $2.5 < \eta < 4.0$ as a function of the jet p_T for different photon multiplicities and jet energy ranges. It can be clearly seen that with increasing number of photons in the electromagnetic jet (increasing "jettiness" of the event) the asymmetry becomes smaller. Jets with an isolated π^0 have the largest asymmetry consistent with the asymmetry in inclusive π^0 events, as seen from the right-most panel in Figure 2-10. For all jet energies and photon multiplicities in the jet, the asymmetries are basically flat as a function of jet p_T, a feature also already seen for inclusive π^0 asymmetries. Recently, it has been proposed that in the collinear, twist-3 factorization approach a significant portion of the sizable inclusive pion asymmetries seen at forward pseudorapidity is due to twist-3 fragmentation functions coupled to transversity [8]. This calculation is the first one which showed, similar to the experiment [9], a flat p_T dependence for A_N. The ability for this approach to describe adequately the effects seen at SIDIS and at RHIC is a potentially significant breakthrough in the longstanding mystery surrounding the nonzero inclusive asymmetries at forward pseudorapidity (e.g. Ref. [10]). For these reasons, the most desirable kinematic region for future study at RHIC is in the region of $\eta > 2$.

To further study these effects the transverse single spin asymmetry A_N of these electromagnetic jets was also measured requiring that, in addition, a correlated away side jet in the rapidity range $-1 < \eta < 2$ was present. Figure 2-12 shows clearly that for requiring an additional

correlated away-side jet the asymmetry for isolated forward π^0 mesons becomes smaller. For further details see reference [11]. Both these observations raise serious questions regarding how much of the large forward π^0 asymmetries are caused by 2→2 parton scattering processes.

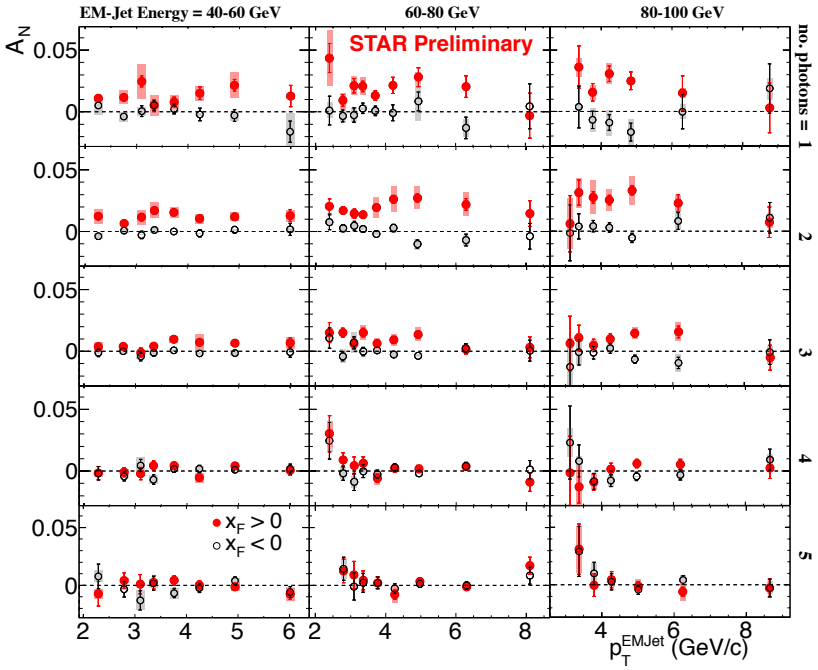

Figure 2-11: The transverse single spin asymmetry A_N for electromagnetic jets detected in the forward meson spectrometer ($2.5 < \eta < 4.0$) as function of the jet p_T and the photon multiplicity in the jet in bins of the jet energy.

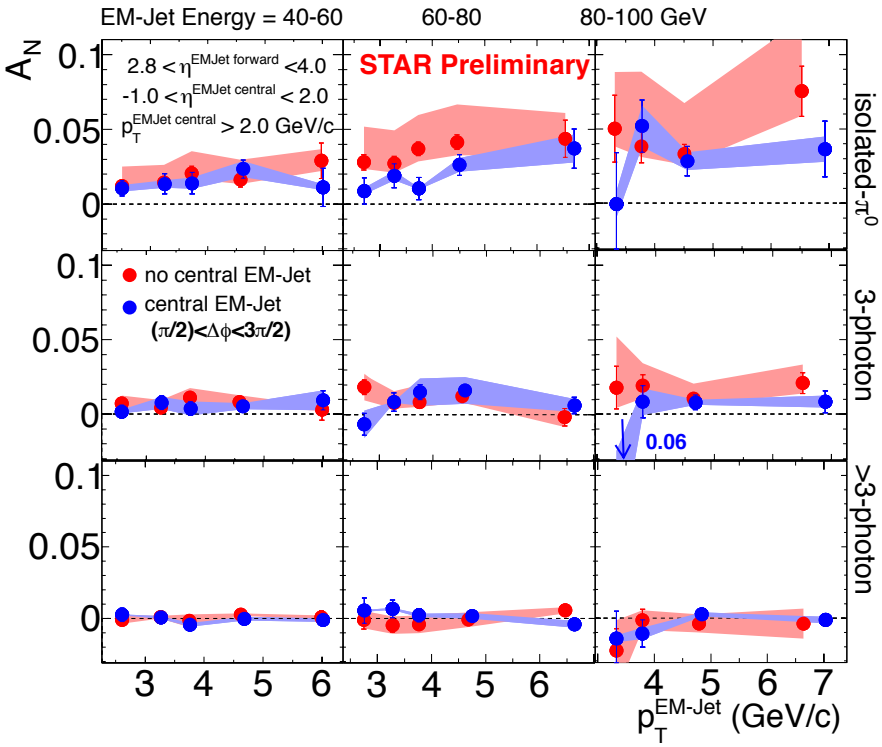

Figure 2-12: The transverse single spin asymmetry A_N for electromagnetic jets detected in the forward meson spectrometer ($2.5 < \eta < 4.0$) as a function of the jet p_T and the photon multiplicity in the jet, in bins of the jet energy (red points). The blue points represent the transverse single spin asymmetry A_N if further a correlated

away side jet in the rapidity range -1 < η < 2 was required. The blue and red bands represent the systematic uncertainties.

To disentangle the different subprocesses even further it is important to identify more exclusive measurements (which are particularly sensitive to certain processes). Table 2-3 identifies observables which will help to separate the contributions from initial and final states, and will give insight to the transverse spin structure of hadrons. Most observables in p+p collisions can only be related to the transverse spin structure of hadrons through the twist-3 formalism, where only one hard scale is required. For the TMD framework, a second scale is required, as can be provided in di-jets, W, Z, or Drell-Yan production.

Sivers	**Transversity *h(x)* × Collins FF**
A_N as a function of rapidity, E_T, p_T and x_F for inclusive jets, direct photons and charmed mesons	A_N as a function p_T and the invariant mass of the hadron pair (IFF) $A_{UT}^{\sin\Phi} = A_{UT}\sin(\Phi_R - \Phi_S) = \frac{\sigma^{\uparrow} - \sigma^{\downarrow}}{\sigma^{\uparrow} + \sigma^{\downarrow}}\sin(\Phi_R - \Phi_S).$
A_N as a function of rapidity, p_T for $W^{\pm}$, Z^0 and DY	Hadron correlations within a jet
	A_{UT} as a function of the azimuthal dependence of the correlated hadron pair on the spin of the parent quark

Table 2-3: Observables to separate the contributions from initial and final states to the transverse single spin asymmetries. 2-scale processes are indicated in blue and 1-scale ones in black.

An important aspect of the Sivers effect, which has emerged from theory, is its process dependence and the color gauge invariance. In SIDIS, the quark Sivers function is manifested in association with a final state effect from the exchange of (any number of) gluons between the struck quark and the remnants of the target nucleon. On the other hand, for the virtual photon production in the Drell-Yan process, the Sivers asymmetry appears as an initial state interaction effect. As a consequence, the quark Sivers functions are of opposite sign in these two processes and this non-universality is a fundamental prediction from the gauge invariance of QCD. The experimental test of this sign change is one of the open questions in hadronic physics (NSAC performance measure HP13) and will provide a direct verification of QCD factorization. The COMPASS experiment at CERN is pursuing this sign change through DY using a pion beam and new initiatives have been proposed e.g. at FNAL.

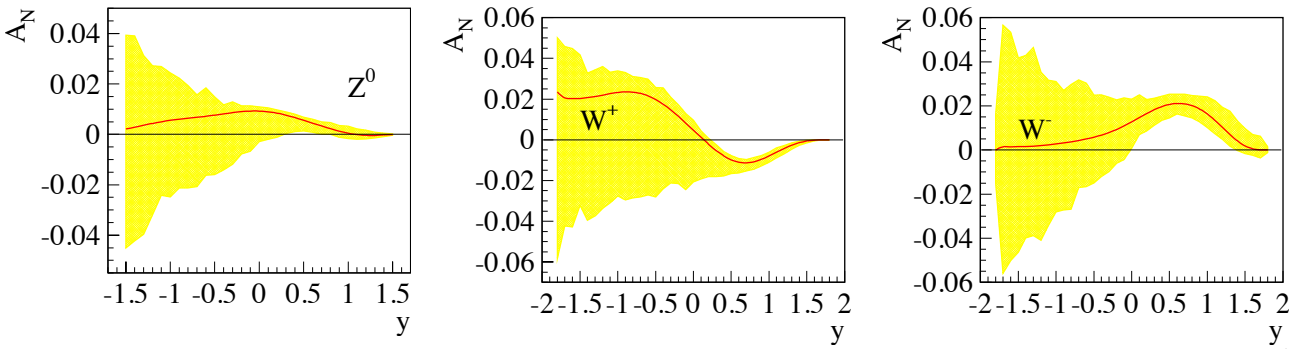

Figure 2-13: Theoretical predictions from reference [12] for the transverse single spin asymmetries for $W^{\pm}$ and Z^0 Bosons for 0 GeV <p_T< 3 GeV. The yellow bands represent the uncertainties for the asymmetry. At negative rapidity this is mainly caused by the currently unconstrained sea quark Sivers functions.

While the required luminosities and background suppressions for a meaningful measurement of asymmetries in Drell-Yan production are challenging, other channels can be exploited in p+p collisions which are similarly sensitive to the predicted sign change. These include prompt photons, $W^{\pm}$ and Z bosons, and inclusive jets. These are either already accessible with the existing STAR detector or need only modest upgrades and require continued polarized beam operations.

Figure 2-13 shows the most up-to-date theoretical predictions for the transverse single spin asymmetries for $W^{\pm}$ and Z^0 Bosons from reference [12] including TMD-evolution.

The transversely polarized data set in Run-11 at $\sqrt{s}$ = 500 GeV allowed STAR to reconstruct the transverse single spin asymmetries for A_N for $W^{\pm}$ and Z^0 Bosons. Especially the measurement of the A_N for $W^{\pm}$ Bosons is challenging where, contrary to the longitudinally polarized case, it is required to completely reconstruct the W-Bosons as the kinematic dependences of A_N can not easily be resolved through the high p_T decay lepton, for details see [12,13]. Due to the large STAR acceptance it was possible to reconstruct the W-Boson kinematics from the recoil jet, a technique used at D0, CDF and the LHC experiments to reconstruct the W-Boson kinematics. Figure 2-14 shows the transverse single spin asymmetries for A_N for $W^{\pm}$ as a function of the W-Boson rapidity y. The asymmetries have also been reconstructed as a function of the p_T of the W-boson. For the Z^0-Boson the asymmetry could only be reconstructed in one bin in y with the current limited statistics (25 pb^{-1}). Details for this analysis can be found in [14]. The analysis represents an important proof of principle similar to the first Run-9 $W^{\pm}$ A_L measurement.

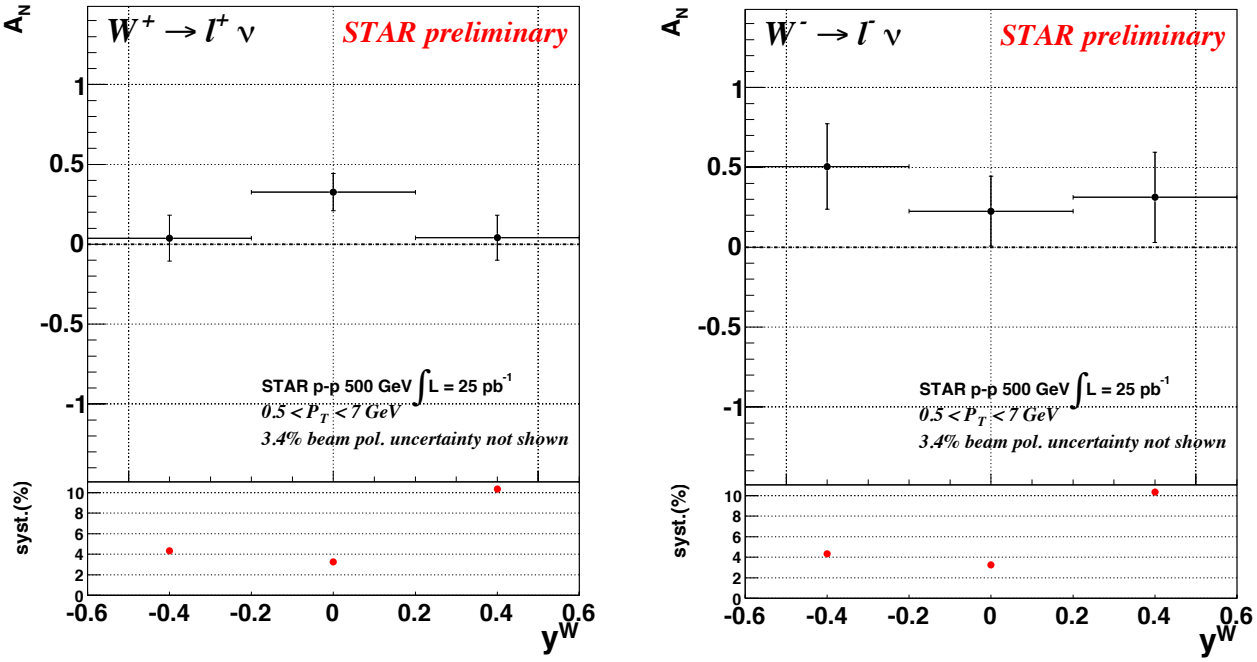

Figure 2-14: The transverse single spin asymmetries for A_N for $W^{\pm}$ as function of the W-Boson rapidity y.

$W^{\pm}$ bosons production due to is maximum parity violating nature provides an ideal tool to study the spin-flavor structure of sea quarks inside the proton. Such a measurement of the transverse single spin asymmetry will provide the world wide first constraint on the sea quark Sivers function in a x-range where the measured asymmetry in the $\bar{u}$ and $\bar{d}$ unpolarized sea quark distribution functions, as measured by E866 [15], can only be explained by strong non-pQCD contributions. At the same time, this measurement is also able to access the sign change of the Sivers function. Figure 2-15 shows the projected uncertainties for transverse single spin asymmetries of $W^{\pm}$ and Z^0 Bosons as function of rapidity and p_T for a delivered integrated luminosity of 400 (900) pb^{-1} and an average

beam polarization of 55%. The 400 (900) pb^{-1} correspond to 7 (14) weeks running with a dynamic β^* squeeze through the duration of a RHIC fill. The dynamic β^* squeeze provides a factor 2 increase of the luminosity in a fill, compared to Run-13, as the luminosity profile through the fill is kept flat.

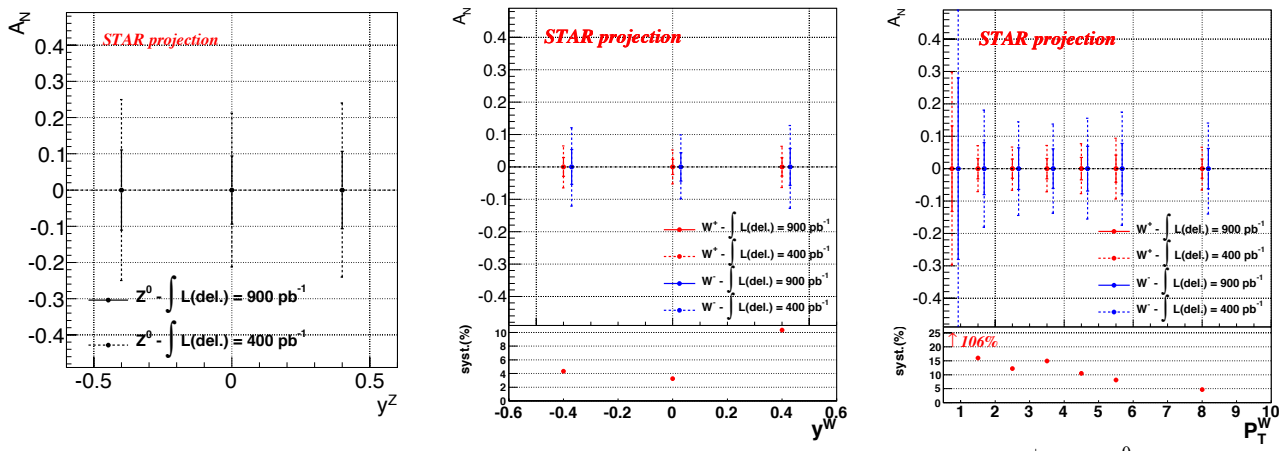

Figure 2-15: The projected uncertainties for transverse single spin asymmetries of $W^{\pm}$ and Z^0 Bosons as a function of rapidity and p_T for a delivered integrated luminosity of 400 (900) pb^{-1} and an average beam polarization of 55%.

Transverse single spin asymmetries in direct photon production provide a different path to access this sign change through the Twist-3 formalism. Figure 2-16 right shows the statistical and systematic uncertainties for the direct photon A_N. The asymmetry can be measured up to $x_F \sim 0.7$ where the π^0 asymmetries are largest. Figure 2-16 left shows the level of achieved background suppression for charged particles as well as photons from decays, i.e. π^0, using the forward meson spectrometer (FMS) and its preshower without any significant loss in the direct photon yield. Ideally, neutral pion asymmetries are measured simultaneously in the same x_F-range. Merged clusters in the FMS from pion decay become problematic at $p_z \approx 60$ GeV or more; here the preshower/converter will help to increase the signal/background fraction and extend the reach in x_F.

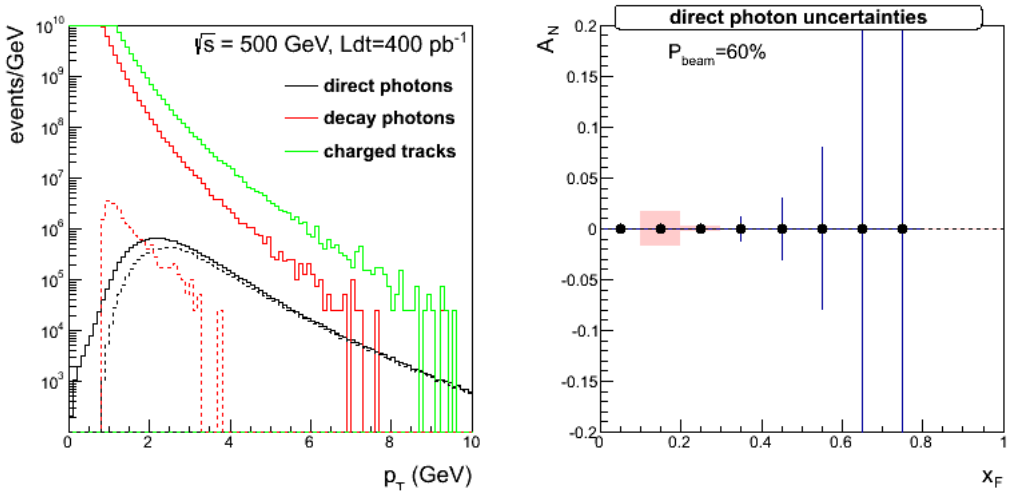

Figure 2-16: (left) The number of events at $\sqrt{s}$=500 GeV for a delivered luminosity of 400 pb^{-1} for direct photons, charged hadrons and photons from decays, i.e. π^0 before (solid) and after (dashed) detector responses have been applied. (right) Statistical and systematic uncertainties for the direct photon A_N after background subtraction.

The ultimate test for the TMD evolution would be to measure A_N for $W^{\pm}$, Z^0 Boson and DY production. To obtain a significant measurement of A_N for DY production, the DY leptons need to be detected at rapidities 2 to 4 for a lepton pair mass of 4 GeV and bigger. This is a highly non-trivial measurement, as backgrounds mainly due to QCD 2→2 processes need to be suppressed by a factor ~10^6. A first attempt to measure A_N for DY will be done during the 2016 run, using the FMS, preshower and a postshower. The FCS and FTS will provide the needed background suppression to reach a signal to background of 0.5 to 100 as function of the DY di-lepton mass. This would allow for a measurement with δA_N of 0.02 in 4 bins in rapidity for $2 < \eta < 4$. The COMPASS experiment at CERN is pursuing this sign change using a pion beam in the years 2015 and 2016.

As described above, for a complete picture of nucleon spin structure at leading twist one must consider not only unpolarized and helicity distributions, but also those involving transverse polarization, such as the transversity distribution, $h_1(x)$ [16, 17, 18]. The transversity distribution can be interpreted as the net transverse polarization of quarks within a transversely polarized proton [17]. Transversity is difficult to access due to its chiral-odd nature, requiring the coupling of the distribution to another chiral-odd distribution. Recently, semi-inclusive deep inelastic scattering (SIDIS) experiments have successfully probed transversity through two channels: asymmetric distributions of single pions, coupling transversity to the transverse-momentum-dependent (TMD) Collins fragmentation function [19], and asymmetric distributions of di-hadrons, coupling transversity to the so-called "interference fragmentation function" (IFF) [20] in the framework of collinear factorization. Taking advantage of universality and robust proofs of TMD factorization for SIDIS, the recent results [21, 22, 23, 24] have been combined with e^+e^- measurements [25, 26] isolating convolutions of Collins and IFFs for the first global analyses to extract simultaneously the transversity distribution and polarized fragmentation functions [27, 28]. In spite of this wealth of data, the kinematic reach of existing SIDIS experiments, where the range of Bjorken-x values don't reach beyond $x \lesssim 0.3$, limits the current extractions of transversity.

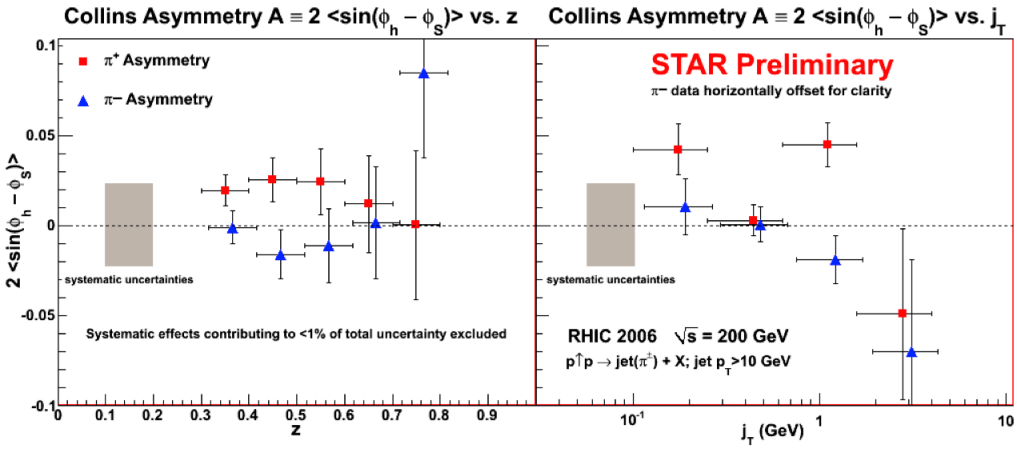

Figure 2-17: Preliminary Collins asymmetries for leading charged pions within jets produced with $|\eta| < 1$ and $p_T > 10$ GeV/c [29]. Asymmetries are shown as a function of pion z and j_T. Statistical uncertainties indicated by error bars, while systematic uncertainties are shown as shaded error bands.

As shown in Figure 2-17 and Figure 2-18, the STAR detector at RHIC has seen evidence of non-zero Collins [29] and di-hadron asymmetries [30] in preliminary data from $p^{\uparrow} + p \rightarrow jet + \pi^{\pm} + X$ and $p^{\uparrow} + p \rightarrow \pi^+ + \pi^- + X$ at $|\eta| < 1$ and $\sqrt{s} = 200$ GeV. These results are from 2.2 pb^{-1} of transversely polarized data with 58% polarization taken in 2006, and demonstrate for the first time that transversity is accessible from polarized proton collisions at RHIC. By accessing the Collins asymmetry through the distribution of pions within a jet, one may also extract the k_T

dependence of transversity, giving insight into the multidimensional dependence of the distribution. While TMD factorization is broken in p+p scattering, di-hadron asymmetries utilize collinear factorization. Thus, not only can more precise measurements of these effects in p+p improve our knowledge of transversity, such measurements may prove invaluable to understanding longstanding theoretical questions, such as the depth of any existing TMD factorization breaking. Extractions at RHIC kinematics also allow the possibility for understanding the TMD evolution of the Collins fragmentation function (e.g. Ref. [31]) by comparing to those extractions from SIDIS and e^+e^- data. Probing transversity in p+p collisions also provides broader access to the various quark flavors than is available in SIDIS.

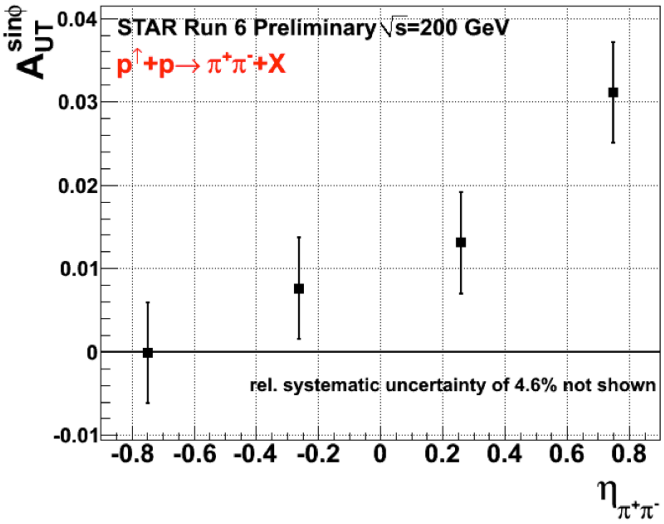

Figure 2-18: Preliminary di-hadron asymmetries for charged pions produced within $|\eta| < 1$ [30]. Asymmetries are shown as a function of di-hadron pseudorapidity. Error bars indicate statistical uncertainties.

Both the Collins and di-hadron asymmetries depend directly on the partonic spin transfer parameter $\hat{d}_{TT}$ which approaches unity as one moves toward forward scattering in the partonic center of mass, where $\cos\theta^* \to 1$. Furthermore, transversity remains quite poorly constrained for $x > 0.3$. To extend the measurements of transversity to the high x region has many important insights:

- one can access the tensor charge $\int_0^1 (\delta q^a(x) - \delta \bar{q}^a(x))dx = \delta q^a$ [32] a quantity essential to understand the nucleon structure at leading twist and calculable in lattice calculations.
- The difference between the helicity distributions and the transversity distributions for quarks and antiquarks provides a direct, x-dependent, measure of nonzero orbital angular momentum components in the wave function of the proton.
- current transversity extractions seem to indicate that the Soffer bound $\delta q(x,Q^2) < \left| q(x,Q^2) + \Delta q(x,Q^2) \right| / 2$ is violated, if proven by high statistics data at high-x it would have consequences on fundamental assumptions of strong interactions [33].

The planned STAR upgrades for the second half of this decade include expansion of the TPC tracking capability by about one half of a unit of pseudorapidity as well as charged-particle tracking capability and hadronic calorimetry to the forward subsystems, spanning the range $2.8 < \eta < 3.7$ [34]. Tracking upgrades are critically necessary for Collins and di-hadron measurements that require robust charge-sign discrimination. A more thorough discussion of these upgrades and their capabilities is given in section 3

In Figure 2-19 we show the expected Collins asymmetries for $p^\uparrow + p \to jet + \pi^\pm + X$ at $2.8 < \eta < 3.7$ and $\sqrt{s} = 500$ GeV. Jets are required to have a minimum p_T of 3 GeV/c. The 2008 transversity and Collins fragmentation function parameterization by the Torino group [27] has been inserted into a leading-order PYTHIA simulation using CDF Tune A. Jets are reconstructed

utilizing an anti-k_T algorithm, and the asymmetries are calculated relative to the associated hard-scattered parton. The projections assumed 1 fb^{-1} of luminosity with 60% beam polarization. Particle kinematics are reconstructed assuming a fast simulation for detector smearing based on a silicon forward tracking system and electromagnetic and hadronic caolorimetry. Asymmetries of nearly 2% are expected for both flavors of pions. In Figure 2-20 we show a comparison of di-hadron asymmetries at the "detector" level, with the fast simulation detector smearing, to those at the "particle" level, before simulated detector smearing. Based on the simulation, the effects of kinematic smearing to the asymmetries are expected to be quite small. This suggests that within the same subsystem, one can simultaneously measure in a robust fashion the Collins asymmetry within the TMD framework and the di-hadron asymmetry within the collinear framework. These measurements are critical for extending current understanding of transversity and questions concerning TMD evolution, factorization breaking, and universality, as well as longstanding questions about the nature of large inclusive asymmetries seen in p+p collisions.

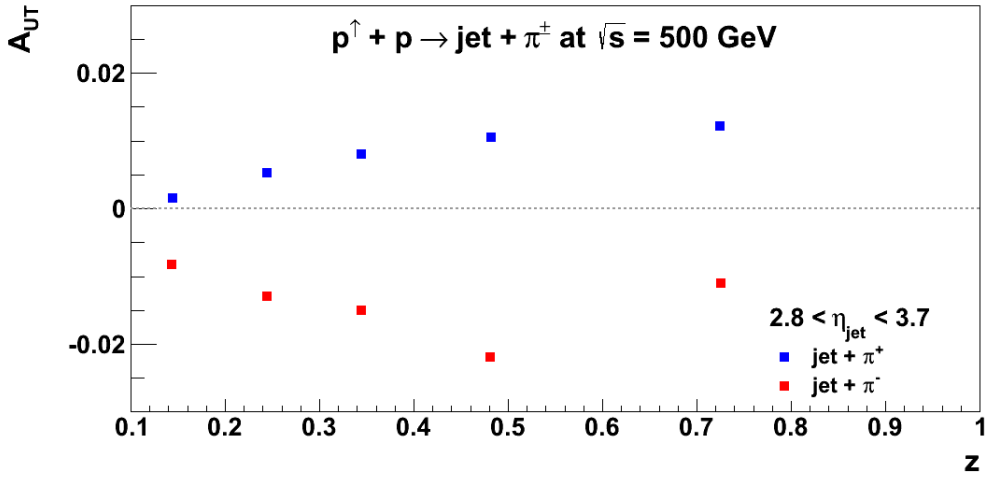

Figure 2-19: Expected Collins asymmetries assuming the Torino parameterization [27] within a leading-order PYTHIA Monte Carlo for charged pions within jets produced with $2.8 < \eta < 3.7$ and $p_T > 3$ GeV/c. The expectations assume 1 fb^{-1} of integrated luminosity, and statistical uncertainties are smaller than the size of the points. Jets are reconstructed utilizing an anti-k_T algorithm, and the asymmetries are calculated relative to the axis of the hard scattered parton.

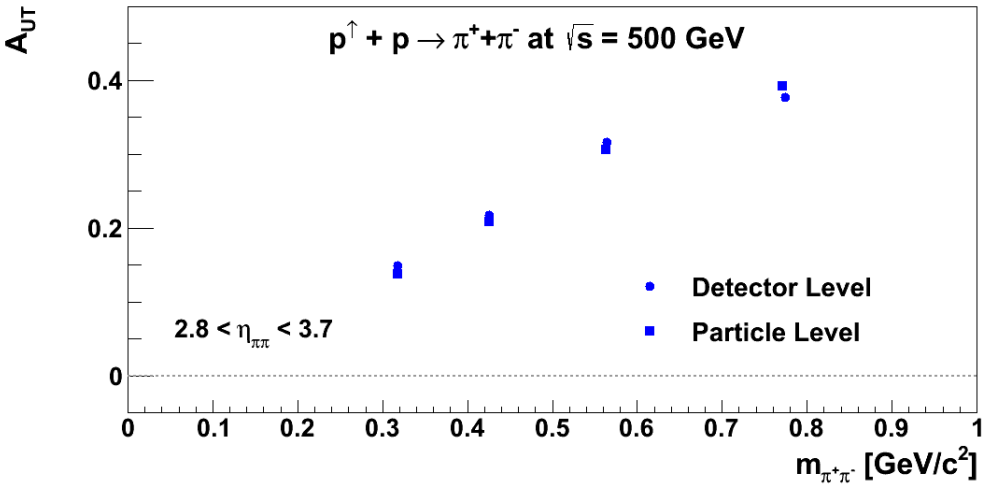

Figure 2-20: Comparison of IFF asymmetries at the "detector" level and at the "particle" level for charged pions produced within $2.8 < \eta < 3.7$. Asymmetries are shown as a function of di-hadron invariant mass, and assuming a parameterization inspired from fragmentation function measurements at Belle [26]. The projections assume 1 fb^{-1} of integrated luminosity, and statistical uncertainties are smaller than the size of the points.

In Figure 2-21 we show the expected Sivers asymmetries [35] for $p^{\uparrow} + p \rightarrow jet + X$ at $2.8 < \eta < 3.7$ and $\sqrt{s} = 500$ GeV. Jets are reconstructed in the same manner as discussed above for the Collins asymmetries, and the Torino parameterization is assumed for the Sivers function [27]. Since the inclusive jet asymmetry provides only a single hard scale, namely, jet p_T, the twist-3 framework is most naturally suited for theoretical interpretation. However, the current estimates give a sense for the size of such effects. One can see that for 1 fb^{-1} statistics may be sufficient to observe a nonzero asymmetry. However, the effects are expected to be quite small, at an order less than 1%. The magnitude of this projection is qualitatively similar to existing inclusive jet asymmetries at forward pseudorapidity [36].

Recent theoretical work [37] has found that by taking into account initial-state and final-state interactions between the hard scattered parton and the polarized remnant, extractions of the Sivers function from SIDIS data [21,22] are consistent with existing inclusive jet data from p+p scattering [36]. The extracted Sivers functions were used to derive the twist-3 function $T_{q,F}(x,x)$ [38] that was then used to compute the corresponding inclusive jet asymmetry for p+p scattering. The prediction compares favorable to the measured asymmetry, indicating a process-dependence to the Sivers effect. Due to the small size of the apparent inclusive jet asymmetries more precise measurements are needed.

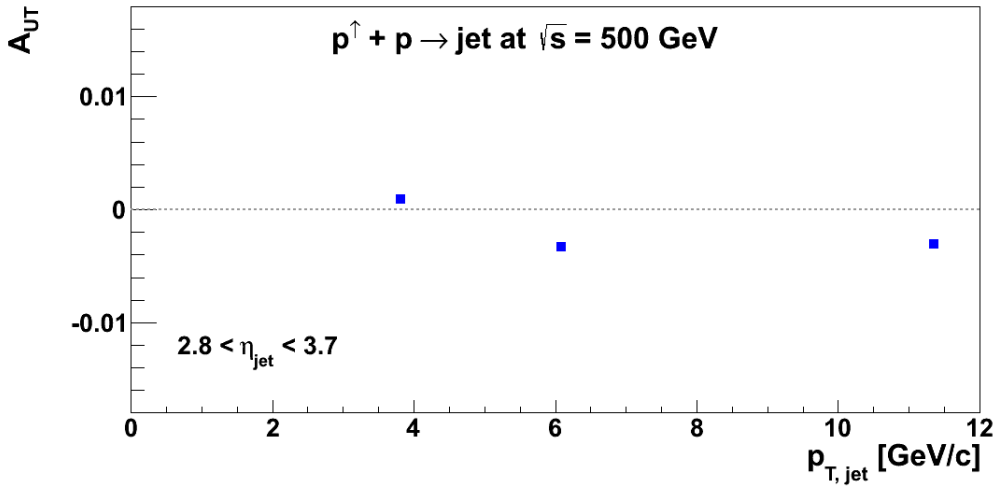

Figure 2-21: Expected Sivers asymmetries based on the Torino parameterization [27] within a leading-order PYTHIA Monte Carlo for jets produced with $2.8 < \eta < 3.7$ and $p_T > 3$ GeV/c. The expectations assume 1 fb^{-1} of integrated luminosity, and statistical uncertainties are smaller than the size of the points. Jets are reconstructed utilizing an anti-k_T algorithm, and the asymmetries are calculated relative to the axis of the hard scattered parton.

In addition to the inclusive jet measurements outlined above, di-jet measurement allow further probes of the transverse momentum dependent structure of the nucleon. Here the relative transverse momentum between the jets, k_T, gives the additional soft scale needed for the TMD framework. In addition, accessing functions like Sivers [35] and Boer-Mulders [39] in p+p collisions allows one to explore additional asymmetries that may result from the "color-entanglement" in p+p, which also leads to the breakdown of factorization theorems [40].

2.3 The Helicity Structure of the Proton

In the following we discuss by means of two premier examples, the longitudinal double spin asymmetry A_{LL} for di-jets and the longitudinal single spin asymmetry A_L for W-Bosons how STAR can further advance the knowledge of the gluon and sea quark polarization as function of Bjorken-x. STAR has or will have, after the forward upgrade described in this document is completed, measurement capabilities for several other channels, i.e. A_{LL} for direct photons, photon/hadron-jet correlations, di-hadrons, lambdas, that provide access to the gluon or sea quark polarizations. A detailed discussion about the STAR detector performance and the advantages and disadvantages of each of these channels is beyond the scope of this document.

Gluon polarization

Measurement of the gluon polarization in a polarized proton has been a major emphasis and strength of the spin physics program at RHIC since its inception [41]. RHIC has completed very successful polarized p+p runs at $\sqrt{s}$ = 200 GeV, $\sqrt{s}$ = 500 GeV, and $\sqrt{s}$ = 510 GeV. Table 2-4 summarizes the collision-energies, STAR recorded luminosities, and the average polarization values for runs since 2006.

Year	$\sqrt{s}$ (GeV)	Recorded Luminosity for longitudinally polarized p+p	<P>
2006	200	6.8 pb^{-1}	57
2009	200	25 pb^{-1}	55
	500	10 pb^{-1}	39
2011	500	12 pb^{-1}	48
2012	500	82 pb^{-1}	50/53
2013	510	300 pb^{-1}	50/53
2015	200	50 pb^{-1}	60

Table 2-4: STAR recorded luminosities for collisions of longitudinally polarized proton beams at the indicated center-of-mass energy for past runs since 2006. The bottom row reflects the STAR beam use request for 2015.

The past $\sqrt{s}$ = 200 GeV data have been analyzed and published [42,43,44,45]. The 2009 STAR data on the spin asymmetry A_{LL} in the inclusive production of jets are shown in Figure 2-22. They are particularly impactful in perturbative QCD analyses of world-data on polarized parton distribution functions, where they provide first direct evidence for positive gluon polarization in the Bjorken-x range $x > 0.05$ at a level similar to the combined quark and anti-quark polarization. Specifically, the STAR collaboration has evaluated the impact of the data on the knowledge of the polarized gluon distribution and its integral using the reweighting method developed by the NNPDF group [46], which allows to include new experimental data into an existing PDF set without the need to repeat the entire fitting process. The results are shown in Figure 2-23. The integral of $\Delta g(x,Q^2=10\ \mathrm{GeV}^2)$ over the range $0.05 < x < 0.5$ is 0.06 ± 0.18 for the original NNPDF fit and 0.21 ± 0.10 when the fit is reweighted using the STAR jet data. The DSSV group has performed a new global analysis [47] including the STAR jet A_{LL} results. They find that the integral of $\Delta g(x,Q^2=10\ \mathrm{GeV}^2)$ over the range $x > 0.05$ is $\mathbf{0.20^{+0.06}_{-0.07}}$ at 90% C.L., consistent with the value STAR finds by reweighting the NNPDF fit. This presents a highly significant advance over previous body of world-data, as is illustrated by comparison of the fit results in Figure 2-24, which is reproduced

from the new DSSV analysis [47]. The "new fit" includes 2009 jet A_{LL}, unlike the original DSSV and DSSV* fits which include the less precise 2006 data. A factor three improvement in uncertainty in Δg over the measured range in x is seen.

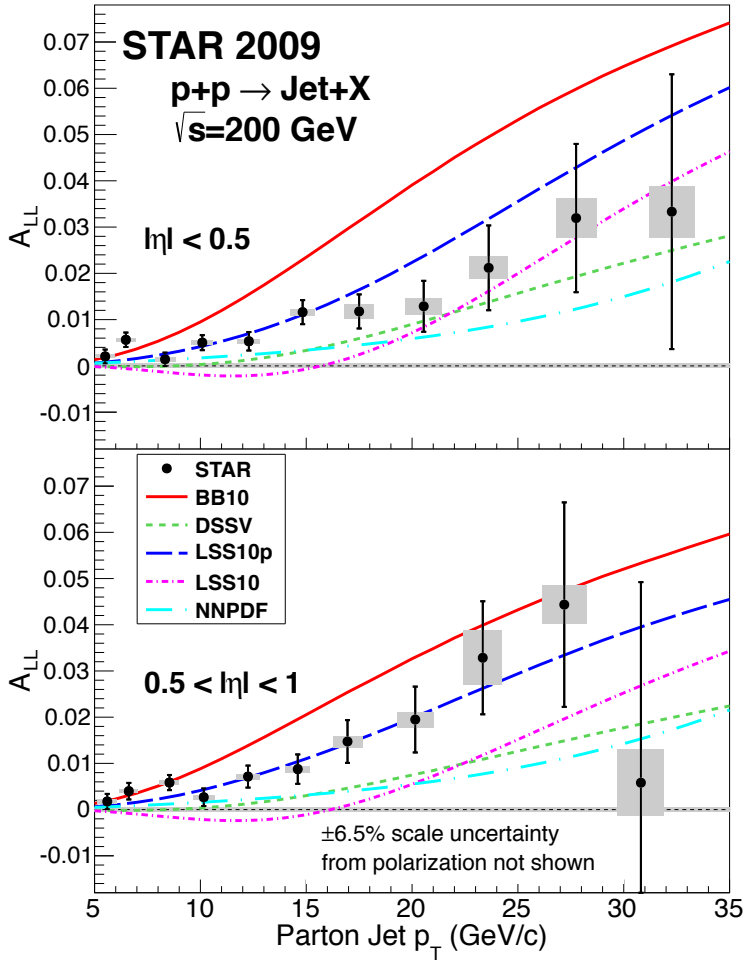

Figure 2-22 Midrapidity ($|\eta| < 0.5$, upper panel) and forward rapidity ($0.5 < |\eta| < 1$, lower panel) inclusive jet A_{LL} vs. parton jet p_T, compared to predictions from several NLO global analyses. The error bars are statistical. The gray boxes show the size of the systematic uncertainties.

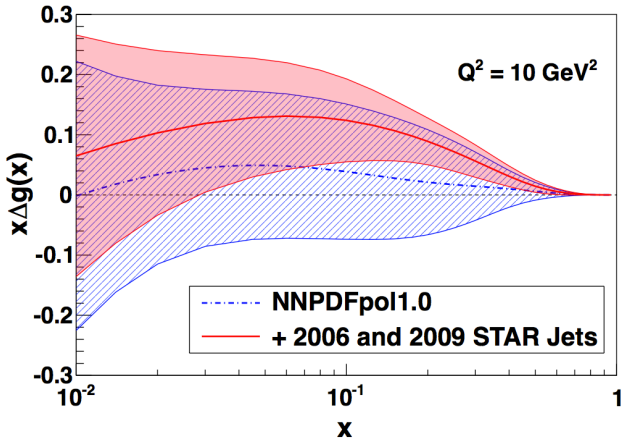

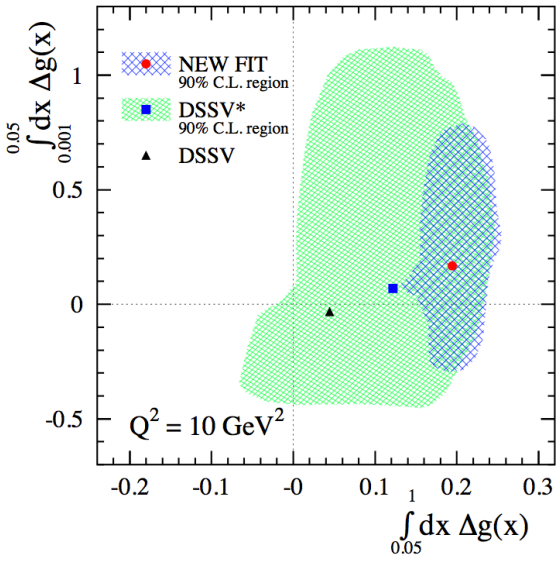

Figure 2-23: Gluon polarizations from NNPDF (blue dot-dashed curve, hatched uncertainty band), and from a modified version of NNPDF obtained by including the STAR 2006 and 2009 inclusive jet A_{LL} results through reweighting (red continuous curve and uncertainty band).

Figure 2-24: 90% confidence level areas in the plane spanned by the truncated moments of Δg computed for $0.05 < x < 1$ and $0.001 < x < 0.05$ at $Q^2 = 10$ GeV^2. Results for DSSV and DSSV* analysis, which include STAR 2006 data, and the new analysis [47] that includes the STAR 2009 data are shown.

The analysis of 2011-2013 data is in progress. Together with data the proposed running period in 2015, a further improvement by a factor of about two in precision is anticipated as shown in Figure 2-25 and Figure 2-26. The top-energy data will also extend to 2.5 times lower x values for equal jet p_T, down from $x \sim 0.05$ to $x \sim 0.02$.

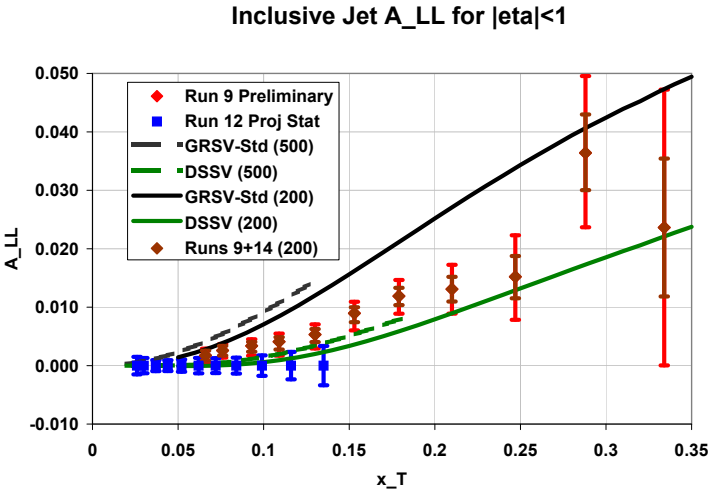

Figure 2-25: The expected precision for A_{LL} vs. p_T for inclusive jets at $\sqrt{s}$ = 200 GeV p+p collisions after the proposed Run-15 data are combined with the existing Run-9 measurements (brown diamonds). Also shown are the current Run-9 results (red diamonds) and the expected precision at $\sqrt{s}$ = 510 GeV from Run-12 (blue squares), together with model predictions for both energies from GRSV-Std and DSSV 2008.

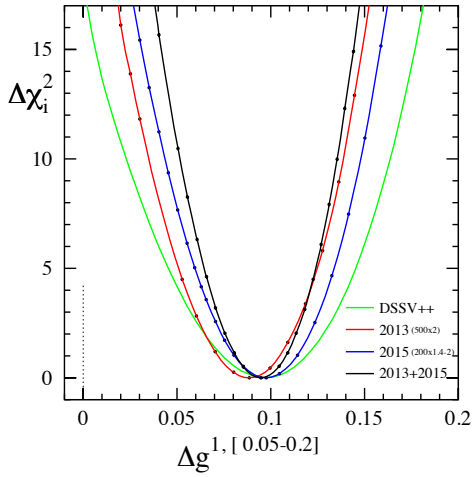

Figure 2-26: The improvement of the x^2 profile for the integrated gluon contribution in the x region currently probed at RHIC for $\sqrt{s}$ = 200 GeV. The different curves represent including different data sets, red including the $\sqrt{s}$ = 510 GeV data from Run-12 and Run-13 (red), blue including the expected data from Run-15 (blue) and black represent a fit to all data at once.

The contour of the truncated Δg integral for the measured and unmeasured x-region in Figure 2-26 demonstrates that the low-x region is of paramount importance to the understanding of the gluon spin contribution to the proton spin. Future STAR analyses and proposed measurements aim to address this issue by using correlated probes to gain more direct sensitivity to x-dependence than is possible with inclusive probes and by extending the measurements to forward pseudo-rapidity. The combination forms a world-wide unique opportunity prior to eRHIC.

Measurements of beam-spin dependence in di-jet production at STAR will allow better constraints of the underlying event kinematics to constrain the shape of the gluon polarization [48]. Initial di-jet measurements with relevant precision have been obtained from data collected during the 2009 running period, Run 9 [49]. The invariant di-jet mass, M, is related to the product of the initial partonic x values, $x_1 \cdot x_2$, in 2→2 processes, whereas the pseudo-rapidity sum $\eta_3 + \eta_4$ is related to the ratio x_1/x_2 of the partonic x values, since $M^2 = s \cdot x_1 \cdot x_2$ and $\eta_3 + \eta_4 = \ln(x_1/x_2)$ based on elementary four-vector kinematics. Measurements at both $\sqrt{s}$=200GeV and at $\sqrt{s}$=500GeV are preferred to maximize the kinematic region in x. The wide acceptance of the STAR experiment permits

reconstruction of di-jet events with different topological configurations, i.e. different η_3/η_4 combinations, ranging from symmetric ($x_1=x_2$) partonic collisions to asymmetric ($x_1 < x_2$ or $x_1 > x_2$) partonic collisions. It is in particular the access to the large η_3 / η_4 region which allows to probe gluons in QCD processes at very small x-values. The proposed new instrumentation for the forward region, discussed in section 3, would cover a nominal range in η of $2.5 < \eta < 4.0$.

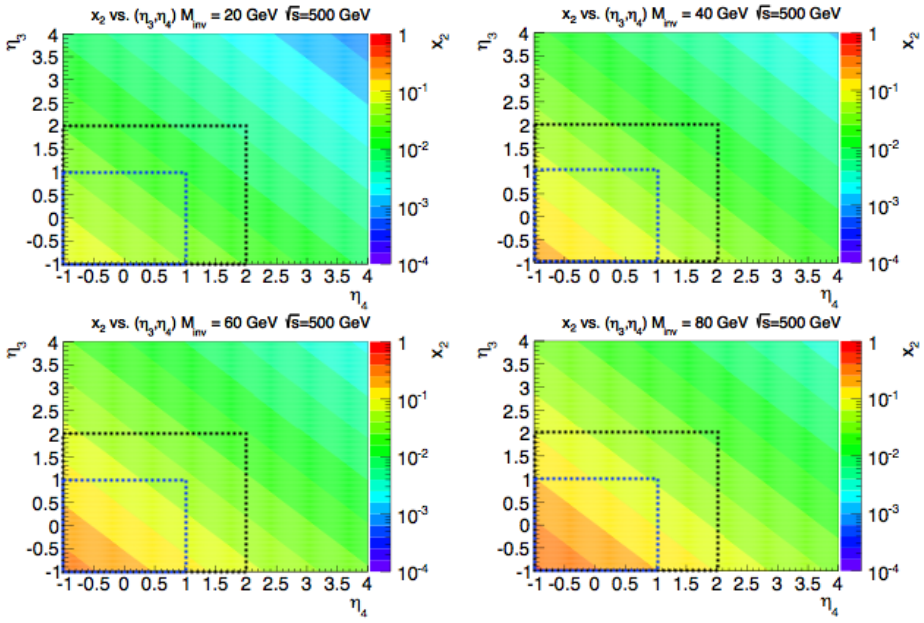

Figure 2-27: Low-x coverage (x_2) shown as a color shade for di-jet (2-to-2) final states showing η_3 and η_4 for four different invariant mass values of M = 20, 40, 60 and 80 GeV.

Figure 2-27 illustrates the lower x-range covered for a di-jet final state of four different invariants mass valves of M = 20, 40, 60 and 80 GeV displaying the actual x value in a color shade as a function of η_3 and η_4 for the current ($-1.0 < \eta < 2.0$) and future, proposed forward acceptance region ($2.5 < \eta < 4.0$). The black and blue dashed lines indicate the region for which results have been released (black) and the region for which STAR has been fully instrumented (blue) without yet releasing any results as of now. One can clearly see that the current η-range allows to probe a region in x of approximately $0.05 < x < 0.2$. Extending the current region to include the EEMC region of $1.1 < \eta < 2.0$ would extend the x range to at least 10^{-2}. Additional instrumentation at forward rapidity for $2.5 < \eta < 4.0$ would allow an extension to x values as low as 10^{-3}.

The kinematic range in x, the size of the invariant mass cross-section along with the projected uncertainties for di-jet longitudinal double-spin asymmetries A_{LL} have been evaluated using a MC framework at NLO level [50]. Those studies are based on the following assumptions:

- Jet efficiencies for the BEMC EAST and WEST region and EEMC region constrained by data ranging from ~30% at p_T=10GeV and rising to ~90% (95%) at p_T=20GeV (p_T=30GeV). For the forward acceptance region, it is assumed that a hadronic calorimeter system is available allowing conceptual larger efficiencies at the level of 90%.
- Asymmetric di-jet cuts in p_T have been chosen to be 5 GeV and 8 GeV.
- The systematic uncertainty is expected to be dominated by the relative luminosity (R) measurement relevant for the actual asymmetry measurement. An uncertainty of $\delta R = 5 \cdot 10^{-4}$ has been assumed for the projections presented here. This value was achieved for the Run 9 inclusive jet analysis. This value is therefore considered to be a conservative estimate for the

purpose of the di-jet A_{LL} projections presented here. Improvement will require continued analysis development and could entail also the addition of a new luminosity monitor to complement the existing luminosity monitors.

- Consistent with the assumptions in this document, a beam polarization of 60% and a total integrated delivered luminosity of 1000 pb^{-1} has been assumed with a ratio of 2/3 for the ratio of recorded to delivered luminosity. The assumed delivered luminosity would require that a full RHIC running period is devoted to 500 GeV operation.

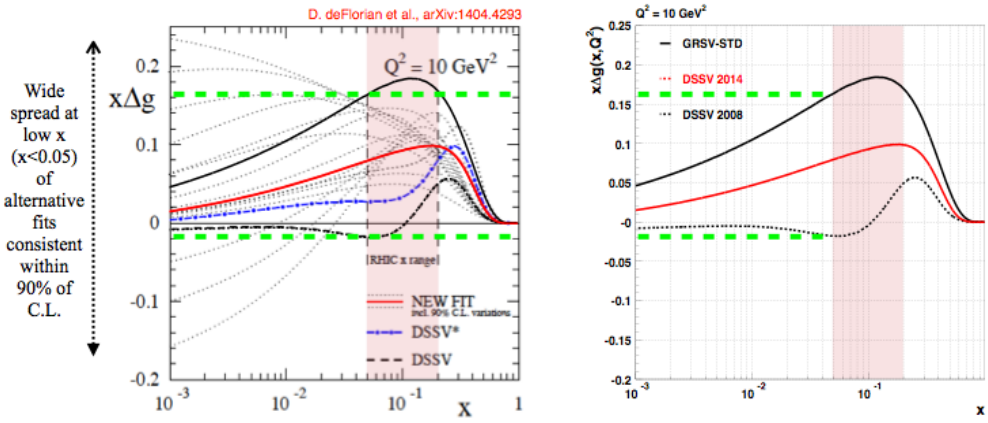

Figure 2-28: Comparison of DSSV (2008) and GRSV-STD to DSSV (2014). The range of DSSV (2008) and GRSV-STD is smaller than the 90% C.L. envelope provided by the DSSV (2014) global analysis.

Figure 2-28 shows a comparison of DSSV (2008) and GRSV-STD in comparison to DSSV (2014). Both DSSV (2008) and GRSV-STD have been used for all projection studies of A_{LL}. The recent DSSV (2014) analysis released an uncertainty envelope based on a fits at 90% C.L. which are shown as dotted lines in Figure 2-28. The range for DSSV (2008) and GRSV-STD is smaller than the 90% C.L. envelope for $x < 0.05$. The range in A_{LL} for DSSV (2008) and GRSV-STD is therefore not covering the full uncertainty range.

Figure 2-29 shows the x_1 / x_2 range for the current STAR acceptance region in η of $-1.0 < \eta < 2.0$ for six different topological di-jet configurations. The EEMC / EEMC configuration would permit probing x values around 10^{-2} and thus well below the current x region for which experimental results have been achieved. The size of the invariant mass di-jet cross-section is shown in Figure 2-30.

Figure 2-31 shows for the same topological di-jet configurations the actual asymmetries A_{LL} as a function of the invariant mass M. The theory curves at NLO level have been evaluated for DSSV and GRSV-STD where DSSV refers to the first global fit result including data at RHIC in polarized p+p collisions [51]. Both the statistical and also the systematic uncertainties are much smaller compared to the separation between DSSV and GRSV-STD.

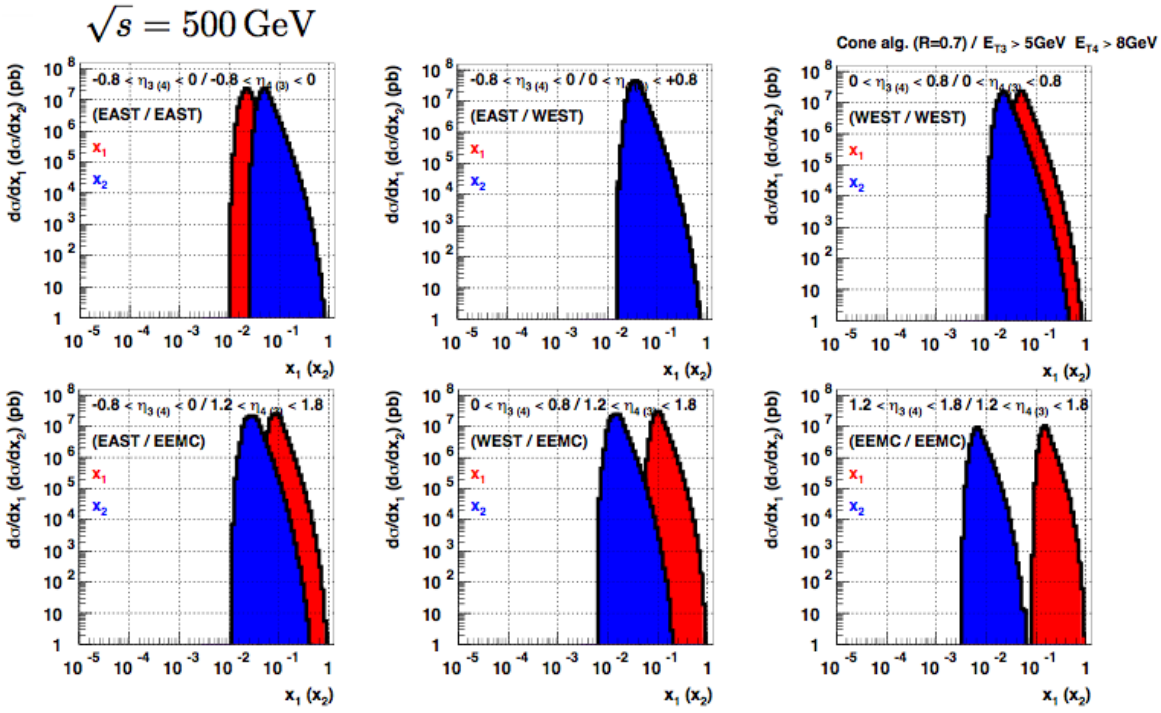

Figure 2-29: x_1 / x_2 range for the current STAR acceptance region in η of -1.0 < η < 2.0,

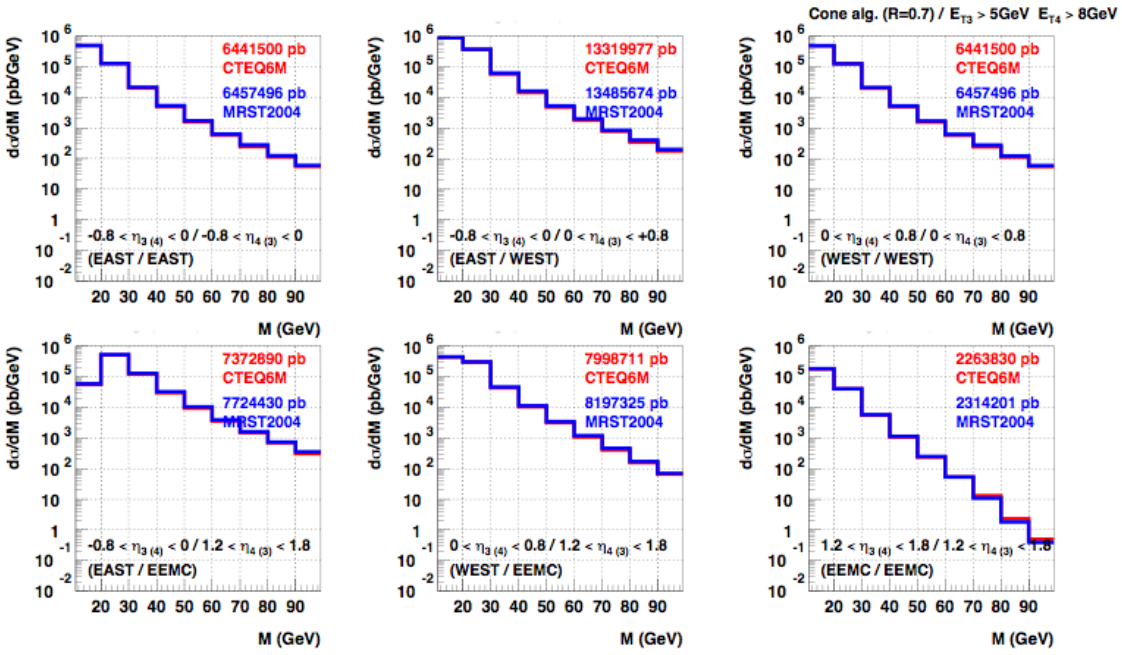

Figure 2-30: Invariant mass cross-section (NLO) for the current STAR acceptance region of -1.0 < η < 2.0.

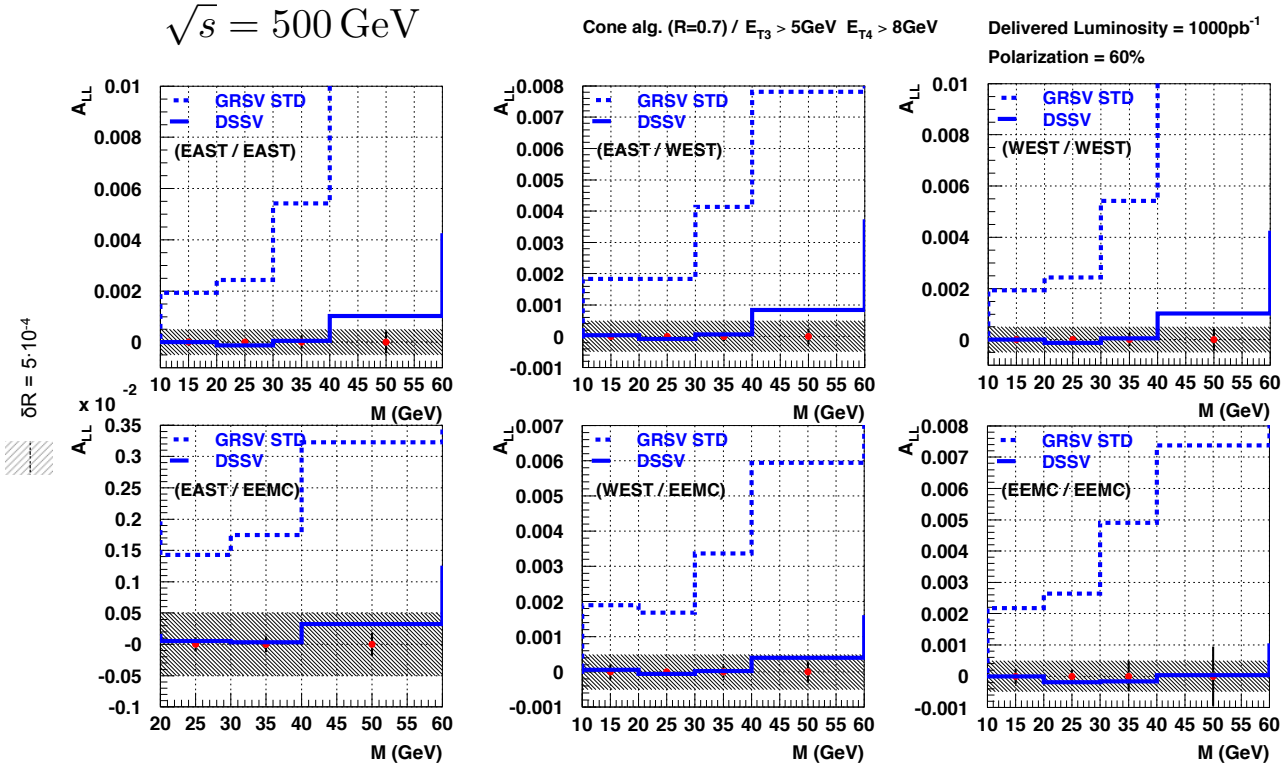

Figure 2-31: A_{LL} (NLO) for the current STAR acceptance region in η of -1.0 < η < 2.0 together with projected statistical and systematic uncertainties.

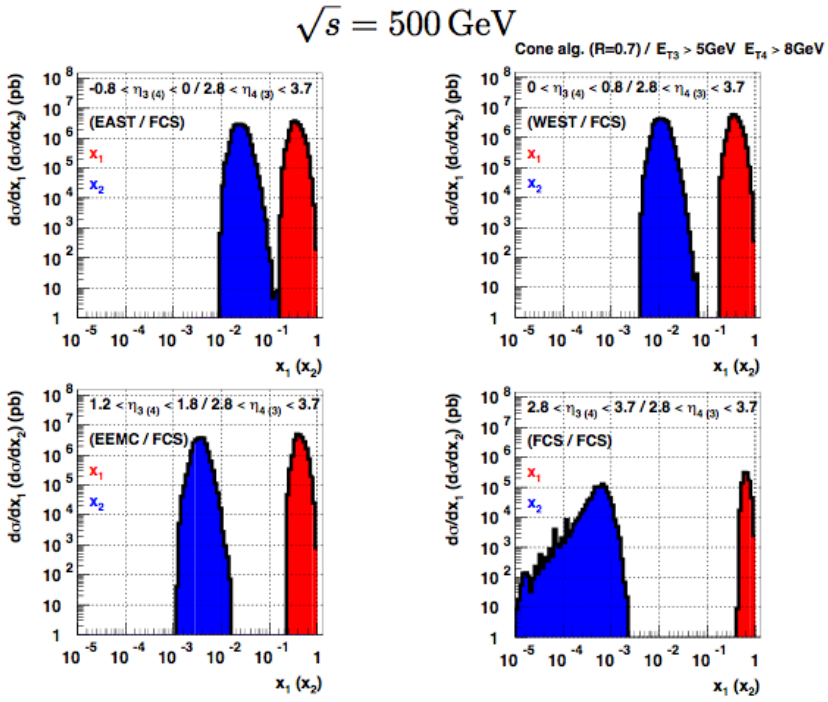

Figure 2-32: x_1 / x_2 range for the forward STAR acceptance region in η of 2.8 < η < 3.7.

Figure 2-32 shows the x coverage for four topological di-jet configurations involving at least the forward system labeled as FCS in combination with either EAST, WEST, EEMC and FCS. It is

in particular the EEMC / FCS and FCS / FCS configuration which would allow to probe x values as low as 10^{-3} in x. The size of the respective invariant di-jet mass cross-section is shown in Figure 2-33.

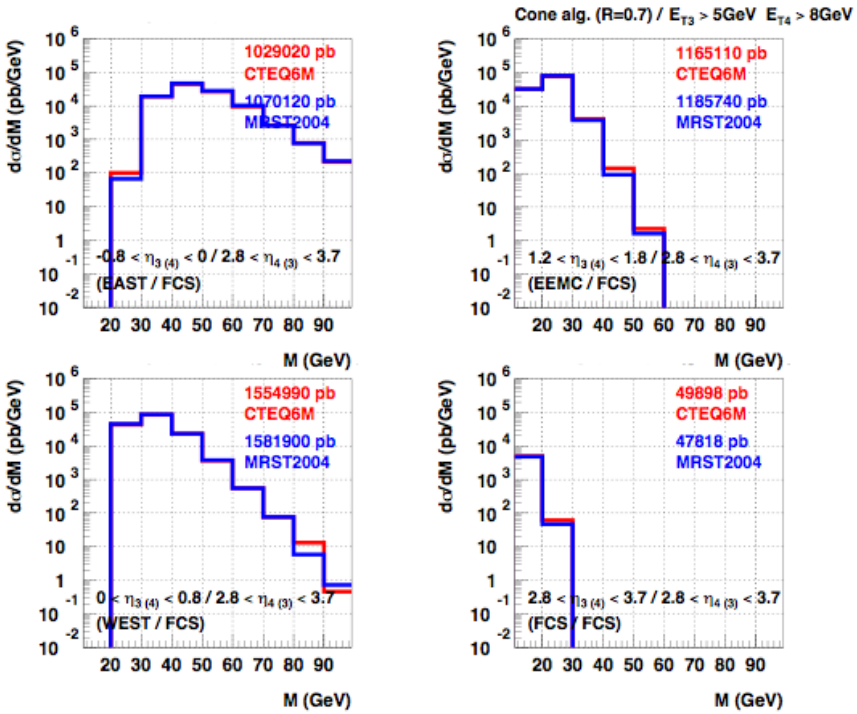

Figure 2-33: Invariant mass cross-section (NLO) for the forward STAR acceptance region of $2.8 < \eta < 3.7$.

Figure 2-34 shows for the same topological di-jet configurations the actual asymmetries as a function of the invariant mass M. The theory curves at NLO level have been evaluated for DSSV and GRSV- STD [52] where DSSV refers also to the first global fit result including data at RHIC in polarized p +p collisions [51]. The systematic uncertainty assumed to be driven by the relative luminosity uncertainty of $\delta R = 5 \cdot 10^{-4}$ is clearly dominating over the size of the statistical uncertainties. Any future measurements in this topological configuration of very forward measurements would clearly benefit from improved relative luminosity control and measurements. This also includes the expected benefit from a fully commissioned spin flipper system at RHIC. However, even with the assumed Run 9 relative luminosity result, a measurement of strong impact can be achieved comparing the A_{LL} curves for DSSV and GRSV-STD evaluated at NLO level. Such measurements would probe for the first time the unexplored kinematic region around 10^{-3} in x prior to a future Electron-Ion Collider program. The recent global analysis released by the DSSV group concludes that low-x data are 'badly needed' [47]. A measurement of forward di-jet production would provide such measurements. The size of the actual cross-section at FCS / FCS configuration is substantially smaller compared to all other configurations shown in Figure 2-33. Accessing this configuration is crucial to allow access to values in x even below 10^{-3}.

Figure 2-35 shows the correlation of the particle and detector di-jet mass based on a fast simulation framework discussed earlier. Good correlation is found for all four topological di-jet configurations. This study assumes only a forward calorimeter system. The impact of a tracking system based on either silicon disks or GEM disks would have only a marginal effect on the p_T reconstruction considering the STAR magnetic field configuration. However, a tracking system is expected to improve the actual localization and separation of jets, in particular for the FCS / FCS di-jet topology that gives access to the lowest possible values of Bjorken-x. High rate capability and efficiency are essential performance measures in particular for background rejection. A forward

hadronic calorimeter system is essential for efficient jet measurements. More detailed simulations are required to develop a full proposal. Besides di-jet correlation measurements, we anticipate to make measurements of π^0-jet correlations with a neutral pion reconstructed at forward rapidity as a systematic cross-check [53]. The NLO framework for hadron / hadron jet measurements exists [54]. The proposed forward di-jet production measurements, shown in Figure 2-34, in combination with measurements of the current STAR acceptance region (Figure 2-31) would allow to probe spin phenomena of gluons well below the region of $0.05 < x < 0.2$, which is currently accessible. Such measurements would provide critical initial insight into the nature of the proton spin. The proposed program offers unique and timely opportunities to advance the understanding of gluon polarization in the polarized proton, prior to a future Electron-Ion Collider that with sufficient energy will probe the x dependence of the gluon polarization to well below 10^{-3} in x with high precision [55].

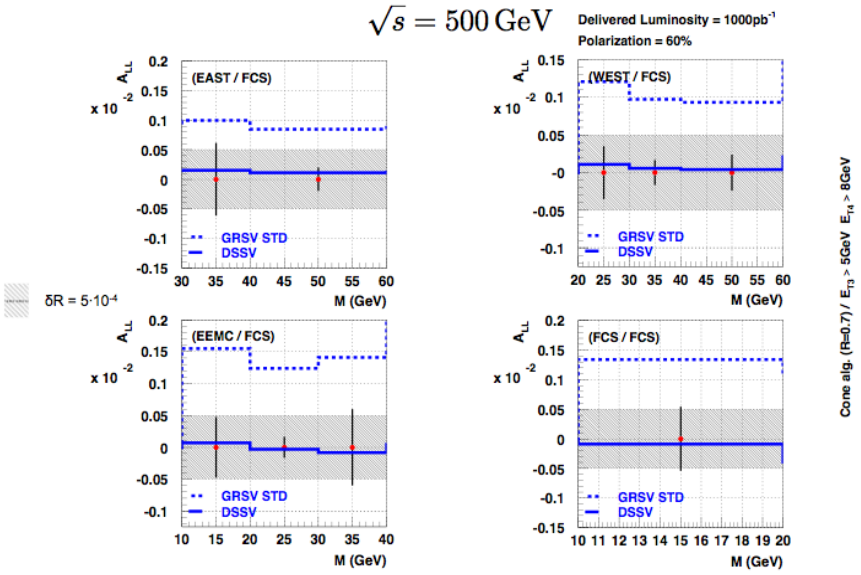

Figure 2-34: A_{LL} (NLO) for the forward STAR acceptance region in η of $2.8 < \eta < 3.7$ together with projected statistical and systematic uncertainties,

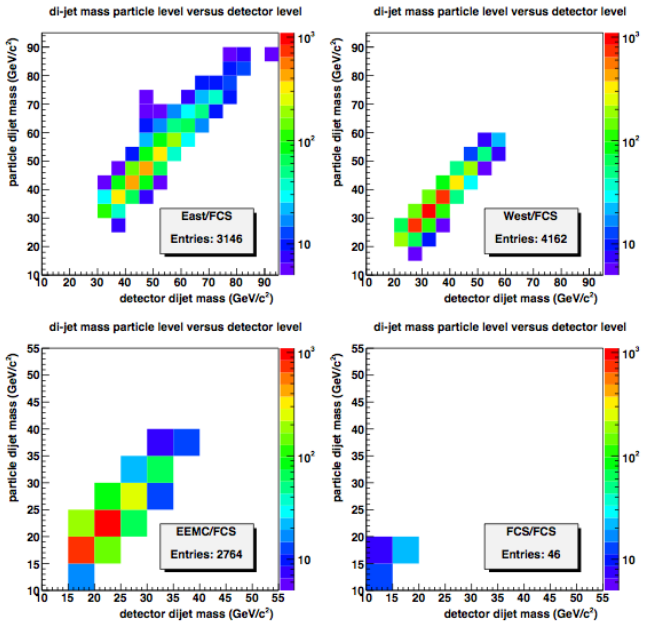

Figure 2-35: Correlation of the particle and detector di-jet mass including effects for the forward STAR acceptance region.

Quark polarization

A second main thrust of the RHIC spin physics program is the flavor delineation of the up and down quark and anti-quark polarizations in the polarized proton. The main observables are the single-spin asymmetries A_L in the production of W^+ and W^- boson and their calculable leptonic decays. Their measurement requires RHIC beam operations at top energy. The inaugural run at $\sqrt{s}$ = 500 GeV in 2009 yielded the first, proof-of-concept measurement [56]. The rapid analysis of the 2011 and the high statistics 2012 longitudinal polarized p+p data sets have delivered impactful results that will be further improved significantly once the analysis of 2013 is completed. Figure 2-36 shows the 2011 and 2012 combined result for the longitudinal single-spin asymmetry, A_L, for $W^{\pm}$ production as a function of lepton pseudorapidity η_e, in comparison to theory predictions.

The STAR preliminary A_L results based on the 2012 data set alone, have been included pQCD-fit by the DSSV group [57], where they result in a clear improvement on the determination of the polarization of the light sea quarks. For $\Delta\bar{u}$ a shift away from the current best mean value was observed, reflecting that the STAR W^- data at negative pseudorapidity tend to lie above the central curve based on DSSV fits to semi-inclusive and inclusive data. Already, with only the preliminary 2012 STAR data, the new global analysis showed a preference for $\Delta\bar{u} > \Delta\bar{d}$ in the range $x > 0.05$. The 2013 data will strengthen or refute these tantalizing initial observations, and may provide additional motivation for continued $\sqrt{s}$ = 500 GeV longitudinal running, concurrent with the proposed Δg program.

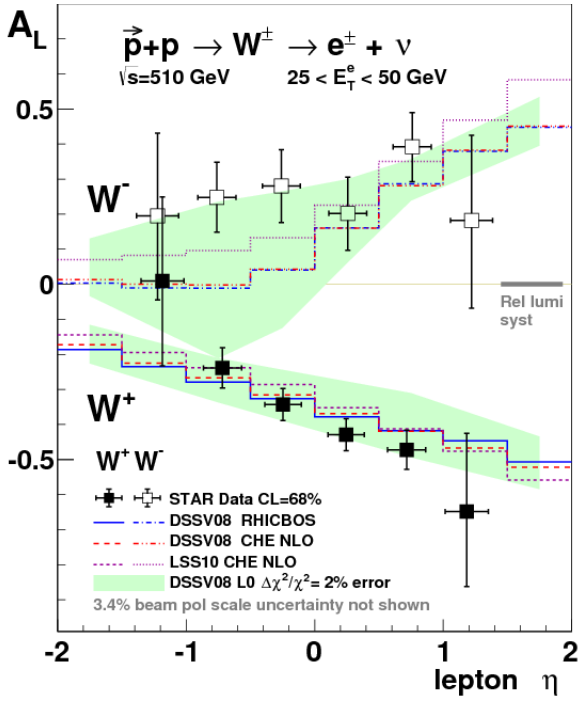

Figure 2-36: Longitudinal single-spin asymmetry, A_L, for $W^{\pm}$ production as a function of lepton pseudorapidity η_e, in comparison to theory predictions.

2.4 The Search for Exotics in p+p

Glueballs at RHIC:

QCD predicts the existence of bound states of gluons with no constituent quarks, glueballs [58]. An existence proof and characterization of these compound objects offer unique insight into the strong interaction since the gluon self-interaction is exclusively responsible for the mass of glueballs. The search for these exotic states and their possible role within the family of $q\bar{q}$ mesons is a long-standing quest in hadron spectroscopy [59]. Glueballs are preferentially produced in gluon-rich processes such as $p\bar{p}$ annihilation [60, 61, 62], the radiative decay of the J/ψ-meson [63, 64], and central exclusive production (CEP) [65, 66, 67, 68, 69, 70] in $pp(\bar{p})$. The CEP at high-energies is a process in which glueballs are supposed to be copiously produced. In CEP, two protons are scattered diffractively into the forward direction without exchanging valence quarks through double Pomeron exchange (DPE). The absence of valence quarks in the production process makes CEP a favorable place to look for hadronic production of glueballs. RHIC can be exploited to study the potential for producing such exotic meson states through the glue-rich production mechanisms.

DPE processes create two rapidity gaps between the beam rapidities and the central region. The process is defined as $p + p \rightarrow p + M_X + p$ and all of the energy lost by the initial protons during the interaction is used in the production of the central system M_X. Theoretical predictions of the evolution of the different exchange mechanisms with center of mass energy $\sqrt{s}$ suggest that Reggeon-Reggeon and Reggeon-Pomeron exchange mechanisms are expected to decrease with energy as s^{-1} and $s^{-0.5}$ while in the double Pomeron exchange mechanism, Pomeron-Pomeron remains a constant [71]. That implies that to relatively suppress Reggeon contributions in double diffractive processes, the center of collision energy needs to be sufficiently high, where also larger rapidity gaps are expected. At $\sqrt{s}$ = 500 GeV, where the beam rapidity is 6.3, ~5 units of symmetric rapidity gaps leave ~2 units of central rapidity region, which is expected to give a good kinematic coverage to reach $M_X \sim 3$ GeV/c^2 assuming the central rapidity spans $2\log(M_X/M_p)$. Since the Pomeron is assumed to carry vacuum quantum numbers, Pomeron-Pomeron can only yield states with $I^G J^{PC} = 0^+0^{++}$ and 0^+2^{++} for the lowest-lying states. Identifying that the leading exchange process is dominated by double Pomerons requires observing suppression of vector and pseudo-vector mesons such as the ρ meson in the process, since they cannot be formed from two states with $I = 0$. While ρ can also be produce by the central exclusive photoproduction in p+p, the production cross-sections are expected to be significantly smaller compared to the DPE processes at high energies as observed at ISR ($\sqrt{s}$ =62 GeV) [72] and LHC ($\sqrt{s}$ =7 TeV) [73]. The energy dependent decrease of ρ production in central productions has been observed by WA92 ($\sqrt{s}$ = 12.6 GeV) and WA102 ($\sqrt{s}$ = 23.8 GeV) [74], which experimentally supports the suppression of the non-DPE mechanism as the center of mass energy increases in the diffractive processes. But abundant production of the $a_1(1260)$ measured by WA102 ($\sqrt{s}$ =29.1 GeV) [75] calls the hypothesis that the leading contribution in central production at this energy regime is Pomeron-Pomeron into question. Also the angular distribution of some produced $q\bar{q}$ mesons at this energy behaves as in photon-photon fusion, which leads to their interpretation as the vectorial interaction of Pomerons, but it also can be attributed to have a significant contribution from Reggeons. At $\sqrt{s}$ = 500 GeV, it is expected that the dominance of the Pomeron-Pomeron process in the central region is more likely to occur. Even though the spin structure of the Pomeron coupling is yet to be fully explored, non-trivial spin effects are expected to be insignificant in the Pomeron dominated inelastic diffractive process at high-energy. Since RHIC can provide protons with transverse and longitudinal polarization, studying spin dependence in DPE processes will potentially provide an extra constraint in filtering Pomeron induced double diffractive processes.

Tagging forward protons with Roman Pots at STAR (Phase II*):

Although identification of a rapidity gap can be utilized for studying diffractive processes, it is imperative to tag and reconstruct the forward proton to eliminate possible ambiguities of a rapidity gap tag, which can be contaminated by background due to low multiplicity non-diffractive processes. The rapidity gap tag also does not provide information on whether the initial proton remains intact after the collision or is excited into a low-mass state with small energy loss, which could still yield a rapidity gap. Tagging forward protons, i.e., detecting scattered protons in a diffractive process requires reaching inside of the beam pipe since the scattering angles are very small, of the order of a few *m*rad and smaller. By detecting the scattered proton in Roman Pots (RPs), one can reconstruct its momentum from the measured positional and directional information of the protons in the given beam optics.

For the initial phase of the new program (Phase I), which probes the small-*t* region, the Roman Pots used for the pp2pp experiment have been integrated with the STAR detector. They are positioned at 55.5 m and 58.5 m from the nominal interaction point (IP). The schematic layout of the RPs is shown in Figure 2-37. Each RP contains four planes of silicon strip detectors ($75\text{x}45\text{mm}^2$) (two vertical and two horizontal) to provide redundancy for the track reconstruction. During RHIC Run-9, 70M of events, including 30M of elastic events, were successfully taken with the Phase I set-up [76].

For Phase II*, the RP system will be moved to be installed between RHIC DX-D0 magnets, at 15.8 m and 17.6 m from the IP as shown in Figure 2-37 and Figure 2-38, extending the acceptance and the reach in four-momentum transfer t for a more optimized setting for diffractive events with larger $|t|$. An additional RP station is planned to be installed with each vertical station with larger Si-Detector ($100\text{x}70\text{mm}^2$), which is considered as a full RP upgrade, RP Phase II.

Figure 2-39 shows the expected *t*-distributions for the scattered protons measured in the RPs in the Phase II* and Phase II setup at = 500 GeV. The acceptance in the high-*t* region for the Phase II set-ups are limited by the aperture of the DX magnet. Since no special accelerator optics is required in the configuration for the Phase II*, II set-ups, running in parallel with other physics program in STAR is possible, and we will be able to utilize high luminosity in the search for rare physics processes.

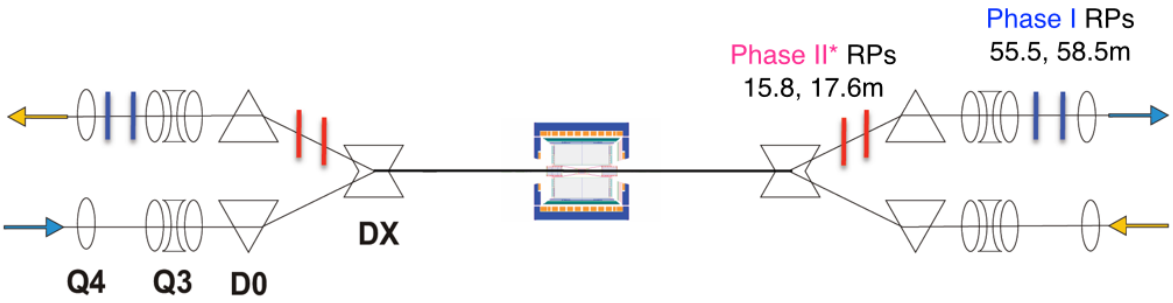

Figure 2-37: The layout of the RPs with the STAR detector (not to scale). The Phase I RPs setup to detect scattered protons with low-*t* are located after two dipole magnets (DX, D0) and three quadruples at 55.5 m and 58.5 m from the interaction point (IP), respectively. For measuring protons with higher-*t* (Phase II*), sets of RPs will be positioned between DX and D0 magnets, at 15.8 m and 17.6 m from IP.

In Figure 2-41, a preliminary measurement of the invariant mass spectrum of the $\pi^+\pi^-$ pairs produced in the central exclusive process $p+p \rightarrow p+M_X(\pi^+\pi^-)+p$ with RP Phase I set-up is shown. The data were obtained with the STAR detector at $\sqrt{s}$ = 200 GeV in 4 days running during Run-9. The Roman Pots (Phase I set-up) were used to tag forward protons and the invariant mass of the pion pair was obtained using tracks reconstructed in the TPC. To select CEP events the balance of momenta of the outgoing protons and central $\pi^+\pi^-$ pair was required.

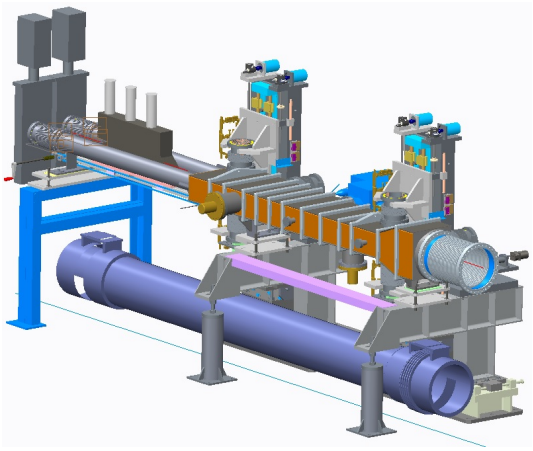

Figure 2-38: Design of the new DX-D0 chamber showing the two vertical Roman Pot stations. The installation will be done in 2014.

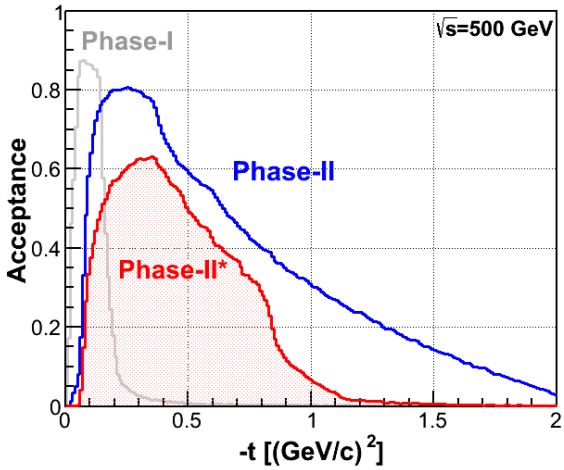

Figure 2-39: Acceptance of protons from DPE processes in p+p at √s = 500 GeV as function of *t* for Phase-II (blue) and Phase-II* (red) configuration. The acceptance for Phase-I setup is also shown (grey) for comparison.

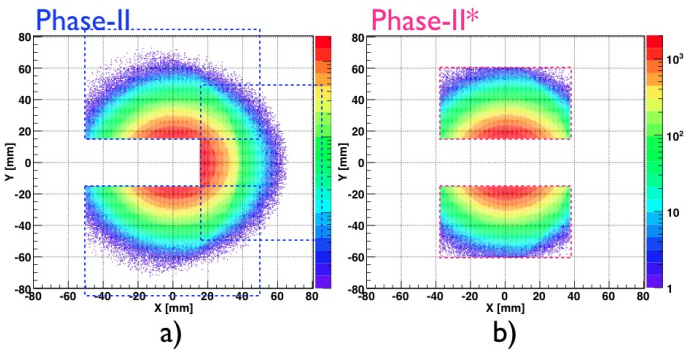

Figure 2-40: Distributions of protons at the upstream RPs for Phase-II (a) and Phase-II*(b) configurations. The detector coverage is shown with dotted boxes.

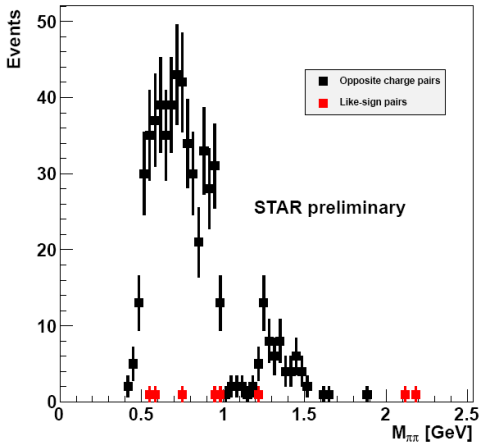

Figure 2-41: Invariant mass distributions for two opposite charged pions in the exclusive central diffraction in $p + p \rightarrow p + M_X(\pi^+\pi^-) + p$ at $\sqrt{s}$ = 200 GeV. The distribution in red is non-exclusive

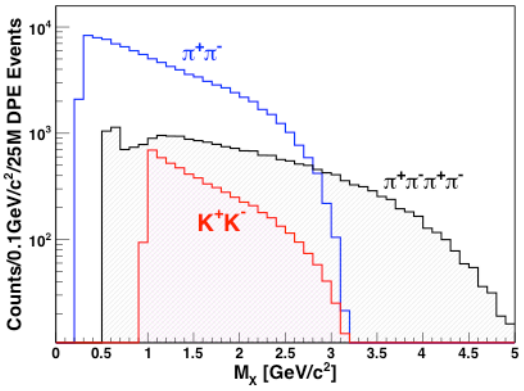

Figure 2-42: Estimated accepted phase-space distributions of invariant mass *MX* decaying into $\pi^+\pi^-$, $\pi^+\pi^-\pi^+\pi^-$ (hatched) and K^+K^- (cross-hatched) from 25M DPE events simulated in

background estimated from events with like-sign charge pion pairs. Shown uncertainties are statistical only.

$p + p \rightarrow p + M_X + p$ at $\sqrt{s}$ = 500 GeV with Phase II set-up.

Central Exclusive Production (CEP) in proton – proton collisions:

Lattice QCD calculations [77] have predicted the lowest-lying scalar glueball state in the mass range of 1500-1700 MeV/c^2, and tensor and pseudo-scalar glueballs in the range of 2000-2500 MeV/c^2. Experimentally measured glueball candidates for the scalar glueball states are the $f_0(1500)$ and the $f_0(1710)$ in central production as well as other gluon-rich reactions. The glueballs are expected to be intrinsically unstable and decay in diverse ways, yielding typically two or more mesons. The $f_0(1710)$ state is expected to decay into $K\bar{K}$ and the $f_0(1500)$ into $\pi\pi$ and 4π. For the tensor meson sector $I^G J^{PC} = 0^+2^{++}$, the established ($f_2(1950)$) and not-well established states such as $f_2(1910)$, $f_2(2150)$, have been less explored. The challenge is partly due to a small production cross-section and also not being able to clearly separate the Reggeon contribution complicated by nearby $q\bar{q}$ mixing and interpretation.

One of the challenges in identifying a glueball state unambiguously lies in difficulties of isolating a glueball state from the conventional meson state that shares the same quantum numbers. To first identify that the diffraction process is dominated by gluon-rich DPE, the leading quantum number of the centrally produced system is required to be made of two vacuum quantum numbers. From the DPE process, to filter potential gluon binding processes, kinematic variables can be utilized.

Correlations of transverse momentum of scattered protons in CEP have been suggested as a means to discriminate different intrinsic structures of the centrally produced object ("glueball-filter") [78]. A possible dynamics behind the filtering mechanism is that small momentum transfer processes are expected to enhance *gg* kinematic configurations since the gluons can flow directly into the final state in the process.

It is not theoretically well known, how the mixing between glueballs and nearby $q\bar{q}$ states will play a role in the dynamics of glueball candidates. The energy regime, where glueball candidates from central production have been identified so far are estimated to be significantly from non-DPE processes. It is imperative that wide kinematic and acceptance coverage is available to extract information of the production of glueball candidates at an energy regime where double Pomeron exchange is expected to be a dominant process in the double diffractive process.

Data Collection at $\sqrt{s}$ = 200 and 500 GeV:

With Phase II* setup:

With the Phase-II* in Run-15, we expect to collect a data sample in a wider-*t* range, while the data taking is done simultaneously with the rest of the STAR program, allowing for much larger statistics as compared to that taken in Run-9 (Figure 2-41). It is estimated that with 5 weeks of pp running in Run-15 with an integrated luminosity of 40 pb^{-1} recorded, we can collect > 1.5×10^5 exclusive $\pi^+\pi^-$ events (> 15k in 1< M_X < 2 GeV/c^2) for analysis. The estimate was done with assumptions $dN/dt \propto \sigma(\pi\pi)$ and the exclusive data sample collected during Run-9. With the luminosity of $\mathcal{L}$> 10 ^{30} cm^{-2}s^{-1}, the data taking rate for the CEP events is expected to be limited by DAQ, and the assumed rate for the CEP data collection is 200 Hz. Given the larger-*t* range covered by the Phase II* RPs compared to Run-9 (Phase I), the purity of the CEP trigger is expected to be much improved due to the decrease of the elastic backgound. With the improvements we will likely collect $\mathcal{O}$(100K) exclusive CEP events in the mass region of 1-2 GeV/c^2 which warrants a sample enables differential spin-parity analysis of the exclusively produced states.

With Phase II setup:

Data taking with the Phase-II RP setup will enhance the acceptance at high-t significantly from having an additional plane in horizontal direction. Figure 2-39 shows accepted t distributions of protons from DPE processes in p+p at $\sqrt{s}$ = 500 GeV for Phase II and Phase II* configurations. The detectors in horizontal/bending plane cover protons with large momentum loss (large-t) as shown in Figure 2-40. Additionally more complete coverage in azimuthal angle with the additional horizontal plane will introduce less bias and corrections in spin-parity analysis of the centrally produced system.

The t coverage scales approximately with p^2_{beam}, the maximum reach of $|t|$ is 6.25 times larger at $\sqrt{s}$ = 500 GeV, which will enhance dynamic range of the potential glueball production in CEP process. Non-Pomeron initiated background in CEP is also expected to be further suppressed at 500 GeV. The expected reconstructed kinematic phase-space distributions of centrally produced system decaying into pions and kaons at $\sqrt{s}$ = 500 GeV are shown in Figure 2-42. The invariant mass range 1-2.5 GeV/c^2 is kinematically well accessible in pion and kaon decay channels. With high-luminosity pp running at $\sqrt{s}$ =500 GeV with full Phase II RP set-up, a high statistic CEP sample can be obtained in an expanded range, especially at large-t region, enabling differential spin-parity analysis of the centrally produced states to study glueball production with wide dynamic sampling.

2.5 The Nucleus as a Laboratory for QCD

Our quest to understand QCD processes in Cold Nuclear Matter (CNM) centers on the following fundamental questions:

- *What are the dynamics of partons at very small and very large momentum fraction (x) in nuclei, and at high gluon-density. What are the nonlinear evolution effects (i.e. saturation)?*
- *What are the pQCD mechanisms that cause energy loss of partons in CNM, and is this intimately related to transverse momentum broadening?*
- *What are the detailed hadronization mechanisms and time scales and how are they modified in the nuclear environment?*

Various aspects of these questions are being attacked by numerous experiments and facilities around the world. Deep inelastic scattering on nuclei addresses many of these questions with results from HERMES at DESY [79], CLAS at JLab [80], and in the future at the JLab 12 GeV upgrade and eventually an Electron-Ion Collider [81]. This program is complemented with hadron-nucleus reactions in fixed target p+A experiments at Fermilab (E772, E886, and soon E906) [82] and at the CERN-SPS. The combination of RHIC p+Au and LHC p+Pb data provides an unprecedented large lever-arm in center-of-mass energy and makes a beam-energy scan at RHIC, modulo surprising discoveries, not the highest priority for upcoming p+A runs. The unique ability of RHIC to run different beam species on the other hand, will be one of the priorities in p+A runs at the end of the decade.

Physics of high Gluon Densities and low-x in Nuclei

The main emphasis of the 2015 and later p+A runs is to determine the initial conditions of the heavy ion nucleus before collision. Our current understanding of nuclear parton distribution functions (nPDFs) is still very limited. Figure 2-43 shows a summary of some of the most recent nPDFs. The central values and their uncertainties for up-valence quarks, up-sea quarks and gluons are shown. The yellow bands indicate regions in x where the fits are not constrained by data [83]. This plot shows clearly that high precision data over a wide x-Q^2 range are needed. Such data are

needed for different nuclei as the A-dependence of nPDFs cannot be predicted from first principles in pQCD.

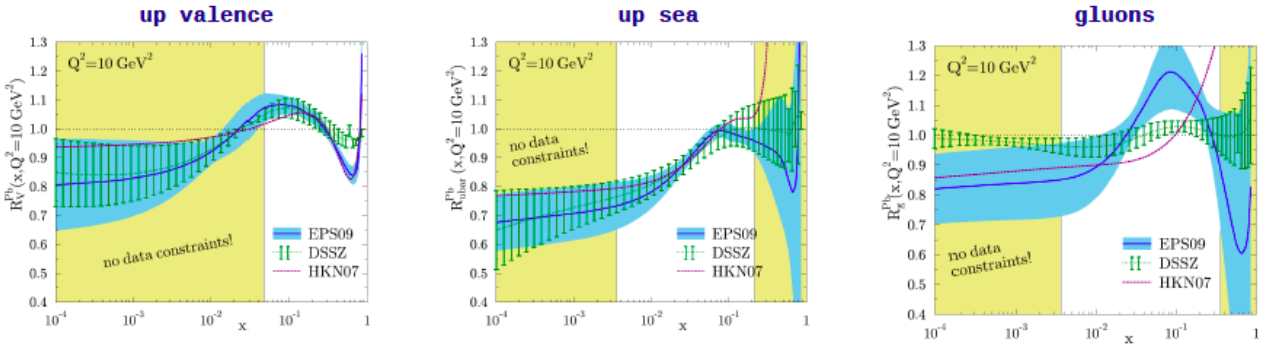

Figure 2-43: A summary of some of the most recent nPDFs. The central values and their uncertainties for up valence, sea and gluons are shown. The yellow bands indicate regions in x where the fits are not constrained by data.

Current measurements at RHIC strongly suggest that the suppression of single hadrons [84,85] and back-to-back di-hadron correlations [86] in d+Au collisions seen at forward rapidities at RHIC [87] can be interpreted as strong hints for the onset of saturation effects. This would go beyond the modification of nPDFs predicted by pQCD fits to the current world data. At this point, though, the interpretation that the onset of saturation effects has be seen, is not unique, for two main reasons.

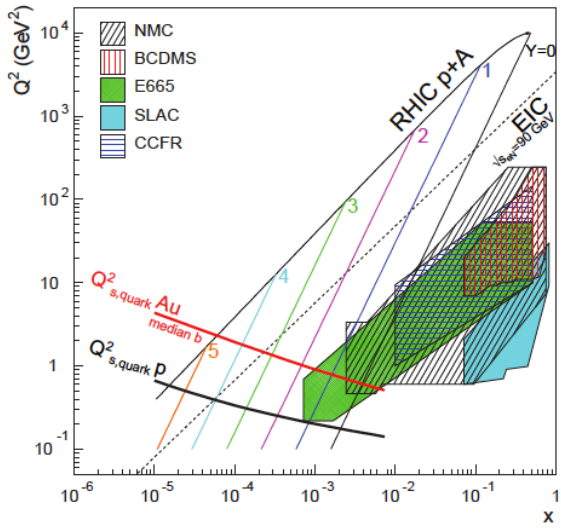

Figure 2-44: Kinematic coverage in the x-Q^2 plane for p+A collisions at RHIC, along with previous e+A measurements, the kinematic reach of an electron-ion collider (EIC), and estimates for the saturation scale Q_s in Au nuclei and protons. Lines are illustrative of the range in x and Q^2 covered with hadrons at various rapidities.

First, as shown in Figure 2-44, for the kinematic reach of RHIC energies the saturation scale is moderate, on the order of a few GeV^2, so measurements sensitive to the saturation scale are by necessity limited to semi-hard processes, and effects due to kinematic limits must be fully addressed.

Second, and more importantly, in measurements to date in d(p)+A collisions both the entrance and exit channels have components that interact strongly, leading to severe complications in the theoretical treatment. In d(p)+A collisions, these complications can be ameliorated by removing the strong interaction from the final state, using photons W$^{+/-}$, Z^0 and Drell-Yan electrons. Beyond this, the possibility of using polarized protons at RHIC to probe saturation phenomena is just beginning to be explored [88,89], utilizing the large transverse single-spin asymmetries seen in

p+p collisions at forward rapidity (which do not require a polarized ion beam) to explore the onset of saturation.

The polarized p+Au run in 2015 will be the first step to obtain data addressing the questions listed at the beginning of section 2.5. Due to its higher luminosity it will enable STAR to study more luminosity hungry processes. In the following a list of the key measurements for Run-15 are given, no scan in beam species is proposed to be done in 2015. However our understanding of the initial partonic structure of nuclei would greatly benefit for a scan in beam species in later years.

1. Di-hadron correlations are still the golden channel at RHIC to observe saturation. The away-side peak in the di-hadron correlations represents the back-to-back contribution to the coincidence signal as function of the azimuthal angle difference between the two hadrons in a p+A collision. It should disappear going from p+p to p(d)+Au if saturation sets in. A recorded luminosity of 300 nb^{-1} in Run-15 would give the unique opportunity to vary the trigger and associated particle p_T from low to high values and thus crossing the saturation boundary as shown in as shown in Figure 2-44 and reinstate the correlations for central p+A collisions for forward-forward π^0's. Single Transverse Spin Asymmetry in Polarized Proton-Nucleus Collisions: As a result of exciting recent theoretical developments, the scattering of a polarized proton on an unpolarized nuclear target appears to have the potential to extend and deepen our understanding of QCD. In the frame where the nucleus is relativistic, its wave function consists of densely packed quarks and gluons, which constantly split and merge with each other. At high enough energies the density of the gluons is so high that the saturation regime is reached, characterized by strong gluon fields and scattering cross sections close to the unitarity bound. The saturated wave function is often referred to as the Color Glass Condensate (CGC) and is reviewed in detail in [90]. The nuclear effects on A_N may shed important light on the strong interaction dynamics in nuclear collisions. While the theoretical approaches based on CGC physics predict that hadronic A_N should decrease with increasing size of the nuclear target [91,92,93], some approaches based on perturbative QCD factorization predict that A_N would stay approximately the same for all nuclear targets [94].

2. R_{pA} for direct photons in the rapidity range $3<\eta<4$:
   Direct photons are one of the key channels to separate strong interactions in the entrance and exit channels in d(p)+A collisions, because they have no strong interaction in the final state.

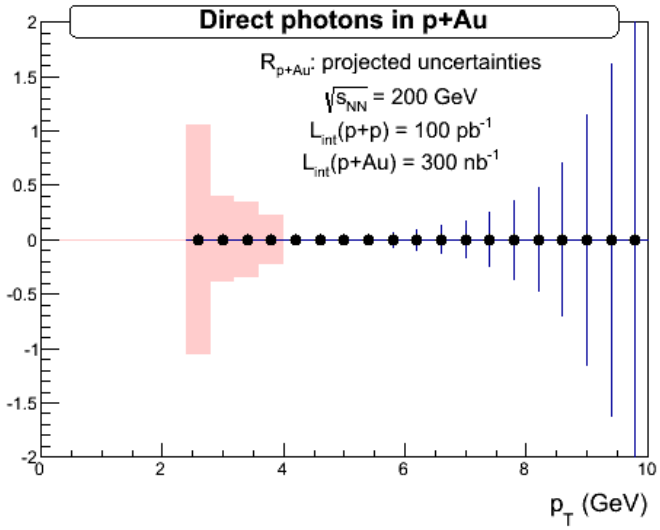

Figure 2-45: R_{pA} for direct photons measured with the FMS and its preshower in the rapidity range $3<\eta<4$. The assumed detector performance and cuts applied are the same as for Figure 2-16. The statistical uncertainties are based on recorded luminosities of 100 pb^{-1} for p+p and 300 nb^{-1} for p+Au. The systematic uncertainties are due to the remaining backgrounds (see Figure 2-16 (left)).

3. J/ψ-production in ultra-peripheral collisions (UPC) provides, like direct photon measurements, the opportunity if the J/ψ is detected through its leptonic channel to study only the effects of strong interactions in the initial state [95]. This measurement provides access to the spatial gluon distribution by measuring the distribution of $d\sigma/dt$. As follows from the optical analogy, the Fourier-transform of the square root of this distribution is the source distribution of the object probed. To study the gluon distribution in the gold nucleus, events need to be tagged were the photon is emitted from the proton. To study STARs capabilities for such a measurement events were generated with the Sartre event generator [96,97], an p+A (e+A) event generator specialized for diffractive exclusive vector meson production based on the bSat dipole model [98] and its linearization, the bNonSat model [99]. In Figure 2-46 (left) shows the probed x-Q^2 plane for events, where the "UPC-photon" is emitted by the proton-beam, p-shine. Figure 2-46 (middle) shows the rapidity distribution for the J/ψ-meson is shown for events the "UPC-photon" is emitted by the proton-beam and for events the photon is emitted by the Au-beam, Au-shine, after the following cuts have been applied to enhance the p-shine case:
   - no hit in the ZDC to veto the Au-breakup to ensure coherent scattering.
   - detecting the scattered proton in the RP ($-0.016 > -t > -0.2$ GeV^2)
   - both J/ψ decay leptons are in $-1 < \eta < 4$
   - cut on the p_T^2 of the scattered Au, calculated as the p_T^2 of the vector sum of the proton measured in the RP and the J/ψ to be larger then 0.02 GeV^2.

   The background from the Au-shine case has been suppressed basically completely. With an integrated delivered luminosity of 2.5 pb^{-1} ~7k J/ψ-mesons survive the cuts in the p-shine case. This statistics will allow measuring dσ/dt for coherently produced J/ψ-mesons. This distribution can be further used to obtain information about the gluon distribution in impact parameter space $g(x,Q^2,b)$ through a Fourier transform [100]. Doing this for different beam species will allow to pin down the A-dependence of nPDFs. For the 2015 p+A run due to the limited luminosity it will only be possible to measure the J/ψ-meson rapidity distribution.

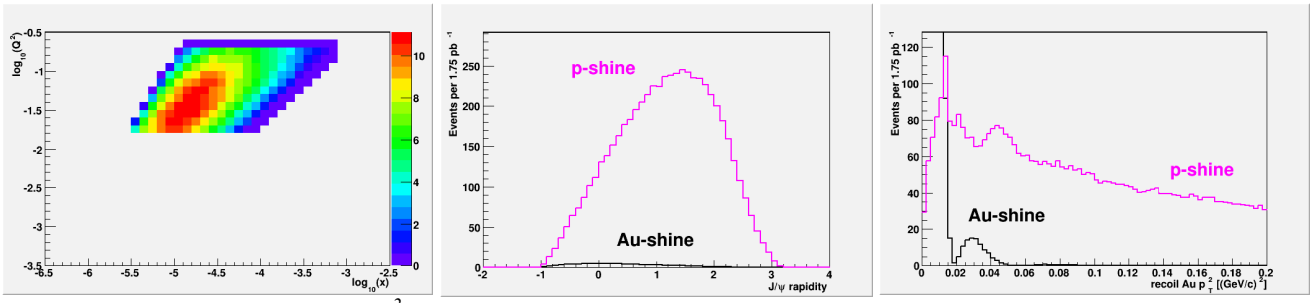

Figure 2-46: (left) The probed x-Q^2 plane for events for p-shine events. (middle) Rapidity distribution for the J/ψ-meson for p-shine and Au-shine events after applying all cuts listed. (right) p_T^2 of the scattered Au, calculated as the p_T^2 of the vector sum of the proton measured in the RP and the J/ψ.

4. Figure 2-47 clearly shows that the requested statistics in the 2015 transversely polarized p+p and p+Au Run, respectively, will be sufficient to measure the first transverse spin observables in pA. But a nuclear dependence must be measured in the p+A run at the end of the decade. Access to the generalized parton distribution E_g: The experimentally best way to constrain GPDs is through exclusive reactions in DIS, i.e., deeply virtual Compton scattering. RHIC with its possibility to collide transversely polarized protons with heavy nuclei has currently world-wide the unique opportunity to measure A_N for exclusive J/ψ in ultra-peripheral $p^{\uparrow}$+Au collisions [101]. A non-zero asymmetry would be the first signature of a non-zero GPD E for gluons, which is sensitive to spin-orbit correlations and is intimately connected with the orbital angular

momentum carried by partons in the nucleon and thus with the proton spin puzzle. A first measurement will be done in the 2015 transversely polarized p+A run with ~7k J/ψ's for a recorded luminosity of 300 nb^{-1}, which is enough to have a first look to the A_N as function of t. This measurement can be significantly improved with the high statistics p+A and p+p runs discussed in this document.

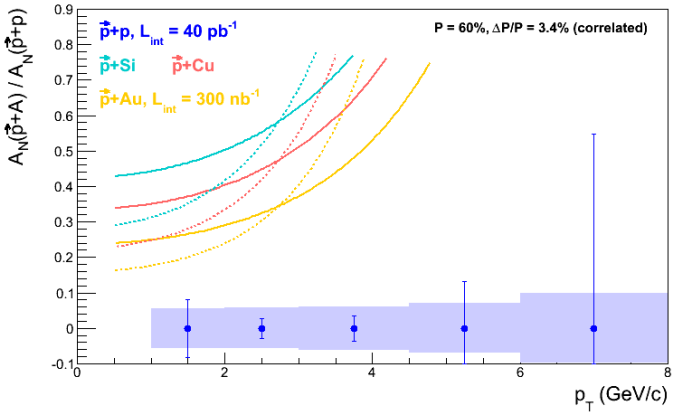

Figure 2-47: The projected statistical and systematic uncertainties for the ratio of A_N^{pA}/A_N^{pp} measured for π^0's in the STAR FMS for the requested transverse p+p and p+A running. The colored curves follow Eq. 17 in Ref. [51] assuming Q_s^p = 1 GeV (solid) and Q_s^p = 0.5 GeV (dotted) with $Q_s^A = A^{1/3} Q_s^p$.

As shown above hard probes in p+A(d+A) collisions at RHIC can provide us with very important constraints on the nPDFs, especially at scales where the DGLAP evolution is expected still to be applicable, i.e., at $Q > Q_s$. Given the kinematic constraints at RHIC, very forward hadron production measurements (low-x) are not well suited to study leading-twist shadowing since the Q^2 values are substantially too low. Typically nPDFs are calculated at most down to Q^2 ~1.69 GeV^2. Of special importance at RHIC will be measurements of correlated charm in p+A collisions at mid- or slightly forward rapidities or gamma-jet correlation measurements at forward rapidities (see section 0), which will help to pin down the nuclear gluon distributions, while Drell-Yan pairs are expected to set further constraints on the nuclear effects for the sea quark distributions. The Drell-Yan process, $q\bar{q} \to \gamma^* \to l^- l^+$, plays a special role among interactions with hadron beams. In contrast to hadronic final states, in Drell-Yan scattering the values of x_1, x_2, and $Q^2(=M^2)$ can be reconstructed on an event-by-event basis. In addition, factorization has been proven, rather than just assumed, for Drell-Yan di-lepton production. As such, for many years Drell-Yan cross sections have played a key role to constrain sea quark distributions in nucleon and nuclear PDF fits. (For example, see the discussions in [102,103].)

When measured in the forward direction, Drell-Yan di-lepton production in p+A collisions at RHIC can provide access to sea quark distributions in the nucleus at $x < 0.001$ (for details see Figure 2-48). This is nearly an order of magnitude lower x than the current nuclear DIS data, and over an order of magnitude lower x than the Drell-Yan data that form the primary inputs for EPS09. Furthermore, measurements of the Drell-Yan nuclear dependence at RHIC can also provide significant constraints on the nuclear gluon distribution at very low x via evolution [102]. As such, Drell-Yan measurements at RHIC will provide essentially model-independent information about the nuclear modifications of the gluon distribution well into the x regime where the π^0-π^0 correlation measurements indicate gluon saturation may be important. It is noted that forward J/ψ production will be measured concurrently with Drell-Yan scattering. J/ψ production in these kinematics is dominated by gg fusion, so this will provide complementary information about the gluon density at very low x.

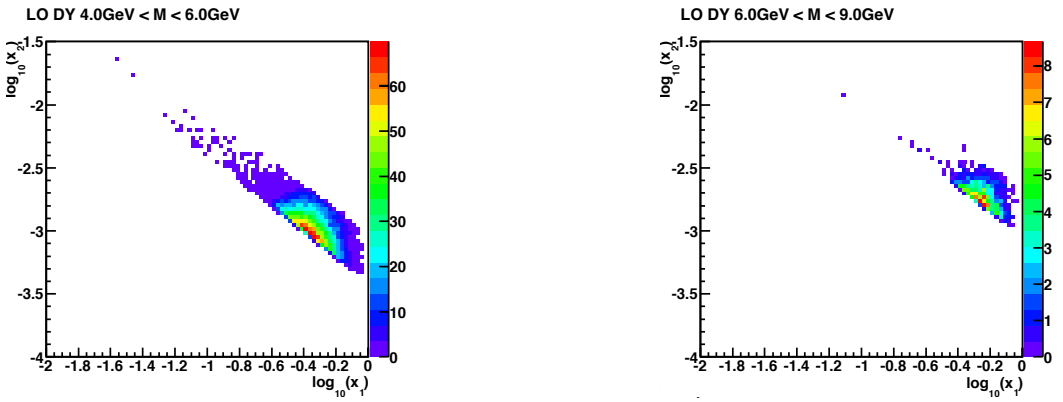

Figure 2-48: The x_1-x_2 distribution for DY production for 2 bins of the lepton pair mass at $\sqrt{s}$ =200 GeV with the leptons being in the rapidity range $2.5 < \eta < 4.0$.

DY measurement capability with forward tracking and forward calorimeter systems

The biggest challenge of DY measurements is to suppress the overwhelming hadronic background. The total DY cross-section is on the order of $10^{-5} \sim 10^{-6}$ of the hadron production cross-sections, therefore the probability of mis-identifying a hadron track as e^+/e^- has to be suppressed down to the order of 0.1% while maintaining reasonable electron detection efficiencies. To that end we have studied the combined electron/hadron discriminating power of the proposed forward tracking and calorimeter systems. We found that by applying multivariate analysis techniques to the features of EM/hadronic shower development and momentum measurements we can achieve hadron rejection powers of 200 to 2000 for hadrons of 15 GeV to 50 GeV with 80% electron detection efficiency. The hadron rejection power has been parameterized as a function of hadron energy and pseudo-rapidity and has been used in a fast simulation to estimate DY signal-to-background ratios. In the subsection we will describe the procedures of our simulation and discuss some of the results.

We have implemented the exact geometry of the proposed forward calorimeter system in section 2.1 into the STAR simulation framework. With both the EM and hadronic sections as well as the high-granularity of the EMCal we will be able to measure the shower development in both longitudinal and transverse directions. We have simulated the response of the FCS to single electrons and π^-. To discriminate EM shower against hadronic shower we have used three observables:

1. **Eratio:**
   the ratio of a 5x5 EMCal cluster energy to the sum of the energies of the same 5x5 EMCal cluster and the projected 5x5 HCal cluster.
2. **Swidth:**
   the effective EMCal shower width defined as $R_p = \sum_i r_i E_i^{0.4} / \sum_i E_i^{0.4}$ where r_i is the distance of the ith tower to the centroid of a 5x5 EMCal cluster, E_i is the energy of that tower. The summation is over the 25 towers in the 5x5 EMCal cluster around the highest tower.
3. **NTratio:**
   the number of EM towers with energies above 100MeV divided by the total number of EMCal and HCal towers above the same threshold. All the towers come from a pre-defined 5x5 EMCal cluster around the highest tower and the corresponding 5x5 HCal cluster.

Figure 2-49 shows the distribution of these three variables for 30 GeV electrons and π^- respectively.

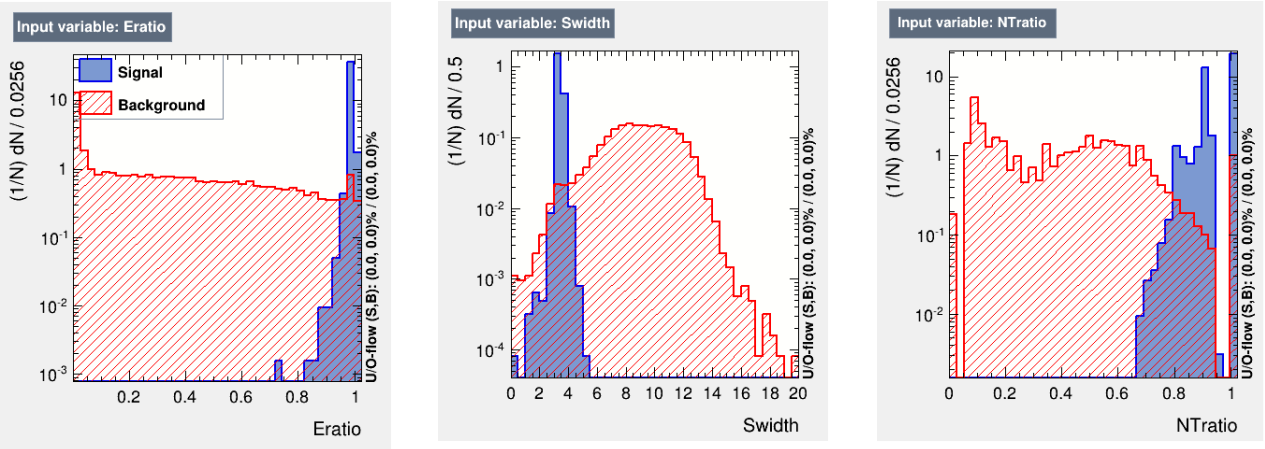

Figure 2-49: Eratio, Swidth & NTratio distribution for 30 GeV electrons (Signal) and π^-(Background). See text for explanation.

The FTS helps rejecting hadrons by measuring total track momentum. The ratio of energy deposit in EMCal to track momentum (E/P ratio) could serve as an additional information in separating $e^{+/-}$ from charged hadrons. The momentum resolution was evaluated from a standalone simulation of the forward tracking system with typical expected performance for the technology choice and parameterized as a function of energy and pseudo-rapidity. Figure 2-50 shows the parameterized momentum resolution at $\eta = 2.5$ and 4.0. Figure 2-51 shows the E/P ratio for 30 GeV electrons and π^-.

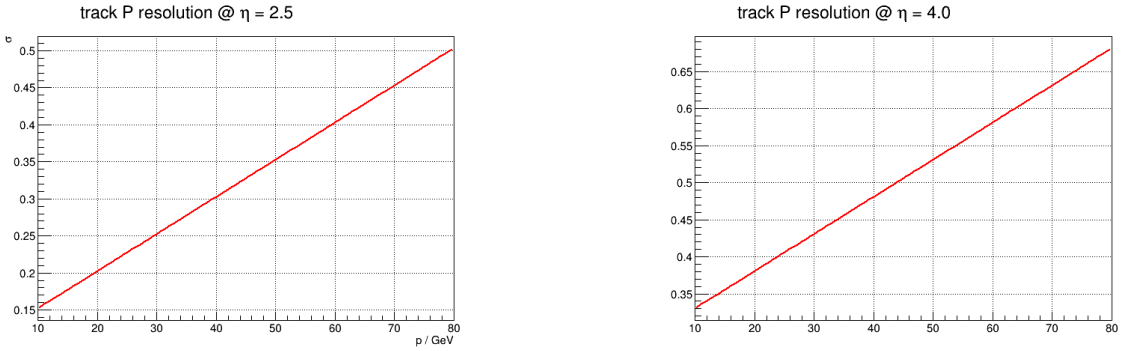

Figure 2-50: expected track momentum resolution of the forward tracking system from simulations.

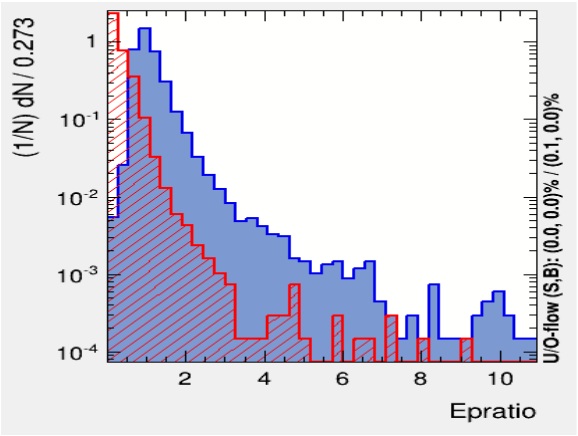

Figure 2-51: E/P ratio of 30 GeV electrons (blue) and π^- (red)

These observables from the FTS and FCS have been used as inputs to a Boosted Decision Trees (BDT) algorithm. The BDT contains 1000 binary decision trees each has a depth of 4 and corresponds to a particular partition of the 4-dimensional feature space into signal(electron) and background(hadron) regions. They're trained sequentially using half of the electron/ π^- samples generated. Mis-identified tracks from the previous decision trees were given a higher weight in training the subsequent trees. In the end each decision tree was given an index representing its performance during the training. In the validation stage the decision of each track identification was made based on the collective response of all of the decision trees, with each of their responses weighted by the performance index. The boosting algorithm takes advantage of using not only the discriminating power of each single observable but also the correlations among them.

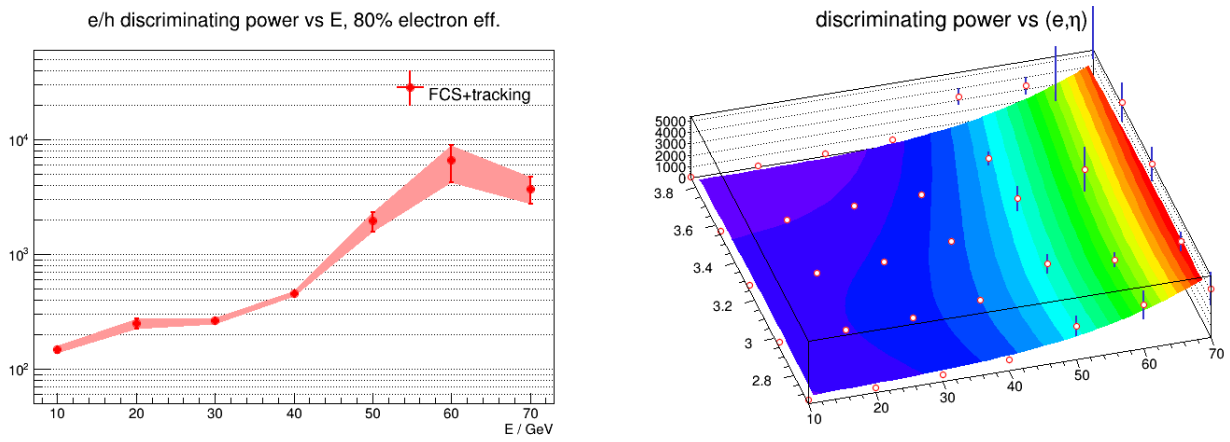

Figure 2-52: e/h discriminating power as a function of the track energy (left panel) and the variation over the pseudo-rapidity (right panel) from combined forward tracking and calorimeter systems

To estimate the DY signal to background ratio the e/h discriminating power has been parameterized as a function of the track energy and the pseudo-rapidity as shown on in Figure 2-52. We have generated 4 billion PYTHIA pp events at 200 GeV with *CKIN(3)* = 3 GeV and a forward filter requiring a total p_T> 3 GeV in any of the four jet-patch-like regions in 2.5 < η < 4.0. All basic QCD 2→2 scatterings as well as heavy flavor channels were enabled. As a reference we note that 2.5 pb^{-1} p+Au luminosity is equivalent to 500 pb^{-1} p+p luminosity, which corresponds to 240.5 billion p+p events with the above setting. The DY productions through $q\bar{q}$ annihilation and qg scattering processes were separately generated and scaled to 500 pb^{-1}.

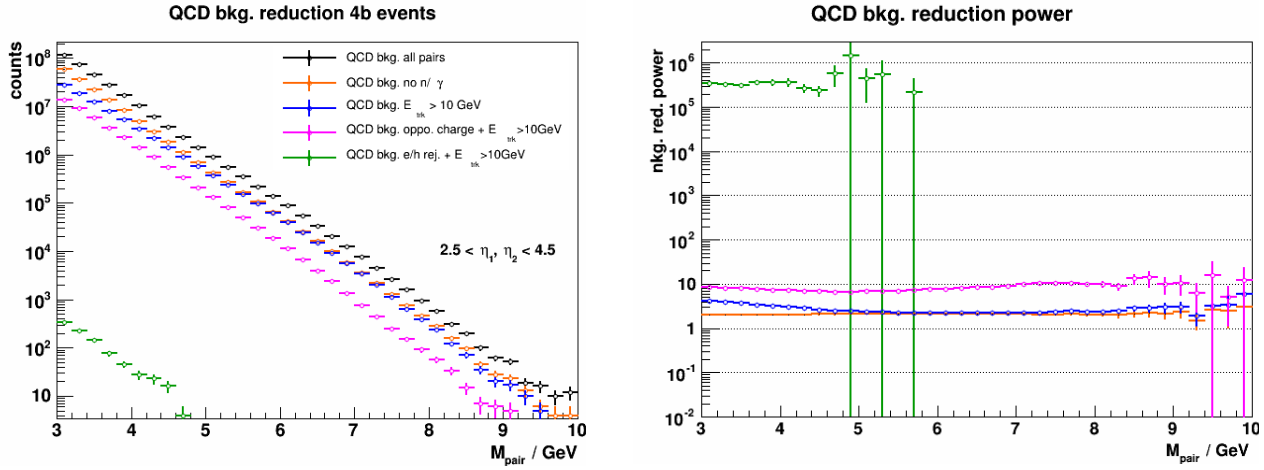

Figure 2-53: QCD background reduction with kinematics cuts and e/h rejections

Figure 2-53 (left panel) shows the yield of track pairs from QCD background sample with the proposed cuts applied accumulatively to illustrate the background reduction process from each step. The final background yields from the 4 billion sample after gamma/neutron removal + track energy cuts + charge sign requirement and e/h discrimination are shown by the green points. The right panel of Figure 2-53 shows the accumulative background reduction factor after each step of applying the cuts.

The final background yields as a function of pair masses were then fit by an exponential function and rescaled to a total luminosity of 500 pb^{-1}. The left panel of Figure 2-54 shows the normalized background yield along with the expected DY productions. The green band represents the statistical uncertainties of the background yield and its shape. The right panel shows the DY signal to the QCD background ratio as a function of pair masses.

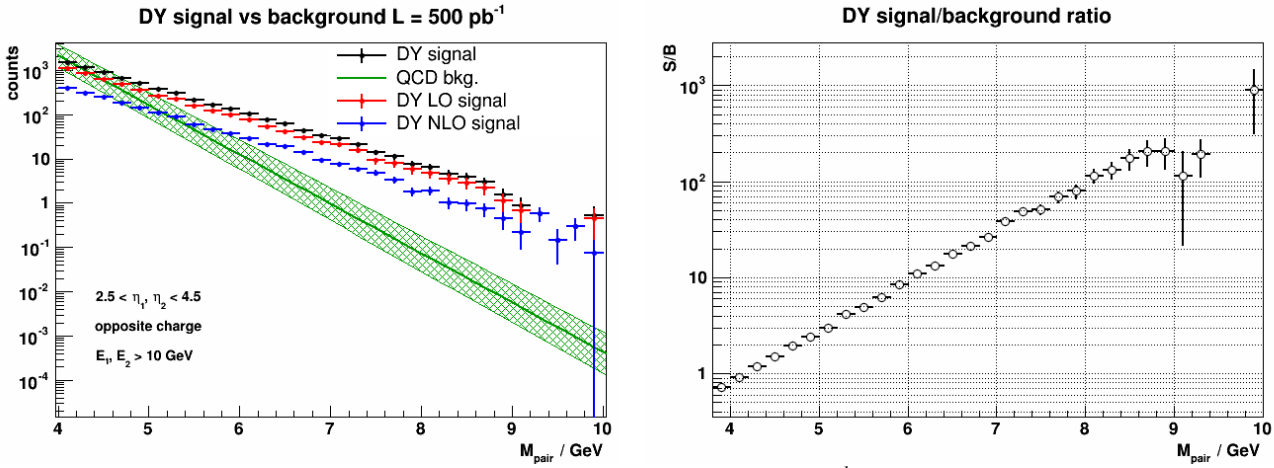

Figure 2-54: DY signal and background yield from 500 pb^{-1} pp200 GeV collisions

Finally we note that we have only considered the QCD background in the DY signal/background ratio presented in this subsection. We expected additional backgrounds from photon conversion from materials. Without a detailed design of the beam pipe and the FTS and its supporting structure, we do not have a reliable GEANT model to simulate the photon conversion background yet. Rough estimate indicated that these additional backgrounds may be on the same order for the QCD background if care is taken to minimize the materials in the fiducial acceptance of the forward detectors. We conclude that the DY measurement for p+A collisions at 200 GeV with the STAR forward instrumentation upgrade is very promising and will be pursued vigorously as we prepare for a proposal and technical design report of the upgrade.

Direct Photon plus Jet

The analysis of the angular dependence of two-particle correlations in hadronic collisions has proven to be an essential tool for testing the underlying QCD dynamics [104]. In forward-forward correlations facing the $p(d)$ beam direction one selects a large-x parton in the p(d) interacting with a low-x parton in the nucleus. For $x < 0.01$ the low-x parton will be back-scattered in the direction of the large-x parton. Due to the abundance of gluons at small x, the backwards-scattered partons are dominantly gluons, while the large-x partons from the p(d) are dominantly quarks.

Direct photon plus jet (direct γ+jet) events, dominantly produced through the gluon compton scattering process, $g+q \rightarrow \gamma+q$, are sensitive to the gluon densities of the nucleon and nuclei in p+p and p+A collisions. Through measurements of the longitudinal double spin asymmetry in polarized

p+p collisions and azimuthal correlations in p+A collisions for direct γ+jet production, one can study the gluon helicity density and gluon saturation phenomena at small-x. Unlike di-jet production that is governed by both the Weizsäcker-Williams and dipole gluon densities, direct γ+jet production only accesses the dipole gluon density, which is better understood theoretically [105]. On the other hand, direct γ+jet production is experimentally more challenging due to small cross section and large background contribution from di-jet events in which photons from fragmentation or hadron decay could be misidentified as direct photons. We have studied the feasibility to perform direct γ+jet measurements with the upgraded STAR detector in polarized p+p collisions at $\sqrt{s}$=500 GeV and unpolarized p+p and p+Au collisions at $\sqrt{s_{NN}}$=200 GeV. PYTHIA-8.189 [106] is used to produce direct γ+jet and di-jet events. In order to suppress di-jet background, the leading photon and jet are required to be balanced in transverse momentum, $|\phi^{\gamma} - \phi^{jet}| > 2\pi/3$ and $0.5 < p_T^{\gamma}/p_T^{jet} < 2$. Both the photon and jet have to be in the forward acceptance $2.8 < \eta < 3.7$ with $p_T > 4.5$ (3.2) GeV/c in 500 (200) GeV p+p collisions. The photon needs to be isolated from other particle activities by requiring the fraction of electromagnetic energy deposition in the cone of ΔR=0.1 around the photon is more than 95% of that in the cone of ΔR=0.5. Jets are reconstructed by an anti-k_T algorithm with ΔR=0.5. After applying these selection cuts, the signal-to-background ratio is around 3:1 [107]. The expected number of selected direct γ+jet events is around 1.2 million with 500 pb^{-1} delivered luminosity in polarized p+p collisions at $\sqrt{s}$=500 GeV. Such a measurement would constrain the gluon helicity density in 0.0003<x<0.003 (see Figure 2-55). The expected number of selected direct γ+jet events is around 100k with 500 pb^{-1} (2.5pb^{-1}) delivered luminosity in p+p (p+Au) collisions at $\sqrt{s_{NN}}$=200 GeV. We conclude that a measurement of direct photon-hadron correlation from p+A collisions is feasible, which is sensitive to the gluon density in 0.001<x<0.005 in the Au nucleus (see Figure 2-55) where parton saturation is expected.

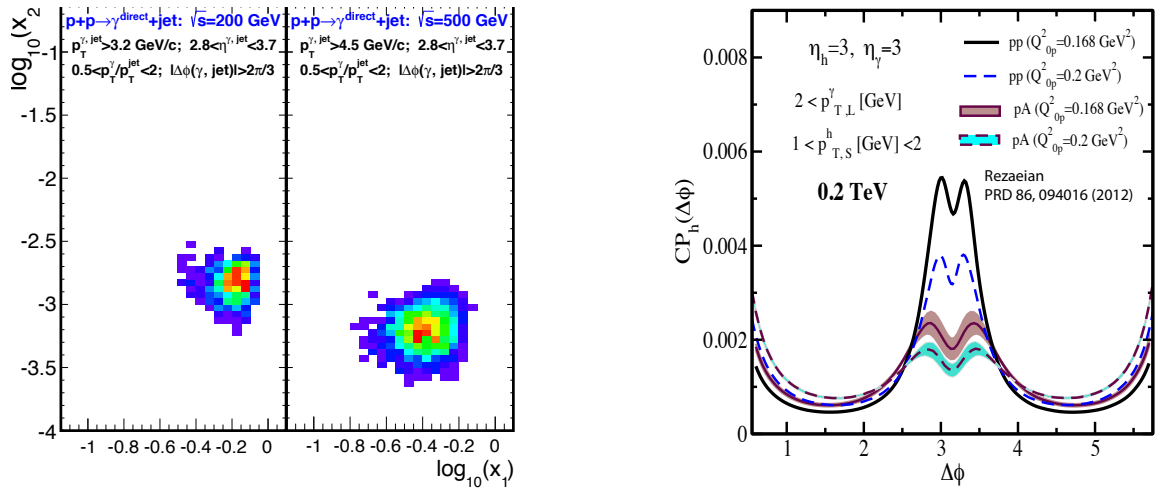

Figure 2-55: Left: Bjorken-x distributions of hard scattering partons in direct γ+jet production after event selections described in the text in p+p collisions at $\sqrt{s}$=200 and 500 GeV, respectively. Right: γ-hadron azimuthal correlation in minimum bias p+p and p+Au collisions at $\sqrt{s_{NN}}$=200 GeV. The curves are obtained with two different initial saturation scale of proton Q^2_{0p}=0.168 and 0.2 GeV^2 and the corresponding initial saturation scale in the nucleus within Q^2_{0A}~3-4Q^2_{0p} (c.f. [105]).

Energy Loss in Cold Nuclear Matter

One of primary observables for measuring cold nuclear matter effects is the production of J/ψ in p+A collisions. Since J/ψ are produced in hard collisions, their yields are expected to scale as the nuclear thickness function T_{AB}, for collision species A and B, in the absence of nuclear

modifications. In p+A collisions, the observed yields can be affected by both modifications to the parton distribution functions (an initial-state effect), which can also include saturation effects at large enough gluon densities, as well as energy loss in the cold nuclear medium (a final-state effect) [108]. At mid to forward rapidity, both of these effects result in a suppression of the T_{pA}-scaled yields. At very forward rapidity, the energy loss mechanism is expected to become dominant, making it easier to differentiate between the two effects. Figure 2-56 shows the predicted effect of CNM energy loss on the R_{pA} of J/ψ as a function of rapidity [108, 109], where R_{pA} is the ratio of the T_{pA}-scaled particle yields in p+A collisions to the cross section measured in p+p collisions.

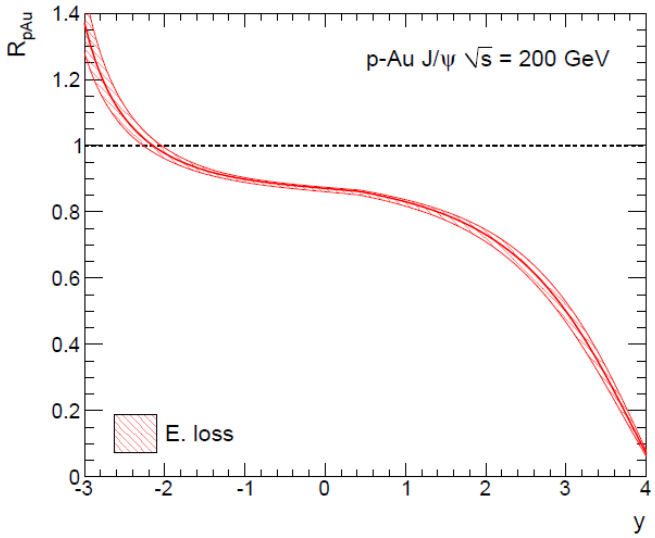

Figure 2-56: Predicted R_{pA} for J/ψ at $\sqrt{(s_{NN})}$=200 GeV as a function of rapidity [108, 109].

PHENIX has measured R_{dAu} for J/ψ at backward to forward rapidity, but the measurement does not extend up to y>+3, where the suppression is predicted to be largest. Figure 2-57 (left) shows the PHENIX publication of this measurement in d+Au collisions [110] in the range $-2.2<y<2.2$. The theoretical calculation [104], including both energy loss and modified PDF's, agrees with the data well. At these rapidities, the effect of energy loss is not as strong as at more forward rapidity. The models are able to describe the current data with and without saturation effects and with different values of "q-hat" varying the parton energy loss. More forward measurements have been performed at the LHC, by both the LHCb experiment [111] and the ALICE experiment [112] at a higher collision energy of $\sqrt{s_{NN}}$=5 TeV. Figure 2-57 (right) shows the result from the LHCb experiment compared to theoretical calculations. The J/ψ is measured for $p_T<14$ GeV/c (with mean p_T between 2.5 and 3.0 GeV/c). For this measurement at the LHC collision energy, the models including only initial-state effects are not so distinguishable from those containing effects from final-state effects. The measurement for $1.5<y<4.0$ is consistent with LO EPS09 and nDSg [113] (two different parameterizations of the nuclear-modified gluon distribution functions) calculations, NLO EPS09 [114], as well as those calculations including both initial-state effects and final-state energy loss (curves labeled "E. loss") [108].

The result from ALICE [112] is in a similar kinematic range and is consistent with the LHCb result. The same calculation shown for RHIC collision energy in Figure 2-56 [108] is also in Figure 2-57 (right) for LHC collision energy. In this calculation, the suppression is predicted to be larger at forward rapidity at RHIC.

With the planned forward upgrades, STAR will be able to measure J/ψ for $2.5<y<4.0$ through the mass reconstruction of electron-positron pairs. Tracking in the FTS together with the calorimetry of the planned FCS will provide good electron/positron candidates for the invariant

mass calculation. The Pre-Shower in the FCS will provide further rejection of photons as well as hadrons.

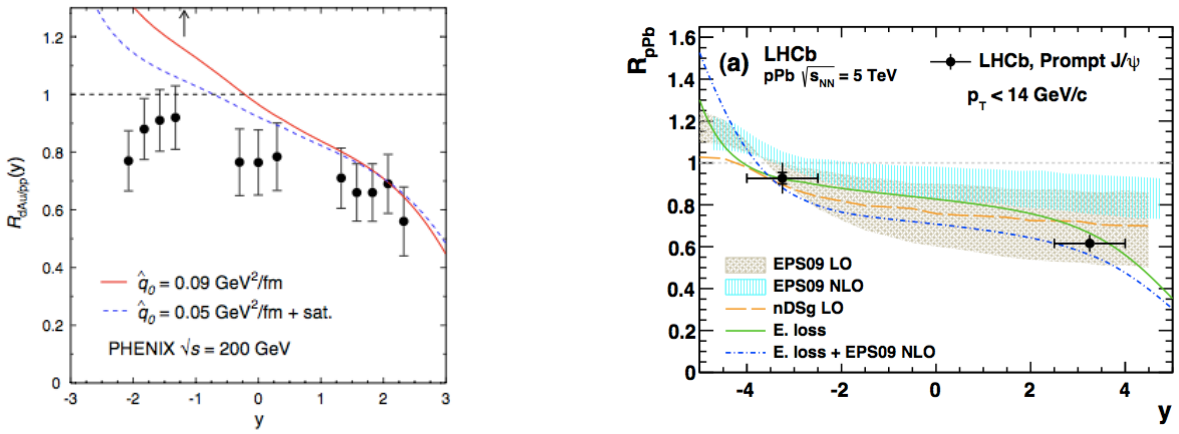

Figure 2-57: (Left) PHENIX measurement of CNM effects of J/ψ production in d+Au collisions relative to p+p collisions for −2.2<y<2.2 at $\sqrt{(s_{NN})}$=200 GeV [110] compared to a theoretical calculation [108]. (Right) LHCb measurement of J/ψ production in p+Pb collisions relative to p+p collisions for 1.5<y<4.0 and −5.0<y<−2.5 at $\sqrt{(s_{NN})}$=5 TeV [111] compared with theoretical calculations [108, 113, 114].

Calculations of the J/ψ cross section as a function of rapidity predict $Bd\sigma/dy$~7 nb at y=3 (where B is the branching fraction of J/ψ to electron-positron pairs) in p+p collisions at RHIC, with a nearly linear decrease in the range of y=2.5 to 3.5 [112]. This calculation describes the PHENIX measurement of J/ψ in p+p collisions for −2.2<y<2.2 [113] well. We therefore assume an approximate cross section of 7 nb in our forward acceptance window times the suppression factor of 0.4 (from the predicted R_{pA} at y=3 shown in Figure 2-56), giving us a cross section of 2.8 nb. With a pp-equivalent luminosity of 500 pb^{-1}, we can expect 1.4 million J/ψ produced in our forward acceptance window. This number is further reduced due to the decay opening angle, by momentum cuts on the electron/positron candidates (p > 10 GeV/c), and by the electron/positron detection efficiency of approximately 0.8, as estimated in the above section on Drell-Yan production. The final expected numbers as a function of J/ψ p_T are shown in Figure 2-58 (left).

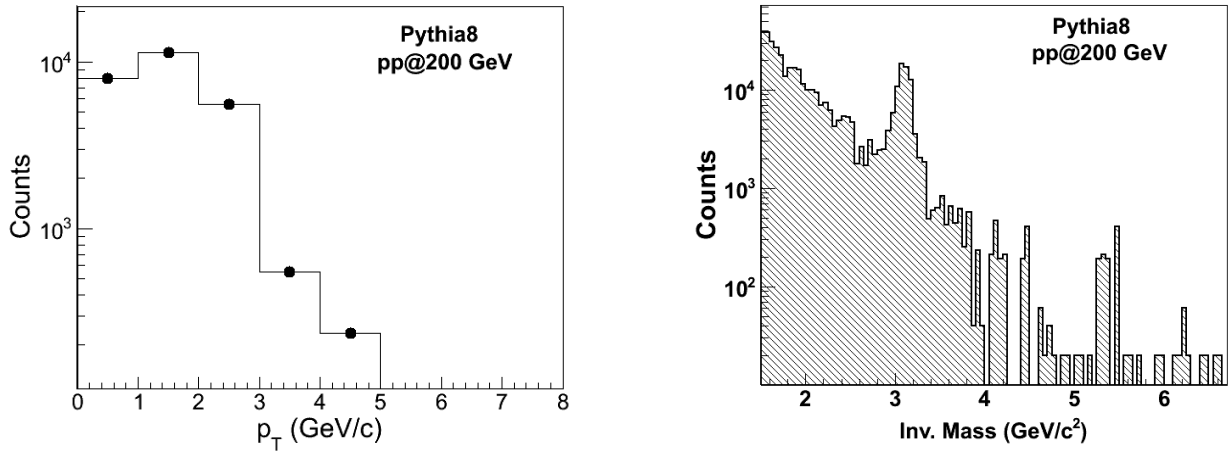

Figure 2-58: Simulation result of (left) J/ψ dN/dp$_T$ distribution, showing the expected number of reconstructed J/ψ in the forward acceptance and (right) invariant mass distribution (log scale) of J/ψ within estimated hadronic background.

Also shown in Figure 2-58 (right) is a simulation of the invariant mass of J/ψ scaled by its relative

cross section and superimposed onto the invariant mass reconstructed from charged-particle background. The rejection factors of hadrons are again taken from estimates made in the previous section on Drell-Yan production and applied to the PYTHIA simulation. The J/ψ signal is generated from PYTHIA events, with the setting that produces a J/ψ in each event, and is scaled to the expected number as calculated in the above paragraph. The hadronic background is generated with PYTHIA events without the setting that produces a J/ψ, and is scaled to the expected number of p+p-equivalent events. The energies are smeared from a parameterization of the expected energy response of the FCS.

3 STAR Upgrades

3.1 Forward Calorimeter System

The STAR forward upgrade is mainly driven to explore QCD physics in the very high or low region of Bjorken *x*. Previous STAR efforts using the FPD and FMS detectors, in particular, the refurbished FMS with pre-shower detector upgrade in Runs 2015-2016, have demonstrated that there are outstanding QCD physics opportunities in the forward region as we have outlined in the previous sections. In order to go much beyond what STAR would achieve with the improved FMS detector, STAR proposes a forward detector upgrade with superior detection capability for neutral pions, photons, electrons, jets and leading hadrons covering a pseudo-rapidity region of 2.5-4.5.

At the core of the forward detector upgrade is the Forward Calorimeter System (FCS). The design of the FCS is driven mainly by detector performance, the integration into the STAR system and the cost optimization. Whenever possible we also minimize the number of mechanical components and the construction and operation resources needed from the collaboration in order to carry out the forward upgrade project under the expected constraints for budget and other resources.

The FCS consists of a Spaghetti ElectroMagnetic Calorimeter (SPACal) followed by a Lead and Scintillating Plate sampling Hadronic Calorimeter (HCal). The SPACal is made of Tungsten powder and scintillating fibers as such it has achieved one of the highest densities and among the most compact calorimeters. The Moliere radius of the SPACal is about 2.3 cm and we have chosen the size of each module to be 2.5×2.5×17 cm^3 corresponding to 23 X_0 in length. The HCal is made of Lead and Scintillator tiles with a tower size of 10×10×81 cm^3 corresponding to 4 interaction length. Our goal is to have a fully compensated calorimeter system. The proposed FCS has 120×80 SPACal towers and 30×20 HCal towers covering an area of 3×2 m^2. We are currently investigating the possibility to locate the FCS closer to the interaction vertex reducing the number of towers necessary for the same pseudo-rapidity coverage.

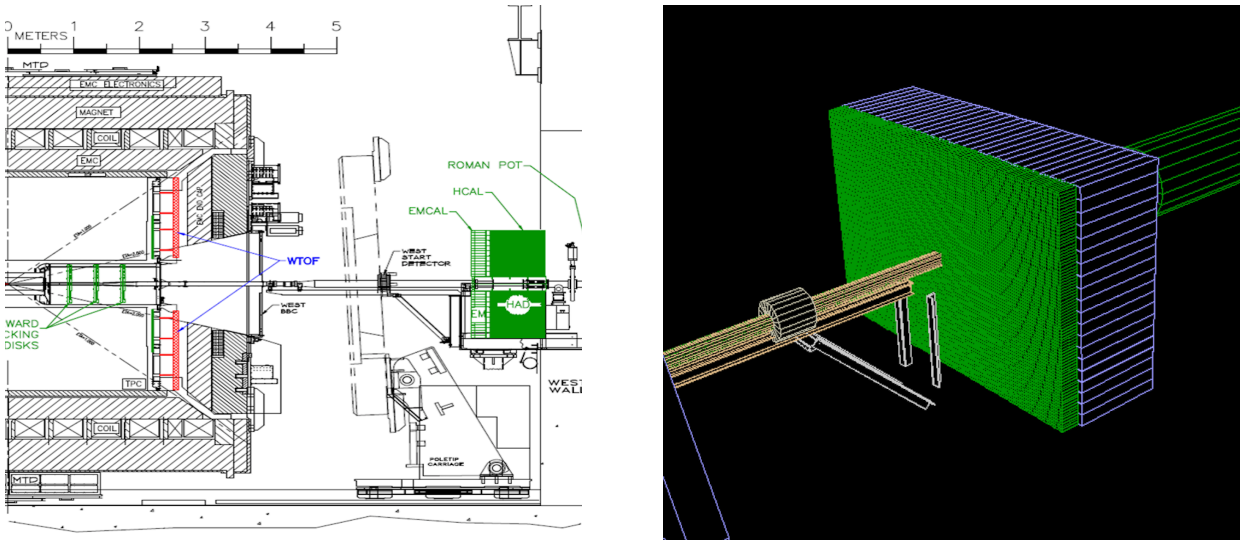

Figure 3-1: Location of the FCS at the West side of the STAR Detector system and a GEANT model of the FCS in the STAR simulation software

Figure 3-1 shows the location of the proposed FCS at the West side of the STAR detector system and a schematic description of the FCS in the STAR Monte Carlo simulation software. The read-out for the SPACal will be placed in the front so that there will be no significant dead gaps

between the SPACal and the HCal. Wave-length shifting slats are used to collect light from the HCAL scintillating plates to be detected by photon sensors at the end of the HCal. Multiple Silicon PMTs will be used to read out each SPACal and HCal module, 4 for SPACal and 8 for HCal, respectively.

The SPACal construction technique using Tungsten powders and scintillating fibers and the compact read-out scheme using SiPMTs have been the subject of a detector R&D project by a team of STAR groups from UCLA, TAMU, PSU, IU and BNL under the support of the BNL/JLab EIC generic detector R&D program. In 2012 we constructed several prototype SPACal modules and carried out a beam test at FNAL to prove the validity of the basic concept for the Tungsten powder and scintillating fiber construction technique. In 2013-2014 with additional support from STAR for the calorimeter R&D, we refined the SPACal construction technology and built wedge-shaped SPACal modules for EIC barrel applications and normal SPACal modules for STAR FCS applictions. We also developed a novel construction technique for HCal by stacking Lead and Scintillator plate in-situ. Students and post-docs just before the test run constructed an array of 4×4 prototype HCal modules at the FNAL test beam site. We envision that a full HCal detector can be assembled at the STAR experimental hall within a few months during the summer shutdown period.

Figure 3-2 shows a newly constructed array of 4×4 HCal modules at the FNAL test beam facility. The right panel shows the energy resolutions for the FCS SPACal and HCal detectors as a function of the beam energy. SiPMTs were used for the read-out of both calorimeter detectors. The measured energy resolution as a function of beam energy is consistent with our Monte Carlo simulations for the detector performance. The measured values have been used in our physics simulations for the proposed forward detector upgrade. We have established a viable detector construction technology and proved the feasibility of SiPMT read-out scheme for the proposed STAR FCS. The performance of the prototype FCS testing at FNAL in March 2014 demonstrated that the proposed FCS detector will meet the STAR physics requirements.

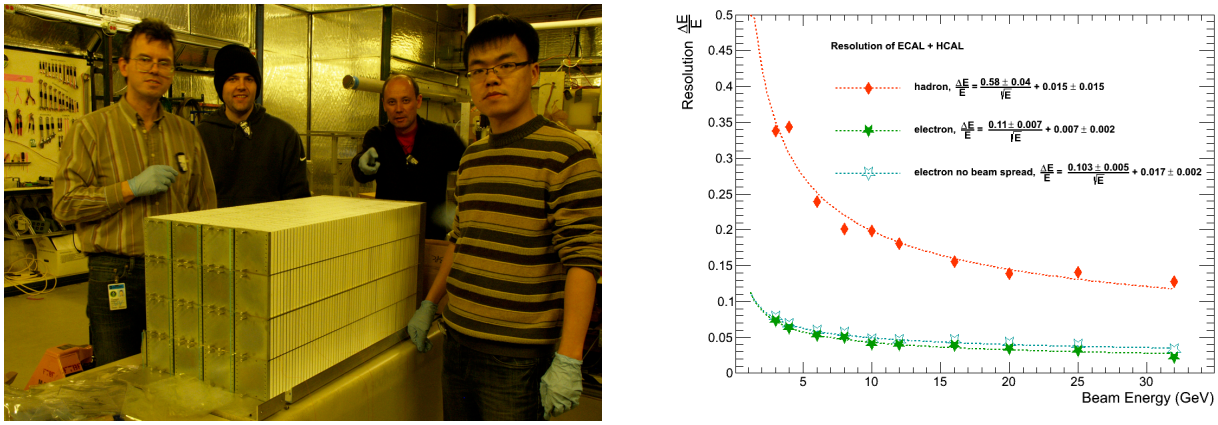

Figure 3-2: Prototype of HCAL calorimeter being assembled at FNAL for the test run. Energy resolution of the FCS for electrons and hadrons measured at test run at FNAL in 2014

3.2 Forward Tracking System

In addition to the FCS, a Forward Tracking System (FTS) is also under consideration for the STAR forward upgrade project. Such a FTS has to cope with the STAR 0.5 T Solenoid magnet field to discriminate charge sign for transverse asymmetry studies and those of electrons and positrons for Drell-Yan measurements. It needs to find primary vertices for tracks and point them towards the calorimeters in order to suppress pile-up events in the anticipated high luminosity collisions, or to

select particles from Lambda decays. It should also help with electron and photon identification by providing momentum and track veto information. In order to keep multiple scattering and photon conversion background under control, the material budget of the FTS has to be small. These requirements present a major challenge for detector design in terms of position resolution, fast readout, high efficiency and low material budget.

STAR has considered two possible detector technology choices: the Silicon detector technology and Gas Electron Multiplier (GEM) technology. STAR has gained considerable experience in both technologies from the FGT (Forward GEM Tracker) construction and the Intermediate Silicon Tracker (IST) construction in recent years. Several groups are pursuing GEM-based detector R&D under the auspices of generic EIC R&D program. Further evaluation of the GEM tracker option based on the STAR FGT experience will be needed if STAR will pursue such a technology.

Silicon detectors have been widely used in high-energy experiments for tracking in the forward direction. For example, Silicon strip detectors have been successfully used at many experiments: the Dzero experiment at the Tevatron, CMS and LHCb at the LHC, and PHENIX at the RHIC. More recent designs incorporate hybrid Silicon pixel detectors, which resulted in the improvement of position resolutions and removal of ghost hits, but unfortunately they also significantly increased the cost and material budget. According to preliminary Monte Carlo simulations, charge sign discrimination power and momentum resolution for the FTS in the STAR Solenoid magnet depends mostly on phi resolution, and is insensitive to the r-position resolution. Therefore a Silicon mini-strip detector design would be more appropriate than a pixel design. We are evaluating a design that consists of three to four disks at z locations at about 70 to 140 cm. Each disk has wedges covering the full 2π range in ϕ and 2.5-4 in η. The wedge will use Silicon mini-strip sensors read out from the larger radius of the sensors. Compared to the configuration of reading out from the edges along the radial direction, the material budget in the detector acceptance will be smaller since the frontend readout chips, power and signal buses and cooling lines can be placed outside of the detector acceptance.

STAR will continue to evaluate these technology options for the FTS design. More R&D efforts are needed to demonstrate the technical feasibility of these options through Monte Carlo simulations and detector prototyping. We hope to narrow the choice when we develop the technical proposal for the STAR forward upgrade in the coming a few years.

3.3 Cost and Schedule

The p+p and p+A physics program forms an integral part of the STAR multi-year physics program depicted in Figure 3-3.

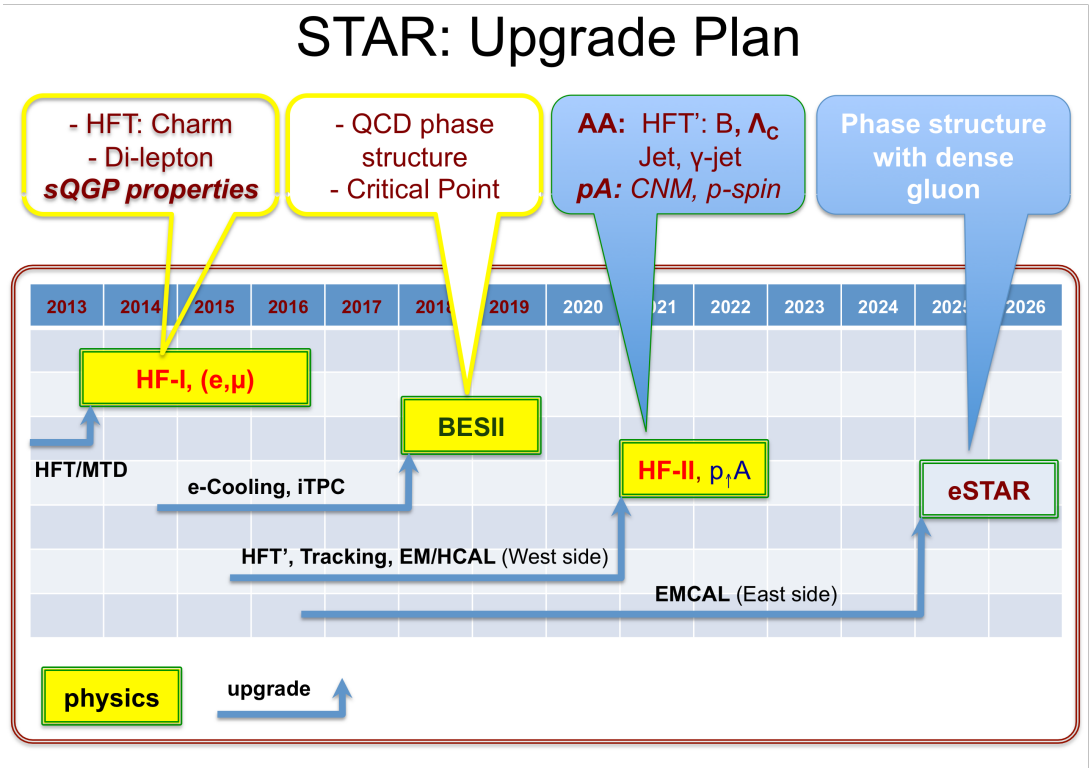

Figure 3-3: STAR's future physics programs: 2014-16, studying sQGP properties with heavy flavor and di-leptons; 2018-19, RHIC beam energy scan, narrowing in on the region of $\sqrt{s_{NN}} \leq 20$ GeV; 2021-22, (a) sQGP properties with the upgraded faster Heavy Flavor Tracker, specifically for the measurements of bottom and Λ_C, and (b) polarized p+p / p+A program as described in this document; 2025 and beyond, starting of the e+p and e+A program.

Research and Development projects are the first steps toward realizing a cutting-edge detector. Both detector components proposed in this document have an associated and active R&D effort. The FCS project has benefited, and is benefiting, from the generic detector R&D program organized by BNL in association with JLab and DOE to address the scientific requirements for measurements at a future EIC. The STAR collaboration is still in the process of optimizing the FCS and FTS configurations for the different physics goals. The plan is to develop a proposal and a Technical Design Report in the coming years. We envision that constructions may commence in 2018 and to have the detectors ready for physics data taking in 2020. The technology for the FCS has been demonstrated through beam tests of a full-scale prototype (see section 3.1). The technology choice for the FTS on the other hand is still under evaluation. Preliminary cost estimates based on the FCS design and a comparable project similar to the FTS amount to approximately $19.5M (FY12) including contingencies. The project costs and the funding profile are based on the following:

- The FCS project has a three-year construction period preceded by a 1-2 year design, engineering, and prototype phase in a technically driven schedule. It will initially serve measurements at forward rapidity in p+p, p+A, and A+A in the later part of the decade. The labor costs are $1.9M in this case and detector materials are projected to amount to $1.3M for

the hadronic section and to $1.4M for the electromagnetic section. The readout is costed at $1.9M. The total FCS project cost amounts to $15M including $0.6M integration costs, 40% contingency and on average 40% overhead. Significant cost saving may be possible with the option of refurbishing the E864 calorimeter after validation of its performance as a part of the HCal system.

- The FTS project is at an earlier stage of development than the FCS projects. Two options are being considered, using either GEM or Silicon microstrip technology. The project total cost estimate given in Table 3-1 is based on the silicon option of about 130k readout channels and is based on experience with the Intermediate Silicon Tracker (IST) subsystem of the recently completed Heavy Flavor Tracker upgrade. It contains $1.4M for detector modules, $0.3M in mechanics, $0.7M for electronics, and additionally 30% contingency and 40% overhead. It is planned to be used for A+A, p+p and p+A physics with an envisioned timeline are similar to that of the FCS.

Upgrade projects	Year of completion	Total project cost (M$)	Funding Sources	Supplemental information
FCS	2020	15	potentially significant	50% from refurbishing E864 HCAL
FTS	2020	4.5	foreign	GEM or Silicon
Total (M$)		19.5	in-kind contributions	FY 12 Dollars

Table 3-1: Project cost estimates in FY12 funds for the baseline STAR upgrades essential for the p+p and p+A physics program outlined in this document.

The detector configuration presented in this document provides the baseline for STAR's forward instrumentation upgrade for the A+A, p+p and p+A physics program envisioned in early 2020s. We will continue to optimize the detector configuration in terms of physics capabilities and cost/schedule feasibilities. STAR welcomes more ideas and science-driven proposals to further strengthen the instrument, collaboration and physics capabilities.

4 Appendix

Charge to RHIC Collaborations: Future opportunities for p+p and p+A at RHIC

The current RHIC run plan anticipates high luminosity Au+Au and p+p runs of RHIC in FY2021 and FY2022 utilizing the enhanced capabilities of sPHENIX and STAR anticipated for these years. The current physics focus of these runs is on hard probes, especially jet observables and Upsilon states. Depending on the available operating funds and presently unknown details of the future run schedule, there may be the opportunity to perform high luminosity p+Au (or other p+A) runs during this time.

C-AD currently anticipates the following peak luminosities: 200 pb^{-1}/week for 500 GeV p+p and 300 nb^{-1}/week for 200 GeV p+Au. The p+p luminosity assumes a bunch intensity of 3×10^{11} up from the present value of 1.85×10^{11}, and shorter bunches. The p+Au luminosity assumes bunch intensities of 3.0×10^{11} for protons and 1.5×10^{9} for Au. Since these numbers represent substantial increases over historically achieved luminosities, it may be prudent to assume somewhat lower numbers for estimates of required beam times.

In view of the prospect that the capability to investigate p+p, p+A, and A+A collisions at RHIC may be lost after the possible transition of the RHIC facility to a electron-ion collider, it is timely to consider the future physics opportunities for a polarized p+p and p+A program at RHIC from our present state of knowledge.

The question of the relative priority of extended p+A runs in the final years of RHIC is likely to come up in the context of the upcoming Long Range Plan process. In order to provide a framework for this discussion I am hereby asking the Collaborations to submit Physics Assessments of the scientific reach of such a program in the light of the anticipated capabilities of the RHIC detectors at the time of the final RHIC campaign.

Specifically, I would request that the assessment considers the following issues:

- The scientific motivation for high statistics p+p and p+A data based on our current knowledge, especially in the light of a future EIC physics program and with special consideration of the use of polarized protons;
- What will likely be accomplished during Runs 14-16;
- The compelling physics observables and their expected physics reach;
- The required integrated luminosities;
- The possible need for collision systems other than p+Au (e.g. p+C, p+Cu, d+Au).
- Detector requirements for a successful p+p/p+A program and the associated cost and schedule.

In particular, the document should address which compelling physics questions the p+p and p+A program at RHIC could address in the early part of the next decade in the context of the experiment upgrade plans, the existing and anticipated data from RHIC, LHC, and COMPASS, and a future EIC. The document should address the question to what extent polarized p+p and p+A collisions are complementary to the physics program of an EIC and not just an alternate and possibly less discriminating way of studying the same physics.

In order to be most useful as basis for the discussions in the context of the Long Range Plan process, I request that you submit your assessment no later than April 30, 2014. The two RHIC collaborations may consider the value of collaborating on the physics part of this charge and developing a joint Physics Assessment, followed by separate sections describing the hardware requirements and expected physics reach of each detector.

Berndt Mueller

ALD for Nuclear and Particle Physics

October 8, 2013

5 Bibliography

[1] STAR BES White-Paper
[2] eSTAR Letter-of-Intent: https://drupal.star.bnl.gov/STAR/starnotes/public/sn0592
[3] The STAR Decadal Plan: http://www.bnl.gov/npp/docs/STAR_Decadal_Plan_Final[1].pdf
[4] H1 Collaboration, F. Aaron *et al.*. JHEP, **01**:109, 2010. arXiv:0911.0884.
[5] L. Adamczyk et al., Phys. Rev. **D 89** (2014) 012001; arXiv:1309.1800
[6] B. I. Abelev *et al.*, Phys. Rev. Lett. **101**, 222001 (2008), arXiv: 0801.2990
[7] L. Adamczyk et al., Phys. Rev. **D 86** (2012) 051101; arXiv:1205.6826
[8] K. Kanazawa, Y. Koike, A. Metz, D. Pitonyak, arXiv:1404.1033.
[9] S. Heppelmann, CIPANP-2012,
https://indico.triumf.ca/getFile.py/access?contribId=349&sessionId=44&resId=0&materialId=slides&confId=1383
[10] B. I. Abelev *et al.* (STAR Collaboration), Phys. Rev. Lett. **101**, 222001 (2008).
[11] M. M. Mondal, talk at DIS-2014:
http://indico.cern.ch/event/258017/session/6/contribution/216/material/slides/1.pptx
[12] Z.-B. Kang and J.-W. Qiu, Phys. Rev. Lett. **103** (2009) 172001, arXiv:0903.3629
[13] A.Metz and J. Zhou, Phys. Lett. B **700** (2011) 11, arXiv:1006.3097
M.G. Echevarria, A. Idilbi, Z.-B. Kang and I. Vitev, Phys. Rev. **D 89** (2014) 074013, arXiv:1401.5078
[14] S. Fazio, talk at DIS-2014, http://indico.cern.ch/event/258017/session/11/contribution/219/material/slides/0.pptx
[15] E.A. Hawker et al., Phys. Rev. Lett. **80**, 3715 (1998)
[16] J. Ralston and D.Soper, Nucl. Phys. **B 152**, 109 (1979).
[17] R. Jaffe and X. Ji, Nucl. Phys. **B 375**, 527 (1992).
[18] P. Mulders and R. Tangerman, Nucl. Phys. **B 461**, 197 (1996).
[19] J. C. Collins, Nucl. Phys. **B 396**, 161 (1993).
[20] J. C. Collins, S. F. Heppelmann, and G. A. Ladinsky, Nucl. Phys. **B 420**, 565 (1994).
[21]A. Airapetian *et al*. (HERMES Collaboration), Phys. Rev. Lett. **94**, 012002 (2005); **103**, 152002 (2009); Phys. Lett. **B 693**, 11 (2010).
[22] V. Y. Alexakhin *et al*. (COMPASS Collaboration), Phys. Rev. Lett. **94**, 202002 (2005); E. S. Ageev et al. (COMPASS Collaboration), Nucl. Phys. **B 765**, 31 (2007); M. G. Alekseev et al. (COMPASS Collaboration), Phys. Lett. **B 673**, 127 (2009); M. G. Alekseev et al. (COMPASS Collaboration), Phys. Lett. **B 692**, 240 (2010); C. Adolphetal. (COMPASS Collaboration), Phys. Lett. **B 717**, 376 (2012); N. Makke (COMPASS Collaboration), arXiv:1403.4218.
[23] A. Airapetian *et al.* (HERMES Collaboration), JHEP **0806**, 017 (2008).
[24] C. Adolph *et al*. (COMPASS Collaboration), Phys. Lett. **B 713**, 10 (2012).
[25] R. Seidl *et al.* (Belle Collaboration), Phys. Rev. Lett **96**, 232002 (2006); Phys. Rev. **D 86**, 039905(E) (2012).
[26] A. Vossen *et al.* (Belle Collaboration), Phys. Rev. Lett. **107**, 072004 (2011).
[27] M. Anselmino *et al.,* Phys. Rev. **D 75**, 054032 (2007); Nucl. Phys. B, Proc. Suppl. **191**, 98 (2009); Phys. Rev. **D 87**, 094019 (2013).
[28] A. Bacchetta, A. Courtoy, and M. Radici, Phys. Rev. Lett. **107**, 012001 (2011).
[29] R. Fatemi, AIP Conf. Proc. 1441, 233 (2012).
[30] A. Vossen, *Il Nuovo Cimento* **C 35**, 59 (2012).
[31] Z.-B. Kang, Phys. Rev. **D 83**, 036006 (2011).
[32] R. L. Jaffe and X. Ji, Phys. Rev. Lett. **67**, 552 (1991); Nucl. Phys. **B 375**, 527 (1992).
[33] J.P. Ralston arXiv:0810.0871.
[34] E. Aschenauer *et al.* (RHIC Spin Collaboration), arXiv:1304.0079.
[35] D. Sivers, Phys. Rev. **D 41**, 83 (1990); 43, 261 (1991).
[36] L. C. Bland *et al.* (A_NDY Collaboration), arXiv:1304.1454.
[37] L. Gamberg, Z.-B. Kang, A. Prokudin, Phys. Rev. Lett. **110**, 232301 (2013).
[38] A. V. Efremov and O. V. Teryaev, Sov. J. Nucl. Phys. **36**, 140 (1982); Phys. Lett. **150B**, 383 (1985); J.-W. Qiu and G. Sterman, Phys. Rev. Lett. **67**, 2264 (1991); Phys. Rev. **D 59**, 014004 (1998).
[39] D. Boer and P. J. Mulders, Phys. Rev. **D 57**, 5780 (1998).
[40] T. Rogers, Phys. Rev. **D 88**, 1, 014002 (2013).
[41] G. Bunce, N. Saito, J. Soffer, and W. Vogelsang, *Ann. Rev. Nucl. Part. Sci.* **50** (2000) 525.
[42] B. Abelev *et al.* (STAR Collaboration), *Phys. Rev. Lett.* **97**, 252001 (2006).
[43] B. Abelev *et al.* (STAR Collaboration), *Phys. Rev. Lett.* **100**, 232003 (2008).
[44] L. Adamczyk *et al.* (STAR Collaboration), *Phys. Rev.* **D86**, 032006 (2012).
[45] P. Djawotho (for the STAR Collaboration), arXiv:1106.5769 (2011).
[46] R. D. Ball et al., Nucl. Phys. **B 849**, 112 (2011) [Errata: ibid **854**, 926 (2012) and **855**, 927 (2012)];

R. D. Ball et al., Nucl. Phys. **B 855**, 608 (2012).
[47] D. de Florian, R. Sassot, M. Stratmann, and W. Vogelsang, arXiv:1404.4293.
[48] M. Stratmann, *Word Scientific - DIS 2006 Conference (Tsukuba, Japan)* **1**, 715 (2006).
[49] M. Walker, PhD Thesis, MIT (2011), B. Page, PhD Thesis IUCF (2013).
[50] D. de Florian *et al.*, *Nucl. Phys.* **B539**, 455 (1999).
[51] D. de Florian *et al., Phys. Rev. Lett.* **101**, 072001 (2008).
[52] M. Glück *et al*., *Phys. Rev.* **D63**, 094005 (2001).
[53] W. Vogelsang, private communication (2013).
[54] D. de Florian, *Phys. Rev.* **D79**, 114014 (2009).
[55] A. Accardi *et al.,* arXiv:1212.1701 (2012).
[56] M. Aggarwal *et al.*, Phys. Rev. Lett. **106**, 062002 (2011), arXiv: 1009.0326.
[57] E.C. Aschenauer et al., The RHIC Spin Program: Achievements and Future Opportunities, arXiv:1304.0079.
[58] E. Klempt and A. Zaitsev, Phys. Rept. **454 1** (2007).
[59] W. Ochs, J. Phys. **G 40** 043001 (2013).
[60] C. Amsler *et al.* (Crystal Barrel Collaboration), Phys. Lett. **B 291**, 347 (1992).
[61] C. Amsler et al. (Crystal Barrel Collaboration), Phys. Lett. **B 322**, 431 (1994).
[62] U. Wiedner, (PANDA Collaboration), Prog. Part. Nucl. Phys. **66**, 477 (2011).
[63] R.M. Baltrusaitis *et al.* (MARK-III Collaboration), Phys. Rev. **D 33**, 1222 (1986).
[64] M. Ablikim et al., (BES Collaboration), Phys. Lett. B 607, 243 (2005).
[65] M. Albrow, arXiv:1010.0625 (2010).
[66] T. Akesson *et al*., (AFS Collaboration), Nucl. Phys. **B 264**, 154 (1986).
[67] F. Antinori *et al*., (WA91 Collaboration), Phys. Lett. **B 353**, 589 (1995).
[68] D. Barberis *et al*., (WA102 Collaboration) Phys. Lett. **B 453**, 316 (1999).
[69] A. Austregesilo (COMPASS Collaboration), arXiv:1402.2170 (2014).
[70] M. Albrow, A. Swiech, M. Zurek (CDF Collaboration), arXiv:1310.3839 (2013).
[71] S.N. Ganguli and D.P. Roy, Phys. Rep. **67**, 201 (1980).
[72] T. Alesson *et al.* (AFS Collaboration), Nucl. Phys. **B 264**, 154 (1986).
[73] R. Schicker (ALICE collaboration), arXiv:1205.2588 (2012).
[74] T.A. Armstrong et al., Z. Phys. **C51**, 351 (1991).
[75] A. Kirk, Phys. Lett. **B 489**, 29 (2000).
[76] L. Adamczyk et al., Phys. Lett. **B 719,** 62 (2013).
[77] C.M. Richards *et al.* (UKQCD Collaboration), Phys. Rev. **D 82**, 034501 (2010).
[78] F. Close, A. Kirk, Phys. Lett. **B 397**, 333 (1997).
[79] A. Airapetian *et al.* (HERMES Collaboration), Phys. Lett., **B 577**:37–46, 2003, arXiv:hep-ex/0307023; Phys. Lett. **B 684**:114–118, 2010. arXiv:0906.2478.
[80] W. Brooks and H. Hakobyan, Nucl. Phys, **A 830**:361c–368c, 2009. arXiv:0907.4606.
[81] W. Brooks, Physics with nuclei at an Electron Ion Collider. 2010. arXiv:1008.0131.
[82] M. Vasilev *et al*. (E866 Collaboration), Phys. Rev. Lett., **83**:2304–2307, 1999. arXiv:hep-ex/9906010.
[83] H. Paukkunen, DIS-2014, http://indico.cern.ch/event/258017/session/1/contribution/222/material/slides/0.pdf
[84] I. Arsene *et al*. (BRAHMS Collaboration), Phys.Rev.Lett. **93**, 242303 (2004), nucl-ex/0403005.
[85] J. Adams *et al.* (STAR Collaboration), Phys.Rev.Lett. **97**, 152302 (2006), nucl-ex/0602011.
[86] A. Adare *et al.* (PHENIX Collaboration), Phys.Rev.Lett. **107**, 172301 (2011), 1105.5112.
[87] J. L. Albacete and C. Marquet, Phys.Rev.Lett. **105**, 162301 (2010), 1005.4065.
[88] Z.-B. Kang and F. Yuan, Phys.Rev. **D 84**, 034019 (2011), 1106.1375.
[89] Y.V. Kovchegov and M.D. Sievert, Phys. Rev. **D 86**, 034028 (2012), Erratum-ibid. **D 86**, 079906 (2012) arXiv:1201.5890.
[90] H. Weigert, Prog. Part. Nucl. Phys. **55** (2005) 461.
E. Iancu and R. Venugopalan, hep-ph/0303204.
F. Gelis, E. Iancu, J. Jalilian-Marian, and R. Venugopalan, Ann. Rev. Nucl. Part. Sci. **60** (2010) 463.
Y. V. Kovchegov and E. Levin, Quantum Chromodynamics at High Energy. Cambridge University Press, 2012.
J. Jalilian-Marian and Y. V. Kovchegov, Prog. Part. Nucl. Phys. **56** (2006) 104.
[91] D. Boer, A. Dumitru, and A. Hayashigaki, Phys. Rev. **D 74** (2006) 074018.
D. Boer and A. Dumitru, Phys. Lett. **B 556** (2003) 33.
D. Boer, A. Utermann, and E. Wessels, Phys. Lett. **B 671** (2009) 91.
[92] Z.-B. Kang and F. Yuan, Phys. Rev. **D 84** (2011) 034019.
[93] Y. V. Kovchegov and M. D. Sievert, Phys. Rev. **D 86** (2012) 034028.
[94] J.-W. Qiu, talk at the workshop on "Forward Physics at RHIC", RIKEN BNL Research Center, BNL, 2012.
[95] S. Klein and J. Nystrand, Phys. Rev. **C 60**, 014903 (1999), hep-ph/9902259.

S. Klein and J. Nystrand, Phys. Rev. Lett. **84**, 2330 (2000).
STAR Collaboration, Phys. Rev. **C 77** (2008) 34910.
[96] T. Toll and T. Ullrich, arXiv:1307.8059 [hep-ph] (2013).
[97] T. Toll and T. Ullrich, Phys. Rev. **C 87**, 024913 (2013).
[98] H. Kowalski, L. Motyka, G. Watt, Phys. Rev. **D 74**, 074016 (2006).
[99] H. Kowalski and D. Teaney, Phys. Rev. **D 68**, 114005 (2003).
[100] S. Munier, A. M. Stasto and A. H. Mueller, Nucl. Phys. **B603**, 427 (2001).
[101] S. Klein and J. Nystrand, hep-ph/0310223.
[102] K. J. Eskola, H. Paukkunen and C. A. Salgado, JHEP **0904**, 065 (2009).
[103] H.L. Lai et al., Eur. Phys. J. **C12**, 375 (2000).
A.D. Martin, R.G. Roberts, W.J. Stirling, and R.S. Thorne, Eur. Phys. J. **C4**, 463 (1998).
[104] J. Jalilian-Marian, Prog.Theor.Phys.Suppl. **187** (2011) 123, arXiv:1011.1601.
[105] J. Jalilian-Marian and A. Rezaeian, Phys. Rev. **D 86**, 034016 (2012); A. Rezaeian, Phys. Rev. **D 86**, 094016 (2012).
[106] T. Sjöstrand, S. Mrenna and P. Skands, Comput. Phys. Comm. **178**, 852 (2008).
[107] Di-jet production from PYTHIA-8.189 is scaled down due to its overestimation of inclusive π^0 yields than those reported by BRAHMS in Phys. Rev. Lett. **98**, 252001 (2007) and STAR in Phys. Rev. Lett. **97**, 152302 (2006).

[108] F. Arleo and S. Peigné, JHEP **03** (2013) 122.
[109] F. Arleo and S. Peigné, private communication.
[110] A. Adare *et al.* (PHENIX Collaboration), Phys. Rev. Lett. **107**, 142301 (2011).
[111] R. Aaij *et al.* (LHCb Collaboration), JHEP **1402** (2014) 072.
[112] B. Abelev *et al*. (ALICE collaboration), arXiv:1308.6726.
[113] E. Ferreiro, F. Fleuret, J.P. Lansberg and A. Rakotozafindrabe, Phys. Rev. **C 88** (2013) 047901.
[114] J. Albacete *et al.*, Int. J. Mod. Phys. **E 22** (2013) 1330007.